THE UNIVERSITY OF CHICAGO

INTEGRATING AN ATOM ARRAY WITH A NANOPHOTONIC CHIP: A SCALABLE QUANTUM SYSTEM

A DISSERTATION SUBMITTED TO
THE FACULTY OF THE PRITZKER SCHOOL OF MOLECULAR ENGINEERING
IN CANDIDACY FOR THE DEGREE OF
DOCTOR OF PHILOSOPHY

BY
NOAH GLACHMAN

CHICAGO, ILLINOIS
AUGUST 2025

ABSTRACT

Neutral atom arrays have been established as a leading platform in the quantum information science landscape, due in large part to their scalability and reconfigurable, any-to-any connectivity. Similarly, neutral atoms coupled to optical cavities have shown promise for quantum networking due to the inherent indistinguishability of individual atoms. In this work, we aim to combine these strengths by developing a platform that integrates a free-space atom array with a scalable photonic interface in the form of a nanophotonic chip.

This platform relies on three key innovations. First, we present a semi-open chip geometry featuring cantilevered nanophotonic crystal cavities, facilitating the operation of a free-space atom array in close proximity to the chip. Second, we develop a background-free imaging technique that suppresses scattering of the imaging beams from the nearby solid surface, enabling parallel, single-shot, site-resolved readout of the atom array near the nanophotonic devices. Third, we demonstrate free-space coupling to the on-chip cavities, paving a path toward spatial multiplexing utilizing the array of over 100 cavities fabricated on the chip.

Leveraging our background-free imaging method, we implement standard atom array protocols such as rearrangement. We further demonstrate the ability to load atoms into standing wave traps formed by partial retroreflection of our optical tweezers from the cavities. In these traps, the atoms are positioned hundreds of nanometers from the cavity surfaces, an essential step on the path toward realizing strong atom-cavity interactions. Together, these capabilities represent an important milestone towards scalable, integrated quantum systems of individually controlled atoms in engineered photonic environments.

TABLE OF CONTENTS

LIST OF FIGURES

LIST OF TABLES

ACKNOWLEDGMENTS

First and foremost, thank you Hannes for creating this opportunity. This project was only possible thanks to your vision and the care that you put into assembling such an incredible team of scientists. The lab truly felt like a home due to your dedication to cultivating a social and friendly atmosphere. I would also like to thank my thesis committee members, Professor Aashish Clerk, Professor Alex High, and Professor Zoe Yan, for their time, guidance, and insights.

Shankar, it has been my pleasure to work with you developing this experiment over the past six years. I will always admire the fearless leap that you took, joining the lab before the building finished construction and even before Hannes had finished his postdoc at Harvard. You laid the groundwork for this project and truly, none of this could have happened without your hard work and commitment.

Matteo, thank you for teaching me how to be a real programmer. You transformed the way we interact with our experiment during your one-year postdoc with us, raising morale and providing perspective whenever it was needed. You were, and have since continued to be, an incredible mentor and I am so thankful that we had this opportunity to work together.

Kevin, even though you weren't our postdoc, you were integral to getting our experiment off the ground. You taught me everything I know about optics and had the never-ending patience to answer my questions multiple times to ensure I truly understood. You shaped the culture of the lab and taught us all what it means to be a good scientist.

Our collaborators, Johannes and Alan, deserve recognition for their contributions in the early stages of development. Johannes provided important expertise and guidance in theoretically modeling the experimental system, while Alan worked closely with Shankar to develop the fabrication protocols for the nanophotonic cavities and the chip.

Yuzhou, thank you for your incredibly in-depth and well-prepared group meeting slides teaching us all about rare earth ion memories. Though Tommy Wiseau may be the only

filmmaker we have both seen, I hope to one day move on to watch some of the real cinema recommendations that you have provided over the years.

Dahlia, I have truly enjoyed disagreeing with you about food throughout our time together. Even though I don't really believe that you hate mint chocolate, it was honestly impressive how all-encompassing our taste differences are. I hope you find some local Austrian food that you like in Innsbruck. Nayana, thank you for bringing back fun group meetings after Shankar and I ran out of ideas. Your memes brought some much-needed life and flair back to our weekly meetings. I wish you both the best of luck carrying this experiment forward and can't wait to see what you do with it!

Justus, it was so much fun getting to know you and teaching you about our experiment. I was lucky to have the chance to overlap with you briefly, though I wish we had a bit more time. Timo, I hope you learned a thing or two from us during your stay. I'm looking forward to hearing about your future research at Delft. You both had so much to add to Red Lab during our final few months in Chicago.

I must also thank Luigi for the many hours of help, guidance, and entertaining stories in the machine shop, where I was often making custom parts for the experiment.

Ramon and Alex from Quantum Machines generously shared their time and expertise with us, meeting often and working together to get our optical tweezers and rearrangement infrastructure up and running.

I'd also like to acknowledge and thank Haley for building our 935 nm optical tweezer laser, Roberto for building many of our electronics control boxes, and Yuhao for designing our fast optical pulsing infrastructure.

Of course, the rest of the Bernien Lab, current and past members, contributed as well through countless discussions, lending us equipment and offering advice when things weren't working. It was this broader support network in the lab that really kept things afloat. I'm going to miss our daily lab lunches, conversations, and banter. Thank you to Shraddha,

Vikram, Ryan, Conor, Bob, Nikhil, Andrew, Jeff, Hongyi, Cody, Ka Hui, Anurag, Jeremy, Jordan, Samantha, and Wenjun.

Anchita and Jacob, you both ensured that our classes and many late-night problem sets were incredibly fun. Thank you for your friendship and support over the years. Nidhaan and James, thank you for introducing me to so many incredible people and ideas outside of physics. Beyond the university, I must thank Fanella, Mitch, Anna, Doug, Libby, and Ben for their support and for making Chicago feel like home. Adam, Sammy, David, and Noah, even though you weren't here in Chicago, your collective decades of advice, friendship, and support have been essential in shaping who I am today. Thank you for always having my back.

I wouldn't be here today without the incredible support of my parents, Jamie and Neil, as well as my brother, Matthew. Thank you for a life full of love, support, and encouragement. Last, but not least, thank you from the bottom of my heart to my partner, Noa. Your patience, support, and love have been the foundation upon which my life has been built over the past five and a half years. I couldn't have done this without you.

CHAPTER 1

INTRODUCTION

In a 1981 talk, Richard Feynman highlighted a fundamental limitation in using classical computers to simulate quantum systems, due to the exponential growth of the Hilbert space with system size [1]. He proposed an alternative approach of building a new type of computer which operates on fundamentally quantum mechanical information encoding and logic. While this idea is typically attributed to Feynman, it was independently introduced by Yuri Manin in 1980 [2, 3]. The concept of a universal quantum computer was further developed and formalized over the next decades, gaining widespread attention in the mid-1990s with the development of Shor's factoring algorithm and Grover's search algorithm [4, 5, 6]. Around the same time, in 1984, Bennett and Brassard developed the first quantum key distribution protocol, establishing yet another application of quantum information enabling provably secure communication [7].

With key application areas emerging, experimental efforts to design and demonstrate quantum information technologies intensified. In 2000, David DiVincenzo itemized a list requirements, known today as the DiVincenzo criteria, necessary to build a quantum computer and communicate quantum infomration [8]. These criteria include the following: (1) a scalable physical system of well-characterized qubits, (2) the ability to initialize qubit states, (3) coherence times far exceeding quantum gate operation timescales, (4) the ability to implement a "universal" set of quantum gates, (5) the ability to perform qubit-specific measurements, (6) interconversion between stationary and flying qubits, and (7) reliable transmission of flying qubits from one location to another.

Myriad physical architectures have been explored for quantum information processing in the intervening years, including but not limited to trapped ions, neutral atoms, superconducting circuits, photons, defect centers in solids, and quantum dots. The successes in the field spanning several architectures have driven increasing commercialization efforts in

industry. Today, the main challenges in the field relate to scalability, photonic interfaces, and quantum error correction. Neutral atom arrays in optical tweezers, once limited by low two-qubit gate fidelities, have recently emerged as a leading architecture. In large part, the growth of neutral atom arrays is due to their scalability, with recent demonstrations of over 6,000 individually trapped atoms in a single system [9]. High-fidelity two-qubit gates have also been demonstrated recently across several neutral atom groups and atomic species [10, 11, 12, 13]. Early demonstrations of quantum circuits performed on logical qubit encodings with neutral atom systems have further fueled interest in the platform [14].

A parallel research effort has been dedicated towards the goal of achieving strong, controllable, and coherent interactions between quantum emitters and photons, prime candidates for "flying" qubits [15, 16]. One particularly promising approach involves cavity quantum electrodynamics (QED), a field which studies quantum emitters coupled to resonant cavity modes [17, 18]. To enhance coupling strengths, there has been a push in the field to shift from free space Fabry-Perot cavities towards fiber-based and nanophotonic cavities, leveraging the small mode volumes, slow group velocities, and high local densities of photonic states achievable in these systems [19, 20, 21, 22].

While solid-state emitters such as defect centers and implanted rare-earth ions can be positioned close to the mode field maxima of nanophotonic structures, thereby achieving extremely large coupling strenghts, they suffer from inhomogeneous broadening and spectral variability due to their complex solid-state environments [23]. Neutral atoms, on the other hand, are intrinsically identical and spectrally stable, though historically, trapping atoms close enough to nanophotonic structures to achieve strong coupling to the evanescent field has been a challenge. Recently, experimental developments have overcome this barrier, enabling stable trapping of neutral atoms 100-250 nm away from the surface of nanofabricated dielectric structures, where strong atom-photon couplings can be achieved [21, 24, 25, 26, 27, 28, 29, 30].

1.1 Thesis Overview

This thesis focuses on improving the scalability of coupled atom-nanophotonic systems, paving a path past the single-device and few-atom regimes. Prior experiments have demonstrated the feasibility of coupling neutral atoms to nanophotonic structures, but have been limited in scale. Here, we present the development of an experimental platform that integrates large-scale optical tweezer arrays of neutral atoms with a nanophotonic chip hosting over one hundred nanophotonic devices. This system represents an important step toward distributed, modular quantum computing architectures combining the scalability and computational capabilities of atom arrays with the communication potential of quantum networking. It also enables the exploration of new regimes in quantum many-body physics, where atom-atom interactions can be designed and mediated via tailored photonic environments.

Thesis Outline

Chapter 2 provides background on key concepts in atomic physics, cavity QED, and recent advances in neutral atom and atom-nanophotonic systems to contextualize the experiments described.

Chapter 3 presents a detailed overview of the experimental apparatus, including optical, mechanical, and electronic subsystems.

Chapter 4 reviews the operation of our system and the experimental methods and techniques implemented in order to integrate the atom array with the nanophotonic chip. These results were presented previously in Ref. [31].

Chapter 5 explores future directions and applications in quantum networking and quantum simulation enabled by our hybrid platform.

Chapter 6 summarizes the main results and provides an outlook on the future impact of this work.

CHAPTER 2

BACKGROUND

In this chapter, we review several important experimental techniques in atomic physics and quantum optics that are central to the work presented in this thesis. We begin by discussing laser cooling and trapping methods, essential to neutral atom control. We then introduce the principles of cavity quantum electrodynamics (QED) and through this lens explain why nanophotonics are a natural choice for designing cavities. Finally, we examine recent developments in large-scale atom arrays and the integration of these systems with nanophotonics and optical cavities. The review is structured to follow both the historical development of these ideas and techniques as well as the underlying physical principles, providing a framework for understanding the technological and scientific context of this work.

2.1 Laser Cooling and Trapping

Laser cooling is a cornerstone of modern atomic physics. The fundamental concept exploits the fact that photons, despite being massless, carry momentum and can thus exert a force on atoms via radiation pressure. By appropriately tuning laser frequencies and exploiting light-matter interactions, one can reduce the motion of atoms to an extraordinary degree. At room temperature, atoms in a gas move at velocities on the order of hundreds of meters per second, comparable to the cruising speed of a commercial airplane. These high speeds present a major challenge for precision control in experiments. Laser cooling enables us to slow atoms down to speeds more akin to that of a sloth, corresponding to temperatures on the order of tens of microkelvin. The following sections review several experimental methods developed to reach these ultra-cold temperatures and to trap and hold atoms in place for extended experiments.

2.1.1 Doppler Cooling

In 1975, two pairs of physicists, Hänsch and Schawlow, and independently Wineland and Dehmelt, proposed the idea that laser light could be used to slow and cool atoms via radiation pressure [32, 33]. To understand the core concept, consider an atom moving with positive velocity along the x-axis and a counter-propagating laser beam traveling backwards along the -x direction. If the frequency of the laser beam is close to that of an atomic transition, the atom can absorb photons from the laser beam and receive a momentum kick $\Delta p = -\hbar k$ along the x-axis, opposing the atom's motion. The atom will then spontaneously emit the photon in a random direction. In this one-dimensional picture, either along the +x or -x direction. Since this emission process is isotropic, it will average out over many such absorption and emission events. However, the absorption process is directional and does not average out, leading to an overall net force slowing down the atom.

We can now add the Doppler effect to this picture. By red-detuning the laser from the atomic resonance, we induce an asymmetry whereby atoms moving towards the laser beam see the Doppler shifted light blue-shifted closer to resonance, increasing the likelihood of absorbing a photon. Meanwhile, atoms moving away from the laser beam see the laser as red-shifted further from resonance and are less likely to scatter a photon from the laser beam. In this way, we can preferentially target atoms moving towards the laser beam and slow them down without accelerating atoms moving in the opposite direction.

The first experimental demonstrations utilizing this technique to cool ions came in 1978, just a few years after the initial proposals [34, 35]. Another four years later, in 1982, Phillips and Metcalf employed a Zeeman slower to stop a beam of neutral atoms [36]. In this experiment, a collimated beam of slightly supersonic sodium atoms was sourced from a 500° oven and sent through a solenoid towards a counter-propagating "slowing" laser beam. The solenoid was designed to apply a spatially varying magnetic field along its length, inducing a Zeeman shift that compensates for the changing Doppler shift as the atoms slow down.

An alternative method involves chirping the frequency of the slowing beam laser to track the reducing Doppler shift as the atomic beam slows down instead of the spatially varying magnetic field.

The minimum temperature achievable via Doppler cooling is determined by balancing the cooling and heating rates from the scattering of the laser light, giving the Doppler limit as a function of the linewidth of the atomic transition γ:

$$T_D = \frac{\hbar\gamma}{2k_B} \tag{2.1}$$

2.1.2 Optical Molasses

In 1985, researchers at Bell Laboratories successfully extended this Doppler cooling method to three dimensions by applying red-detuned counter-propagating laser light along each Cartesian axis to cool neutral sodium atoms and create a cold gas around 240 μK, in agreement with the Doppler limit [37]. This configuration of red-detuned counter-propagating beams along three orthogonal axes enables atoms at the intersection of these beams can be effectively slowed regardless of their direction of motion, as the atoms will always preferentially absorb photons from the beam or beams that they are moving towards. This configuration is referred to as optical molasses since the force induced on the atoms is a viscous, velocity-dependent damping force. This damping force is highly effective at slowing down and cooling a cloud of atoms, however, these atoms are not trapped in space as there is no position-dependent force to hold them at any particular location. Thus, atoms in optical molasses have a timescale upon which they tend to escape the beam intersection region, which can be up to several seconds.

2.1.3 Magneto-optical Trap

A major advance came in 1987 with the demonstration of the magneto-optical trap (MOT) [38]. A MOT combines optical molasses with a quadrupolar magnetic field, typically generated by a pair of anti-Helmholz coils. The mangetic field creates a position-dependent Zeeman shift such that atoms displaced from the center of the trap are more likely to absorb photons from the beam that will push them back toward the center. This effect depends upon setting the correct opposite handedness ciruclar beam polarizations to match the orientation of the applied magnetic field gradient. Overall, the MOT combines the cooling, damping force of optical molasses with a restoring, trapping force allowing for stable trapping of cold, localized clouds of atoms.

2.1.4 Polarization Gradient Cooling

By 1988, it had become clear that experiments were successfully cooling atoms below the Doppler limit using techniques such as optical molasses [39]. The explanation lay in a new theoretical mechanism which today is known as polarization gradient cooling (PGC) or Sisyphus cooling. To begin understanding this new mechanism, consider a standing wave formed by two counter-propagating lasers with perpendicular linear polarizations. The polarization of this standing wave cycles from linear to circular every $\lambda/8$. Every $\lambda/4$, the circular polarization flips handedness and the linear polarization flips to its orthogonal state.

Now, consider an atom whose ground state has angular momentum $J = 1/2$ and whose excited state has angular momentum $J' = 3/2$ traversing this optical potential. This atom will experience spatially varying AC Stark shifts that depend upon both the M_J state and the position-dependent polarization of the standing wave. If the laser light is red-detuned of the atomic transition, then this shift is negative for both M_J states of the $J = 1/2$ ground state. This shift is larger in magnitude for the $M_J = -1/2$ state when the polarization is σ^- and larger in magnitude for the $M_J = 1/2$ state when the polarization is σ^+.

Now, we can begin to see why this effect is called Sisyphus cooling. Let's imagine our atom is at a location where the polarization is σ^+ and it absorbs a photon, thereby exciting it either from $M_J = -1/2$ to $M_{J'} = +1/2$ state or from $M_J = +1/2$ to $M_{J'} = +3/2$. The $M_{J'} = +3/2$ state can only decay back to down to its original $M_J = +1/2$ ground state, whereas the $M_{J'} = +1/2$ state can decay down to either ground state. If the $M_{J'} = +1/2$ state decays back to its original state, we are right back where we started, but if it decays down to the $M_J = +1/2$ state, then it cannot return to the $M_J = -1/2$ state by absorbing this σ^+ photon and decaying back down via spontaneous emission. This asymmetry leads to an effect known as optical pumping, whereby the $M_J = -1/2$ state can be optically pumped into the $M_J = +1/2$ state, but the reverse process cannot occur.

Next, consider what this means for the energy of the atom due to the polarization gradient. We are optically pumping the atom to a lower energy state, since the polarization is σ^+, the $M_J = 1/2$ state has a negative energy shift of larger magnitude. Thus, as the atom continues to traverse this polarization gradient induced energy potential in the $M_J = 1/2$ state, it will lose kinetic energy as it climbs the potential hill while the polarization rotates to σ^- over the next quarter wavelength (or an integer multiple of quarter wavelengths). Once the polarization has rotated to flip handedness, the reverse process can occur and the atom can be optically pumped back down in energy back to the $M_J = -1/2$ state, which is now the lower energy state. Just as Sisyphus was forced to continually roll a boulder up a hill only for it to fall back down again, the atom in this situation continuously climbs potential hills, giving up its kinetic energy to do so, and is then optically pumped back down to the bottom of the potential hill. The photon generated via the spontaneous emission process carries away the additional energy expended by the atom in each climb.

This explanation covers the case of perpendicular linear polarizations, though a similar, but fundamentally different, mechanism can occur when the counter-propagating lasers have σ^+ and σ^- polarizations. In both cases, the theoretical temperature limit is the so called

recoil limit caused by the momentum kick generated by the spontaneously emitted photon and thus depends upon the mass of the atom M and the wavelength of the cooling transition λ:

$$T_R = \frac{h^2}{k_B M \lambda^2} \tag{2.2}$$

This is typically much lower than the Doppler limit discussed previously and thus this mechanism fits into a category of techniques known as sub-Doppler cooling techniques. The Nobel Prize in 1997 was awarded to Steven Chu, Claude Cohen-Tannoudji, and William Phillips for their work in laser cooling including the explanation of the first sub-Doppler cooling mechanisms.

2.1.5 Dipole Traps

A thorough review of optical dipole traps can be found in Ref. [40]. Here we briefly summarize key concepts relevant to this thesis. When a neutral atom is placed into a laser field that is far detuned from one of its electronic transitions, the oscillating electric field of the laser light induces an oscillating electric dipole moment in the atom. The proportionality constant between the amplitude of the induced dipole moment and the amplitude of the electric field is called the atomic polarizability, a frequency-dependent and typically complex quantity.

The interaction potential between the laser field and the induced dipole of the atom is proportional to the intensity of the laser light and the real part of the atomic polarizability. The atom thus experiences a dipole force proportional to the gradient of the interaction potential and the real part of the atomic polarizability. When the laser is red-detuned from an atomic transition, the dipole force is attractive, pulling atoms towards regions of high intensity, whereas the force is repulsive when the laser is blue-detuned from an atomic transition. Thus, red-detuned beams can be used to directly trap atoms in focused optical

beams while so called bottle beam traps or potential barriers can be made using blue-detuned laser light. The atomic dipole will also absorb and spontaneously re-emit photons leading to a heating effect. This process occurs at a rate proportional to the intensity of the laser field and the imaginary part of the atomic polarizability. The dipole potential and scattering rate can be expressed as follows under the rotating wave approximation and assuming only a single atomic transition contributes:

$$U_{dip}(\mathbf{r}) = \frac{3\pi c^2}{2\omega_0^3}\frac{\Gamma}{\Delta}I(\mathbf{r}), \tag{2.3}$$

$$\Gamma_{sc}(\mathbf{r}) = \frac{3\pi c^2}{2\hbar\omega_0^3}(\frac{\Gamma}{\Delta})^2 I(\mathbf{r}). \tag{2.4}$$

Here, ω_0 is the atomic transition frequency, $\Delta = \omega - \omega_0$ is the detuning of the laser from the atomic transition, and Γ is the linewidth of the transition. Of course, the full effective dipole force must be calculated based upon the sum of the contributions from all nearby atomic transitions accounting for the polarization of the light and the Zeeman sub-level structure. However, these equations illustrate that the dipole potential scales as I/Δ while the scattering rate scales as I/Δ^2. Thus, optical dipole traps are often made using light with large detunings to ensure that the scattering rate, and thus the atomic heating rate, is minimal for a given trap depth. The first demonstration of an optically trapped small ensemble of neutral atoms was demonstrated in 1986 and has since become a standard technique in atomic physics [41].

Optical Tweezers

Optical tweezers are a specific realization of a dipole trap, formed by tightly focusing a laser beam near the diffraction-limited beam waist, typically around a micron or smaller for commonly used wavelengths. They are commonly employed to trap and manipulate small

particles and biological samples and their use in atomic physics gained prominence following the first demonstration of single atom trapping in 2001 [42]. In this pioneering experiment, a tightly focused red-detuned beam with a beam waist $< 1\mu$m was used to trap individual atoms from a background gas. Due to light-assisted collisions, these traps naturally enforce the collisional blockade mechanism whereby two atoms in the trap quickly collide and are lost, leaving behind either zero or one atom per trap [43, 44]. This mechanism makes optical tweezers an ideal tool for preparing and manipulating single atoms.

One year later, in 2002, the first two-dimensional array of neutral atoms trapped in optical tweezers was demonstrated using a microlens array to generate the tweezer array [45]. Since then, tweezer-based architectures have evolved considerably, with modern arrays typically generated using acousto-optic deflectors (AODs) or spatial light modulators (SLMs), which offer programmable control over trap depths and positions. These technologies enable rearrangement protocols to create defect-free arrangements despite the stochastic loading due to the collisional blockade. However, interest in microlens arrays and metasurfaces has not disappeared as they offer power efficient, compact, and passive methods of generating large-scale, static arrays which can be combined with moving traps for rearrangement [46, 47, 48, 49].

2.2 Cavity QED

The field of cavity quantum electrodynamics (QED) explores the interaction between light confined in a cavity and atoms or other quantum emitters. By tailoring the electromagnetic environment, cavities can profoundly alter the spontaneous emission and coherent dynamics of quantum systems. This control underlies a wide range of phenomena in quantum optics and plays a central role in fundamental physics research as well as emerging quantum technologies. The 2012 Nobel Prize in Physics was awarded to Serge Haroche and David Wineland for their work in controlling quantum systems. Serge Haroche's half of the prize

was granted for his pioneering cavity QED research.

2.2.1 Optical Cavities

To introduce optical cavities, we begin with the classic Fabry-Perot geometry consisting of a pair of highly reflective planar mirrors (M_1 and M_2, with reflectivities R_1 and R_2 respectively) separated by a distance L_c, enclosing a medium of refractive index n. A schematic illustration is provided in Fig. 2.1. When laser light enters the cavity through the partially transmitting mirror M_1, it will reflect back and forth between the two mirrors. A resonance condition is met when the cavity length L_c is equal to an integer multiple of half wavelengths: $L_c = m\lambda/2n$, where m is an integer. When this condition is met, the light within the cavity remains in phase, constructively interfering, causing an enhancement of the light field within the cavity and leading to transmission of the light through the cavity via the second mirror M_2. When this condition is not met, destructive interference suppresses the cavity transmission, resulting in reflection off of the input mirror M_1. The transmission spectrum through the cavity is thus a series of peaks corresponding to the resonant modes of the cavity described by the following equations [50]:

$$T = \frac{1}{1 + (4F^2/\pi^2)\sin^2(\phi/2)} \tag{2.5}$$

$$\phi = \frac{4\pi n L_c}{\lambda} \tag{2.6}$$

$$F = \frac{\pi(R_1 R_2)^{1/4}}{1 - \sqrt{R_1 R_2}} = \frac{FSR}{FWHM} \tag{2.7}$$

Here, ϕ is the round-trip phase shift and F is the cavity finesse. The cavity finesse is defined by the ratio of the free spectral range $FSR = c/(nL_c)$, or the distance between transmission peaks, to the width of the transmission peaks as defined by their full width

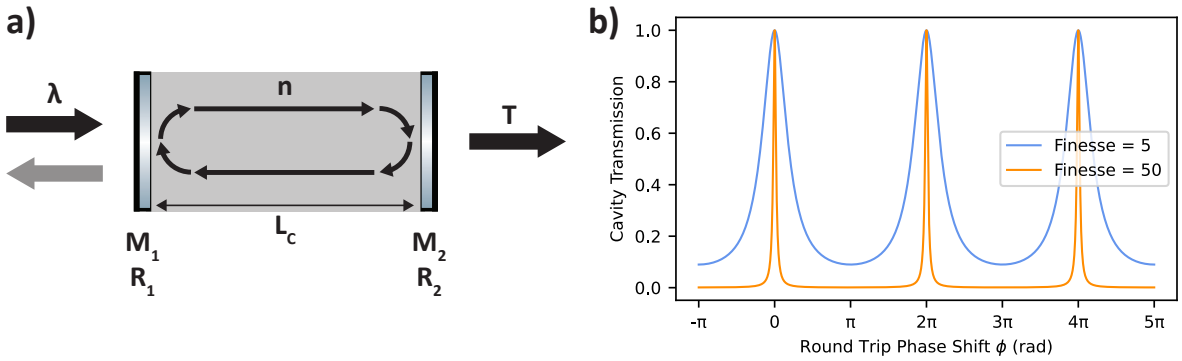

Figure 2.1: **Fabry-Perot cavity schematic.** **a**, A schematic of a Fabry-Perot cavity. **b**, The transmission spectra of two Fabry-Perot cavities with different finesses.

at half maximum, $\Delta\omega_{FWHM} = \frac{\pi c}{nFL_c} = \kappa$, where κ is the photon decay rate from the cavity. Thus, the finesse encapsulates how sharply defined the resonance peaks are. Another important figure of merit to consider for cavities is the quality factor $Q = \frac{\omega}{\Delta\omega}$, or the ratio of the resonance frequency to the width of the resonance, or equivalently the photon loss rate. The quality factor describes how underdamped a resonator is and can also be defined by the ratio of the energy stored in the resonator to the rate of energy loss.

2.2.2 Purcell Effect

When an atom is placed inside an optical cavity, the interaction between the atom and the cavity mode alters the atom's emission behavior depending upon the relative frequencies of the atomic transition and the cavity resonance. Often, it is desirable to ensure that the cavity's free spectral range is sufficiently large that the atom only interacts with a single resonant mode of the cavity. In this case, we can describe the atom-photon coupling strength with a parameter g and consider two limits, the strong coupling limit, $g \gg (\kappa, \gamma)$, where the atom photon coupling is the dominant effect compared to the two primary decay channels, and the weak coupling limit $g \ll (\kappa, \gamma)$, where decay dominates over the coherent atom-photon interaction. The two decay channels to consider are decay from the atom to free

space at rate γ and the rate of photon decay from the cavity κ. Let us begin with the weak coupling limit and briefly describe the Purcell effect, named after E. M. Purcell who discovered it in 1946 [51].

By using Fermi's golden rule, one can calculate the rate of spontaneous emission of the atom into free space, W_{free}, as well as the rate of spontaneous emission into the cavity mode, W_{cav} [50]. Purcell discovered that even in the weak coupling limit, the atomic decay into the cavity mode can be strongly enhanced or inhibited. This is often captured by the Purcell factor, here given assuming that the atom and cavity are co-resonant and that the atomic dipole is oriented properly to the cavity mode field such that the atomic emission enhancement is maximal. If these assumptions do not hold, the Purcell factor will be reduced, potentially enough to inhibit emission into the cavity mode instead of enhancing it, especially if the atom and cavity are far detuned from one another.

$$F_P = \frac{W_{cav}}{W_{free}} = \frac{3}{4\pi^2}\frac{\lambda^3}{n^3}\frac{Q}{V_0} \tag{2.8}$$

Here, n is the refractive index of the medium filling the cavity, λ is the vacuum wavelength of the light, Q is the quality factor of the cavity, and V_0 is the volume of the cavity mode. This result illustrates that high quality factors and small mode volumes lead to strong enhancement of the rate of emission into the cavity mode relative to free space. This can be expressed by examining the proportion of photons that get emitted into the cavity mode compared to the total number of emitted photons: $\frac{W_{cav}}{W_{free}+W_{cav}} = \frac{F_P}{1+F_P}$, which tends towards unity with increasing Purcell factor. This is a highly desirable condition from the perspective of quantum networking where it directly increases the collection efficiency of emitted photons.

2.2.3 Jaynes-Cummings Model

Now, consider the strong coupling regime, where the coherent atom-photon excitation exchange dynamics are faster than the decay timescales. In this situation, the atom can emit

a photon, preferentially into the cavity mode due to the Purcell effect, and subsequently re-absorb the photon multiple times before the excitation is lost from the atom-cavity system. The Jaynes-Cummings model, developed in 1963, provides a minimal quantum description of a two-level atom coupled to a single cavity mode under the rotating wave approximation [52]. Neglecting the vacuum-field energy for simplicity, the core Hamiltonian can be written as follows:

$$\hat{H}_{JC} = \hbar\omega_a\hat{\sigma}_{ee} + \hbar\omega_c\hat{a}^\dagger\hat{a} + \hbar g_0(\hat{\sigma}_{eg}\hat{a} + \hat{\sigma}_{ge}\hat{a}^\dagger). \tag{2.9}$$

Here, $\hat{\sigma}_{\mu\nu} = |\mu\rangle\langle\nu|$ is the atomic transition operator, $\hat{a}$ is the cavity mode annihilation operator, ω_a is the atomic transition frequency, and ω_c is the cavity mode resonance frequency. We must also define the atom-field coupling,

$$g_0 = d_{ge}\sqrt{\frac{\omega}{2\hbar\epsilon_0 V_0}}, \tag{2.10}$$

where d_{ge} is the transition dipole moment of the atomic transition and V_0 is the cavity mode volume. Here, we can see that the atom-cavity coupling strength increases as the mode volume decreases. This is one of the core motivations behind the utilization of nanophotonic cavities to strongly confine the field to a small mode volume.

The eigenstates of the uncoupled system can be constructed from the two atomic levels $|g\rangle$ and $|e\rangle$, defined to have energies 0 and ω_a respectively, along with the Fock states, or number states, of the cavity which can be labeled $|n\rangle$, where n is a whole number describing the quantized number of photons occupying the cavity mode. These states have energies $E_n = (n + 1/2)\hbar\omega_c$. Thus, if the atom and cavity are co-resonant, $\omega_a = \omega_c = \omega$, the uncoupled system has a single ground state, which can be labeled $|g, 0\rangle$, and a set of doubly degenerate excited states consisting of pairs of states $|g, n\rangle$ and $|e, n-1\rangle$.

Introducing the atom-cavity interaction lifts the degeneracy of the excited states, split-

ting them into pairs of eigenstates with wavefunctions $|\Psi_n^{\pm}\rangle = \frac{1}{\sqrt{2}}(|g,n\rangle \mp |e,n-1\rangle$ and corresponding eigenenergies $E_n^{\pm} = (n+1/2)\hbar\omega \pm \sqrt{n}\hbar g_0$. These are called dressed states and the whole set forms the Jaynes-Cummings ladder. Introducing a detuning $\Delta = \omega_a - \omega_c$ between the atomic transition and cavity frequencies controls the weighting of the dressed states, skewing the pairs of states away from equal parts atomic excitation and photonic excitation. See Fig. 2.2 for a diagram representing the Jaynes-Cummings ladder.

Though this model was developed theoretically in 1963, it took quite some time to experimentally demonstrate direct evidence of its predictions. The first of these was the collapse and revival phenomenon predicted for a coherent state input into this system, which was demonstrated experimentally in 1987 [53]. Several years later, in 1992, the optical vacuum Rabi splitting was observed for a small ensemble of atoms [54]. It was not until 2004 that the first demonstrations of the vacuum Rabi splitting for a single atom in a cavity was experimentally shown [55, 56].

One last important figure of merit used to describe these systems is the cooperativity, defined by the ratio of the coherent atom-photon interaction to the primary dissipative decay rates from the atom and the cavity:

$$C = \frac{g_0^2}{\kappa\gamma} \tag{2.11}$$

The strong coupling regime can occasionally be defined with respect to the cooperativity as $C > 1$. It is also important to note that $C \propto \lambda^3 Q/V_0$, again reinforcing the idea that small mode volumes and high quality factors are key metrics to optimize for these systems.

2.2.4 Nanophotonic Crystals

Nanophotonic crystals are periodic dielectric structures with regions of alternating dielectric constants that lead to photonic band structures closely analogous to the electronic band structures of solid-state physics [57]. Generally speaking, these structures exhibit

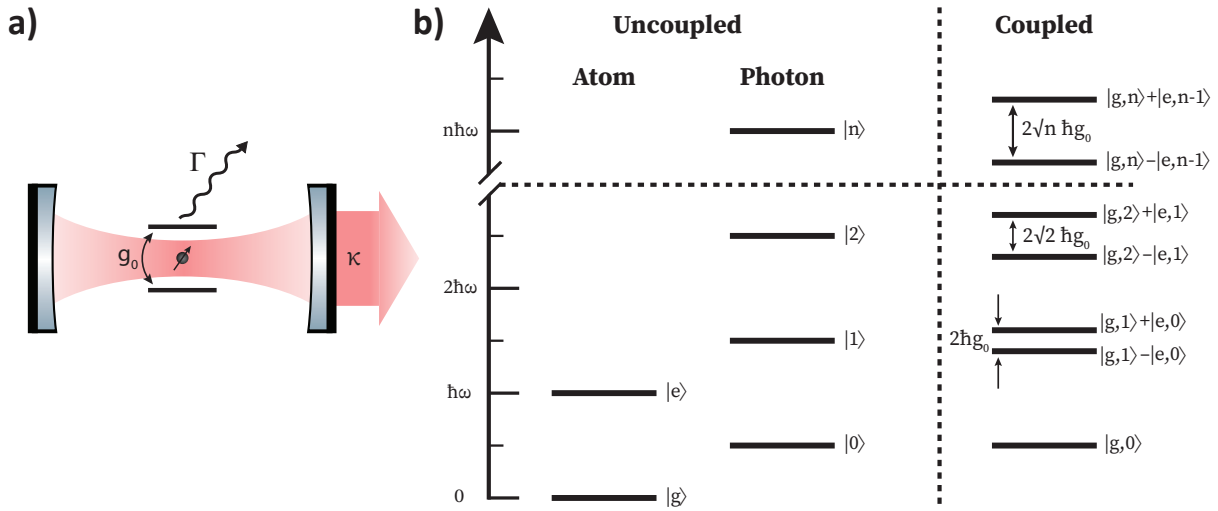

Figure 2.2: **Jaynes-Cummings model.** **a**, A schematic illustration of a prototypical atom-cavity system described by the Jaynes-Cummings model. **b**, Energy level structure of the Jaynes–Cummings model showing the vacuum Rabi splitting and dressed states. The coupled state wavefunctions neglect normalized prefactors for simplicity [50].

band gaps, or frequency ranges over which there are no allowed propagating modes due to interference effects arising from the structure's periodicity. Near a band edge at the wavevector k_0, the dispersion relation can often be closely approximated with the quadratic form $\omega(k) \approx \omega_{BE}(1 - \alpha(k - k_0)^2/k_0^2)$ where ω_{BE} is the frequency of the band edge and the fitting parameter α characterizes the local curvature of the band. We can also use Bloch's theorem to note that the allowed propagating modes near the band edge are of the form $E_k(x) = e^{ikx}u_k(x)$ where the $u_k(x)$ function captures the periodic nature of the photonic crystal's Bloch modes at the band edge and generally takes the form $u_k(x) = \cos(kx)$.

Photonic crystals can be used to make both waveguides or resonators. In the latter case, a photonic crystal cavity can be engineered by locally breaking the periodicity, for example by modifying the hole size, shape, or lattice spacing. If the central region supports a guided mode and the surrounding regions prohibit it, light can be confined via Bragg reflectino, forming a cavity with extremely small mode volume and potentially very high quality factor. This strategy underlies the nanophotonic crystal cavities integrated into the chip platform

described in this thesis. Alternatively, photonic crystal waveguides have exciting applications in the growing field of waveguide QED, a branch of physics closely related to cavity QED [58, 22, 59, 60, 61, 62, 63, 64, 65].

2.3 Neutral Atom Arrays

Building upon the techniques of laser cooling and optical tweezer trapping discussed earlier, neutral atom arrays have emerged as a compelling platform for quantum information science. In these systems, individually trapped atoms serve as qubits, arranged into arbitrary, programmable geometries using optical tweezers. Their rapid development has been driven by several compelling features including scalability to thousands of qubits [9, 48, 66, 67], long coherence times on the order of seconds for both hyperfine and clock state qubits [68, 69], reconfigurable any-to-any connectivity [68, 14], and high-fidelity gate operations [10, 11, 12, 13]. The degree of control achieved in these systems has even extended to arbitrary three-dimensional configurations [70].

A typical simple experimental sequence begins by loading a MOT of alkali or alkaline-earth atoms. A tightly focused tweezer array is then superimposed to stochastically trap single atoms via collisional blockade as PGC cooling is applied to further cool the atoms. These arrays are typically imaged via site-resolved fluorescence on an electron-multiplying charge coupled device (EMCCD) or scientific complementary metal–oxide–semiconductor (sCMOS) camera, where the internal qubit state is mapped onto the presence or absence of an atom at each site. A major milestone was achieved in 2016 when the first atom rearrangement protocols were demonstrated, enabling deterministic assembly of defect-free arrays, overcoming the limitations caused by the stochastic loading of the arrays [71, 72].

Two qubit entangling gates were first demonstrated in 2010, utilizing the Rydberg blockade mechanism, whereby one atom's excitation to a highly excited Rydberg state shifts the energy levels of its neighbor, preventing simultaneous excitation and enabling quantum

logic gates to be implemented [73, 74]. This technique has been refined and is now a standard technique in the field. Beyond quantum computing, the precise control over individual atoms in these systems has opened exciting applications in ultracold chemistry, where recent experiments have shown the ability to assemble individual atoms into molecules [75].

2.3.1 Atom Array - Nanophotonic Integration Efforts

Efforts to couple atoms to nanophotonic structures date back at least 25 years, prior to the first experimental observations of the vacuum Rabi splitting from a single atom in an optical cavity. In 1997, proposals began to couple atoms to whispering gallery modes (WGMs) of dielectric microsphere began to emerge [76, 77]. These were soon followed by additional proposals to trap atoms in two-color evanescent fields of optical nanofibers, to couple atoms to two-dimensional photonic crystals, and to couple atoms to WGMs of toroidal microcavities [78, 79, 80].

Since then, atoms have been successfully coupled to a wide variety of micro- and nanophotonic structures including, but not limited to, various WGM resonators [81, 82, 83], fiber-based Fabry-Perot cavities [84, 85, 20, 86], optical nanofibers [87, 88, 25, 28, 89], photonic crystal cavities [21, 24, 90, 91, 92], photonic crystal waveguides [93, 94], nanofiber Bragg grating cavities [95], and microring resonators [96, 97].

These developments have led to remarkable achievements. Experiments have demonstrated trapping of over 2,000 atoms along a nanofiber[25], precise loading of one and two atoms from free-space optical tweezers onto nanophotonic crystal cavities [21, 91], and observations of bandgap-mediated atom-atom interactions with a few atoms coupled to photonic crystal waveguides [22]. Commercial interest has followed, with Nanofiber Quantum Technologies in Japan developing a nanofiber Bragg grating cavity platform [98].

Despite this incredible progress, integrating a full scale atom array with nanophonic interfaces remains an open challenge. Systems that have demonstrated the coupling of many

atoms typically lack individual control over atomic placement via atom array techniques such as rearrangement or site-resolved addressing. Meanwhile, experiments which offer this degree of control have yet to scale beyond the few-atom or single-device regimes.

Another persistent challenge is atomic state readout. Most experiments to date have relied on transmission or reflection measurements probing the nanophotonic to infer global system properties. However, parallel, site-resolved readout via fluorescence imaging has been essential to the success of neutral atom arrays as quantum information processors. Several experiments have attempted to address this gap and incorporate imaging of atoms near dielectric surfaces, yet the techniques employed have either not been generally applicable to arbitrary nanophotonic geometries or have scalability limitations [89, 96, 91].

These challenges of scalability, individual atomic control, and parallel, site-resolved readout lie at the forefront of experimental research on atom-nanophotonic systems. The next two chapters focus on our experimental apparatus and initial results, representing key steps towards addressing these challenges and developing scalable atom-nanophotonic systems.

CHAPTER 3

EXPERIMENTAL APPARATUS

Over the past two decades, remarkable progress has been made towards assembling and manipulating quantum systems atom-by-atom, exemplifying a bottom up approach to scalability whilst maintaining fine control over each individual atom. Here, we apply those principles to integrate a neutral atom array with a millimeter-scale nanophotonic chip hosting over one hundred photonic crystal cavities. This merging of technologies aims to enable precise placement of defect-free configurations of atoms into tailored photonic environments, opening new directions in quantum networking, quantum many-body physics, chiral quantum optics, and collective phenomena such as super- and sub-radiance. Combining the precise control and flexibility of optical tweezer arrays with the scalability and functionality of on-chip photonics will lay the foundation for novel, scalable quantum architectures.

This chapter presents a detailed overview of the experimental apparatus developed to realize this goal, focusing specifically on the scalability of atom-nanophotonic systems. We introduce several key experimental features:

1. a semi-open chip geometry which enables a free-space atom array to interface directly with a nanophotonic chip,

2. free-space coupling to an array of on-chip photonic crystal cavities,

3. a background-free fluorescence imaging technique that enables parallel, site-resolved, single-shot readout of atom arrays positioned near dielectric surfaces.

We begin the chapter by describing the laser systems used for cooling, trapping, and manipulating atoms. We then review the compact vacuum chamber design, surrounding optics layout, and custom oven used to bake the system. Next, we introduce the nanophotonic chip, free-space coupling, and our approach to stabilizing the cavity resonance frequencies.

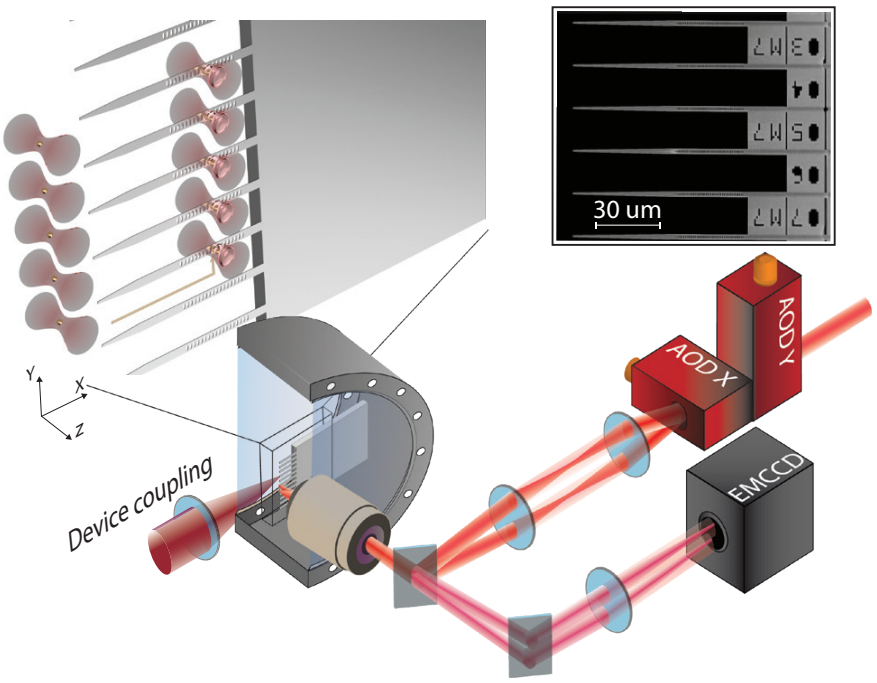

Figure 3.1: **A schematic illustration of our atom array - nanophotonic chip platform.** This schematic shows our optical tweezer array manipulating single cesium atoms near a chip hosting an array of nanophotonic devices. The chip is shown inside a stainless steel ultrahigh vacuum chamber. Also depicted are the acousto-optic deflectors (AODs) to control the tweezer array and the electron multiplying charge-coupled device (EMCCD) used to image the array. The inset shows a scanning electron microscope (SEM) image of the nanophotonic cavity array at the edge of our chip. This figure was adapted from our previous publication: Ref [31].

Lastly, we provide a brief overview of our experimental control infrastructure. Fig. 3.1 provides a schematic overview of some key components of the setup.

3.1 Laser Frequency Stabilization and Distribution System

The laser systems form a cornerstone of the experimental apparatus, enabling cooling, trapping, manipulation, and measurement of atoms in the vacuum chamber. One of my first main projects upon joining the lab was to acquire a suite of lasers and to develop our core laser frequency stabilization and optical power distribution system. The overall laser system consists of multiple interrelated branches, which can be broadly categorized

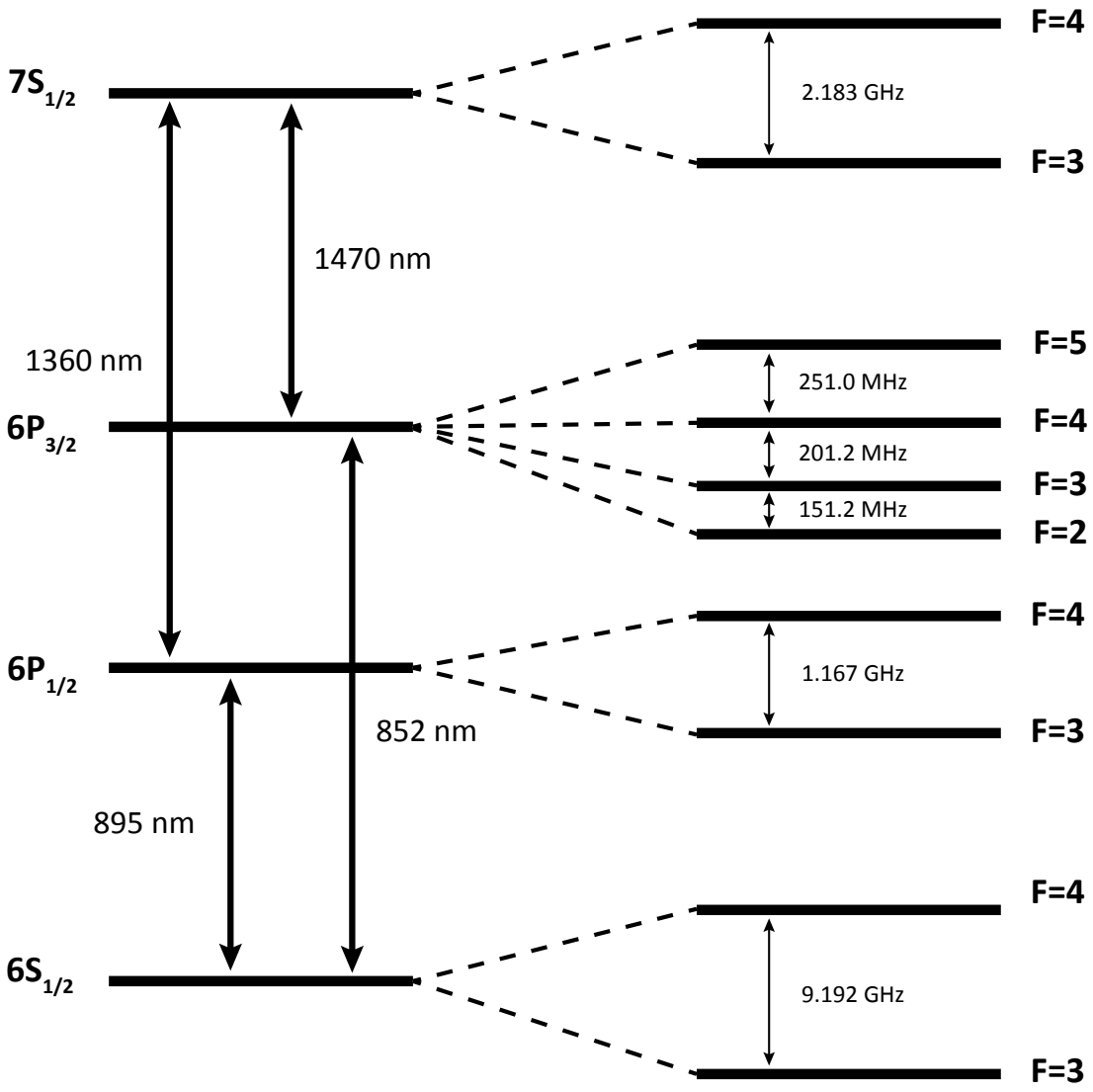

Figure 3.2: **Energy level diagram for caesium.** A schematic depiction of the fine structure and transition wavelengths as well as hyperfine structure and splittings of the relevant caesium energy levels for this work [99, 100, 101].

into the MOT laser system for trapping, cooling, and imaging, the 1470 nm laser system used in our background-free imaging technique and telecom photon generation protocol, the optical tweezer laser system, and our D1 line laser system at 895 nm. Additional laser systems used to characterize and frequency stabilize the resonances of the nanophotonic cavities will be discussed separately in Chapter 3.3, where we introduce the nanophotonic chip. For reference, the relevant caesium atomic level structure is depicted in Fig. 3.2 to aid in contextualizing these laser systems.

3.1.1 D2 Line Laser System

A typical caesium magneto-optical trap (MOT) is formed by three orthogonal pairs of counter-propagating laser beams intersecting at the zero-crossing point of a quadrupolar magnetic field gradient. This magnetic field gradient is generated by a pair of coils in an anti-Helmholtz configuration. Each MOT beam is composed of two optical frequencies that address specific hyperfine transitions of the caesium D2 line at 852 nm.

The first frequency, known as the cycler or cooling laser, drives the $6S_{1/2}$ F=4 to $6P_{3/2}$ F$'$=5 cycling transition. This beam is slightly red-detuned from the atomic transition in order to exploit the Doppler effect to slow down and cool the atoms as described in Chapter 2.1.

The second frequency, referred to as the repump laser, addresses the $6S_{1/2}$ F=3 to $6P_{3/2}$ F$'$=4 transition. Atoms participating in the cooling process, experiencing repeated excitation on the cycling transition, can occasionally decay to the $6S_{1/2}$ F=3 ground state, which is dark to the cooling beam. The purpose of the repump laser is to re-excite these atoms, optically pumping them back into the cooling manifold for sustained cooling and trapping.

The D2 line transitions are highly versatile and are also used for polarization gradient cooling (PGC) and fluorescence imaging. Therefore, this laser must have a highly tunable and dynamically adjustable frequency since the optimal laser frequency differs for each of

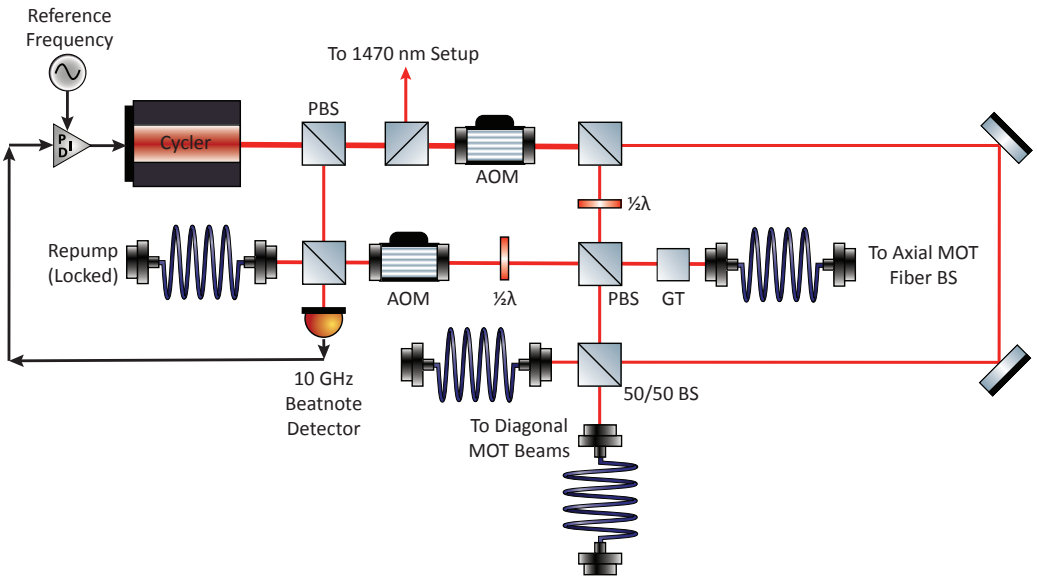

Figure 3.3: **A simplified schematic illustration of the 852 nm MOT cycler and repump optics layout.** This figure was created using Alexander Franzen's Component Library [102]. For clarity, the schematic omits several components, such as polarization optics, shutters, and detailed beam routing, which are important parts of the actual experimental setup.

these applications. This tunability is achieved by offset phase locking the cycler laser to the repump laser. The repump laser is provided to our experiment by the dual-species atom array experiment [103, 104, 105], where it is locked to the $6S_{1/2}$ F=3 to $6P_{3/2}$ F′=3x4 crossover resonance via saturation absorption spectroscopy. The offset phase lock enables dynamic and precise adjustment of the cycler laser frequency with respect to the repump over a broad frequency range by adjusting the frequency of a reference tone provided to the lock box.

Our MOT laser system consists of a high-power distributed Bragg reflector (DBR) laser head, laser controller, and offset phase lock servo, all sourced from Vescent Technologies, Inc. The repump laser provided by the dual-species array lab is also a Vescent DBR laser that is amplified with a tapered amplifier (TA) before being fiber-coupled and relayed to our experiment.

A schematic of the MOT optics layout depicting the cycler and repump beam paths is

shown in Fig. 3.3. Approximately 1 mW of each laser is tapped off and sent to a 10 GHz beatnote detector stabilize the cycler laser frequency via the offset phase lock. An additional ∼2 mW is tapped off from the cycler beam to use as a reference for the 1470 nm laser frequency stabilization, described in Chapter 3.1.3. Next, around 20 mW of the cycler is tapped off to be used in generating fast pulses for our telecom photon generation scheme. The remainder of the cycler beam power is then split into several paths where it is mixed with the repump laser and then fiber coupled for delivery to the vacuum chamber.

The MOT optics on the vacuum chamber side, which further shape and direct these beams are described in Chapter 3.2.3. The acousto-optic modulators (AOMs) on the beam paths that lead to the experiment are used for fast switching and optical power control of the beam, whereas the AOMs on the locking beam paths are primarily used to provide frequency shifts.

3.1.2 D1 Line Laser System

The caesium D1 line, corresponding to the 895 nm transition between the $6S_{1/2}$ and $6P_{1/2}$ states, also plays an important role in our experimental protocols. This transition is addressed using a Toptica DL pro external cavity diode laser (ECDL). A simplified schematic of the optical layout for this laser system is shown in Fig. 3.4.

The optics layout is divided into three main branches. The first branch, tapped off by the first beamsplitter in the schematic before the EOM, routes the majority of the optical power towards the experiment via an optical fiber. For some experiments, this beam passes through additional fiber-based infrastructure to enable fast pulse generation as described in Chapter 5.1.4. The AOM on this path is used for fast optical switching of the beam and provides control over the optical power routed to the experiment.

The remaining two branches are dedicated to frequency stabilization of the 895 nm laser and 1360 nm laser respectively. The 895 nm laser is locked via a compact saturation ab-

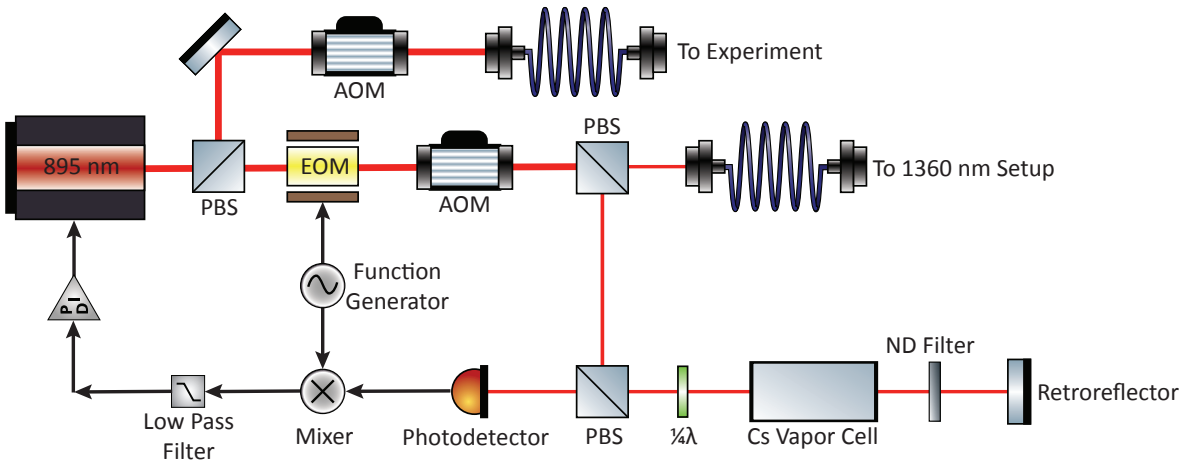

Figure 3.4: **A simplified schematic of the 895 nm D1 line optics layout.** This diagram illustrates the three main branches routing light to the experiment, to a saturation absorption lock for the 895 nm laser, and to the 1360 nm locking setup. This figure was created using Alexander Franzen's Component Library [102].

sorption spectroscopy setup, providing a stable atomic reference. Both branches share a 10 MHz free space electro-optic modulator (EOM) from Qubig, which modulates the 895 nm beam to generate sidebands necessary for the generation of both independent error signals. The AOM on these paths provides a frequency shift identical to the one applied on the experiment branch, ensuring that the light routed to the experiment remains on resonance with the atomic transition after frequency stabilization.

3.1.3 Laser Systems for Excited State Transitions

In addition to the D line transitions, our experiment requires addressing two excited-state transitions from the $6P_{1/2}$ and $6P_{3/2}$ levels to the $7S_{1/2}$ state at 1360 nm and 1470 nm respectively. Frequency stabilizing lasers to these transitions is slightly more involved since the 6P states are not significantly populated in a thermal atomic vapor. While an optical cavity can provide a viable reference, directly referencing the atomic transition can be desirable with regard to cost-effectiveness and stability. We implement a double resonance optical pumping (DROP) spectroscopy scheme inspired by the electromagnetically induced

transparency (EIT) locking scheme presented in Ref. [106]. This enables us to directly reference these two lasers to their respective atomic transitions, leveraging our already locked D line lasers. A schematic depicting the optical layout for these systems is shown in Fig. 3.5.

In this setup, our frequency stabilized ground-state "probe" laser counter-propagates with an excited-state "coupling" laser through a vapor cell. The probe beam is modulated using an EOM. The probe beam transmission through the vapor cell is is split off with an appropriate dichroic and monitored on a photodiode. As the coupling beam frequency is scanned, a change in the probe transmission signal indicates the two-photon resonance condition. Demodulating the probe transmission signal from the photodiode at the EOM frequency yields an error signal which is used to stabilize the coupling laser.

If the probe laser is detuned from the atomic resonance, as can be the case with our 852 nm cycler, then additional care must be taken to accurately determine the frequency of the excited state laser. Even with wedged windows on the glass cell, a small, slightly misaligned backreflection can lead to a second, weaker peak in the spectrum due to flipped sign of the Doppler shift of the backreflected beam [107]. Additionally, the main peak feature shifts away from the true double-resonance by $\Delta_c = \Delta_p(\lambda_p/\lambda_c)$ due to the wavelength dependence of the magnitude of the Doppler shift [107].

The observed signal in this configuration has contributions from both EIT and DROP. EIT is a coherent phenomenon in which the atomic vapor becomes transparent to the probe by trapping the atomic population in a dark eigenstate of the driven system. DROP, on the other hand, induces transparency as population is optically pumped into a second, uncoupled ground state [108].

In the 852/1470 nm system, a transparency feature consistent with this explanation is observed, as expected. Interestingly, however, for the 895/1360 nm system, the double-resonance condition results in increased absorption of the probe beam, rather than increased

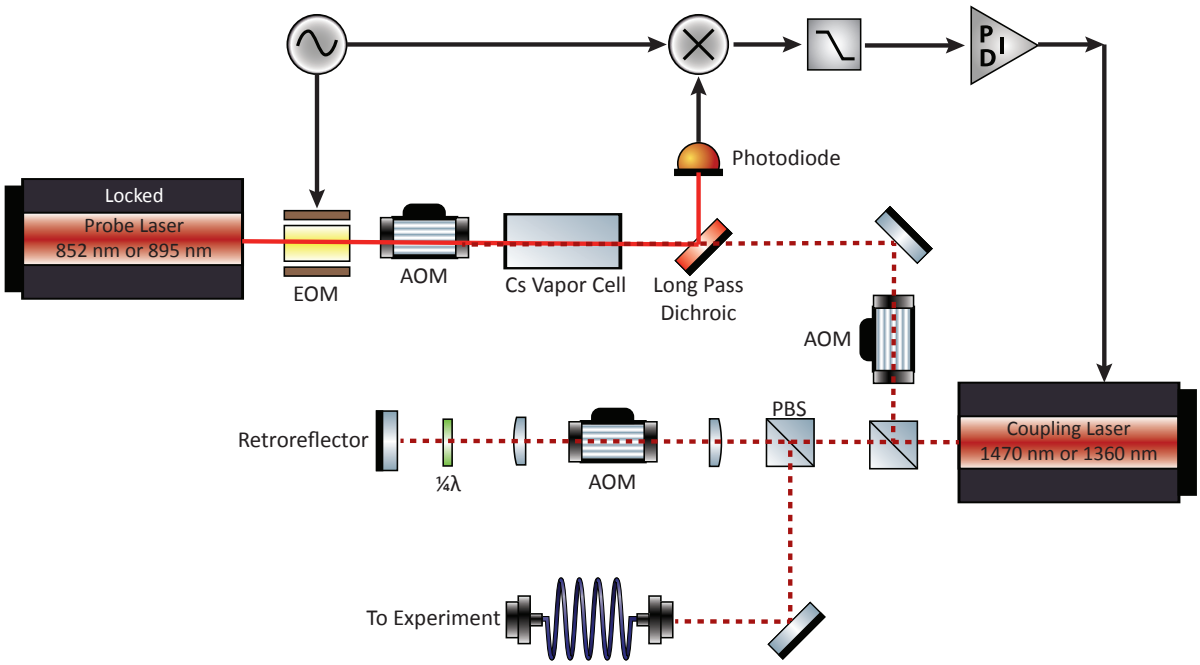

Figure 3.5: **A simplified schematic reviewing the excited state frequency stabilization system.** This layout is used to frequency stabilize the 1360 nm and 1470 nm lasers, referenced to the D1 and D2 line lasers respectively. The secondary path from the coupling laser traverses a double-passed AOM in a cat's eye retroreflection configuration to increase its frequency tuning range and improve the robustness of the beam path to misalignment from the fiber core as the AOM drive frequency is tuned. The other AOM on the coupling beam path to the vapor cell is optional and can be used to further shift or increase the frequency range accessible to the laser. This figure was created using Alexander Franzen's Component Library [102]

transmission. While this does not interfere with the generation of the error signal for our purpose of frequency stabilization, it does represent a deviation from the expected increased transmission behavior observed in similar configurations, such as the 852/575 nm two-photon transition to the $11S_{1/2}$ state [109], the 895/761 nm two-photon transition to the $8S_{1/2}$ state [110], and the 852/795 nm two-photon transition to the $8S_{1/2}$ state [111].

Another study of the 852/1470 nm two-photon transition to the $7S_{1/2}$ state observed both increases and decreases in the probe transmission depending upon which D2 line hyperfine resonance the 852 nm laser was locked to [101]. This was attributed to electromagnetically induced absorption (EIA) for level configurations where the transition pathway is not cycling. Further work may yield deeper insight into the underlying mechanism at play. Example spectra taken for several level configurations are shown in Fig. 3.6.

3.1.4 Optical Tweezer Laser System

Our optical tweezers are generated by a custom-built 935 nm laser constructed by Haley Nguyen during her time as an undergraduate researcher in the lab. This wavelength was chosen because it is the magic wavelength for the D2 line of caesium, meaning that the $6S_{1/2}$ state and $6P_{3/2}$ states experience the same AC Stark shifts from this wavelength. Thus, this atomic transition frequency is independent of the intensity of the optical tweezers.

This laser is sent through an external optical isolator before it is amplified by a Moglabs TA with $\sim$2 W of output optical power. The TA output is then focused through an AOM which is used for intensity stabilization and control of the laser power as well as fast optical switching, for example in drop recapture temperature measurements. We couple this beam into an air-gapped high power optical fiber to clean up the suboptimal spatial mode of the TA output. This fiber also serves to route the beam to the experiment side of the optical table. A beam sampler at the fiber output taps off a small fraction of the beam for our tweezer intensity stabilization.

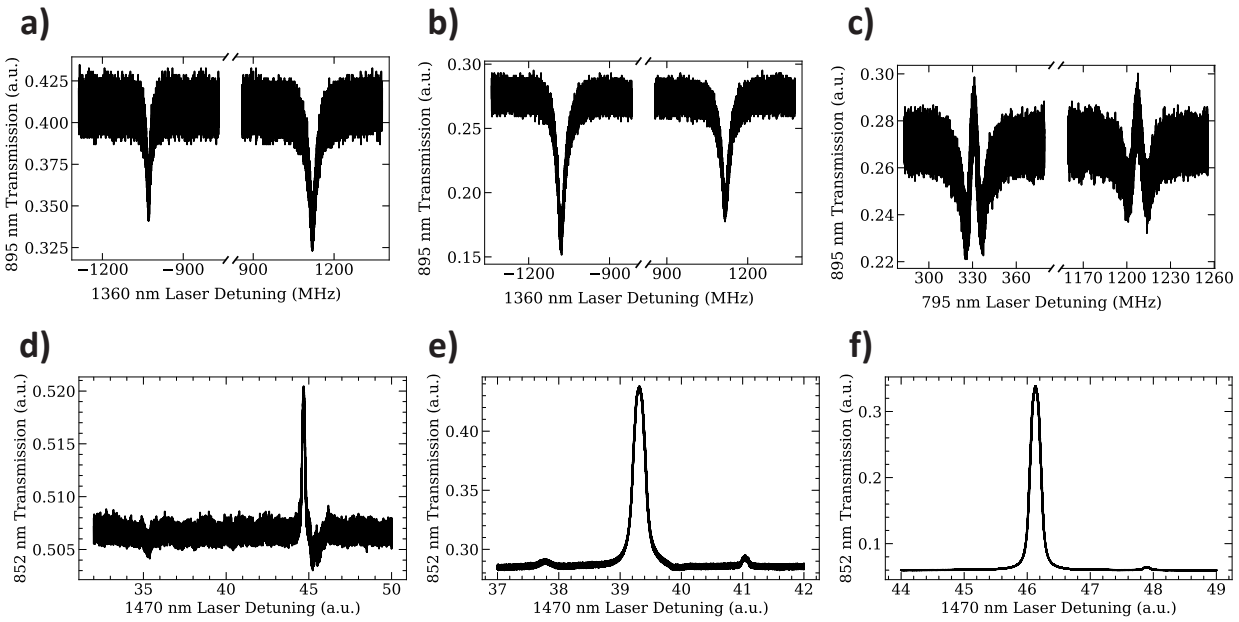

Figure 3.6: **Example DROP spectroscopy spectra for various two-photon transitions in the counter-propagating configuration.** **a**, Here, our 895 nm laser is locked to the $6S_1/2$ F=3 to $6P_1/2$ F'=3 transition and the 1360 nm laser frequency is scanned across the $7S_1/2$ hyperfine splitting to reveal two drops in transmission. **b**, Same as **a**, however, in this case the 895 nm laser is locked to the $6S_1/2$ F=3 to $6P_1/2$ F'=4 transition. **c**, Here, we keep the 895 nm laser locked to the $6S_1/2$ F=3 to $6P_1/2$ F'=4 transition and replace the 1360 nm coupling beam with a 761 nm couping beam to excite up to the $8S_1/2$ level, noting a peak in the transmission spectrum accompanied by two drops in transmission, a typical lineshape for these spectra [110]. **d**, Here, we return to the $7S_1/2$ doubly excited state, and replace the probe beam with the 852 nm D2 line laser, locked to the $6S_1/2$ F=3 to $6P_3/2$ F'=3 transition. The x-axis is not calibrated to frequency here, but the scan is a narrow scan about the F=4 $\rightarrow$ F'=5 $\rightarrow$ F"=4 transition, which is quite weak in this case as the ground state laser is not close to resonance. **e**, Same as **d**, but the 852 nm laser is locked to the $6S_1/2$ F=3 to $6P_3/2$ F'=4 transition. **f**, Same as **d**, but the 852 nm laser is locked to the $6S_1/2$ F=3 to $6P_3/2$ F'=5 transition.

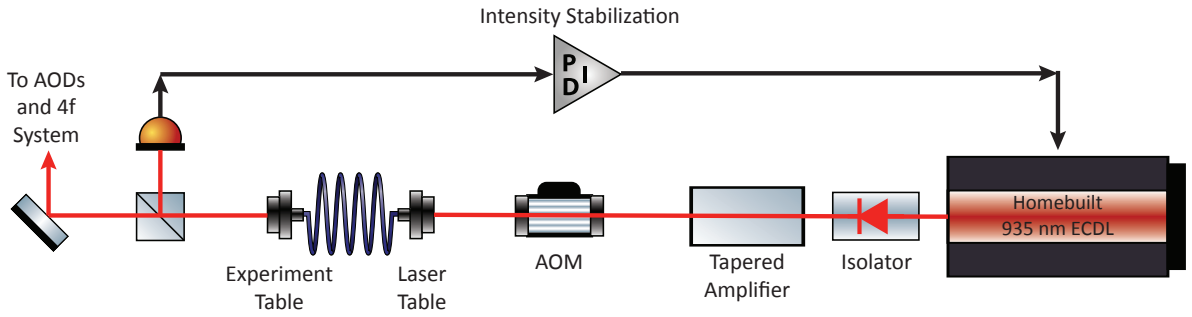

Figure 3.7: **A simplified schematic layout of the optical tweezer laser system.** The remainder of the optical path, to the AODs and 4f system, is shown in Fig. 3.12. This figure was made using Alexander Franzen's Component Library [102]

The remainder of the beam continues on to a pair of crossed acousto-optic deflectors (AODs) from AA-Optoelectronics, which split the beam into an array of optical tweezers. The AODs are driven by the amplified outputs from a first-generation Quantum Machines OPX, discussed further in Chapter 3.4.

The beam then traverses a 4f optical system which relays the tweezer beams to the vacuum chamber through a custom 0.6 NA objective from Special Optics, which is anti-reflection coated for each of our laser wavelengths. A schematic of the pre-optical fiber layout is presented in Fig. 3.7. A simplified schematic of the optical tweezer layout up to the tweezer intensity feedback loop is shown in Fig. 3.7, while the remainder of the beam path is depicted in Fig. 3.12 along with the rest of the chamber side beam delivery optics.

Optimal Filling Fraction

The filling fraction, or truncation ratio, of a Gaussian beam relative to the back aperture of an objective lens significantly influences both the optical power transmission and the effective numerical aperture (NA) of the lens, thereby altering the focal spot size and axial focal depth. These effects have been extensively studied in the context of microscopy [112, 113] and play a particularly important role for optical tweezers as well [114]. The NA

of an objective lens is typically specified under the assumption of uniform filling of the back aperture with a "top-hat" beam profile or a plane wave input, however, Gaussian beams are much more common in experiments. Experimentally, uniform filling can be well approximated by overfilling the back aperture with a Gaussian input beam whose diameter has been expanded to exceed the diameter of the aperture. This approach trades off optical power efficiency due to clipping of the beam at the input aperture in order to maximize the effective NA and retain a diffraction-limited focal spot.

If we define the filling fraction as the ratio of the $1/e^2$ diameter of the Gaussian beam to the diameter of the back aperture, we can examine the transmission as a function of the filling fraction as in Fig. 3.8. Here, we can see that even for a filling fraction of 1, approximately 14% of the optical power is lost to clipping. Underfilling the back aperture increases the power transmission, yet reduces the effective NA of the lens leading to an increase in the focal spot size. This effect is often encapsulated into a spot size factor, or K-factor, which can be calculated numerically. Several empirical polynomial fits to the K-factor are available in the literature, and are plotted in Fig. 3.8 [115, 116, 117]. At a filling fraction of 1, the $1/e^2$ beam waist is increased by $\sim$11% relative to the theoretical value obtained with uniform filling.

Accounting for these effects, we can calculate the resulting tweezer trap depth as a function of the filling fraction. The results, plotted in Fig. 3.8, suggest an optimal range of 0.92 ± 0.05. Across this range, all estimates agree that the trap depth remains within 1% of the theoretical optimum. These findings are consistent with the literature, for example, Ref. [114] finds an optimal filling fraction of 0.9 ± 0.05 for trapping microspheres with some dependence upon the diameter of the microsphere. Based upon these findings, we designed our optical tweezer microscope to slightly underfill the back aperture of our objective lens.

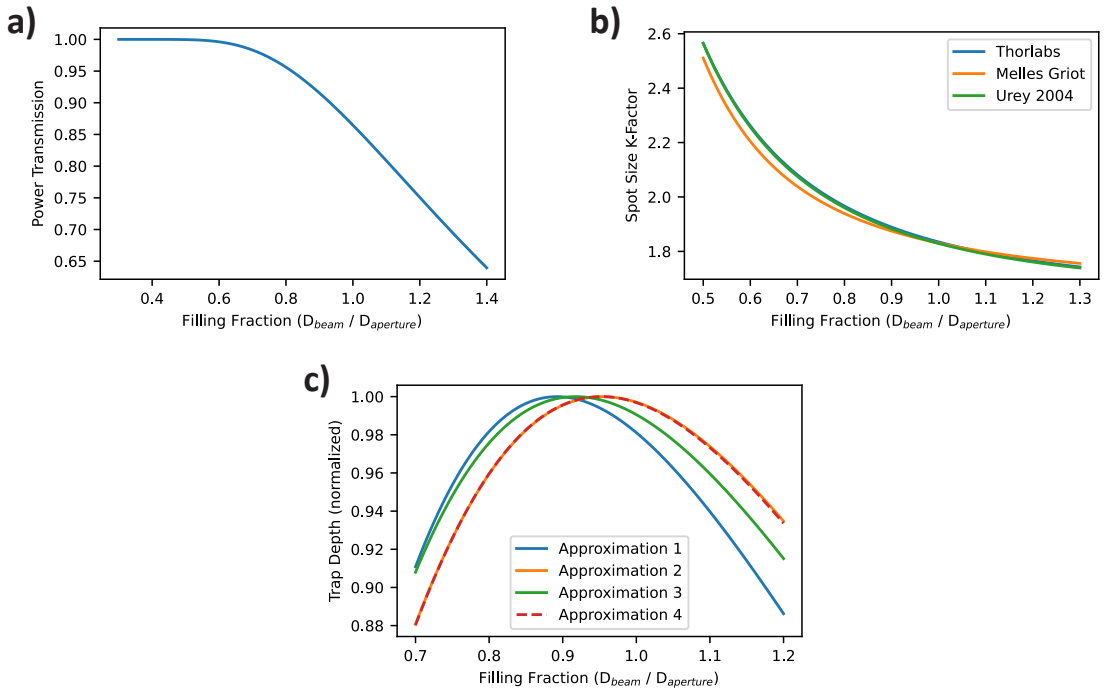

Figure 3.8: **Optimizing trap depth as a function of the objective lens filling fraction.** **a**, Power transmission of a Gaussian beam through a circular aperture as a function of the filling fraction. **b**, Various polynomial fits of the K-factor or spot size factor [116, 117, 115]. **c**, Normalized trap depth as a function of the objective filling fraction accounting for both the power transmission and change in focal spot size. The first approximation is calculated from the formula for the peak irradiance of the focal plane derived in Ref. [115], normalized to assume uniform input power. The remaining curves are calculated from the ratio of the power transmission to the square of the spot size from each of the K-factor fits in **b**.

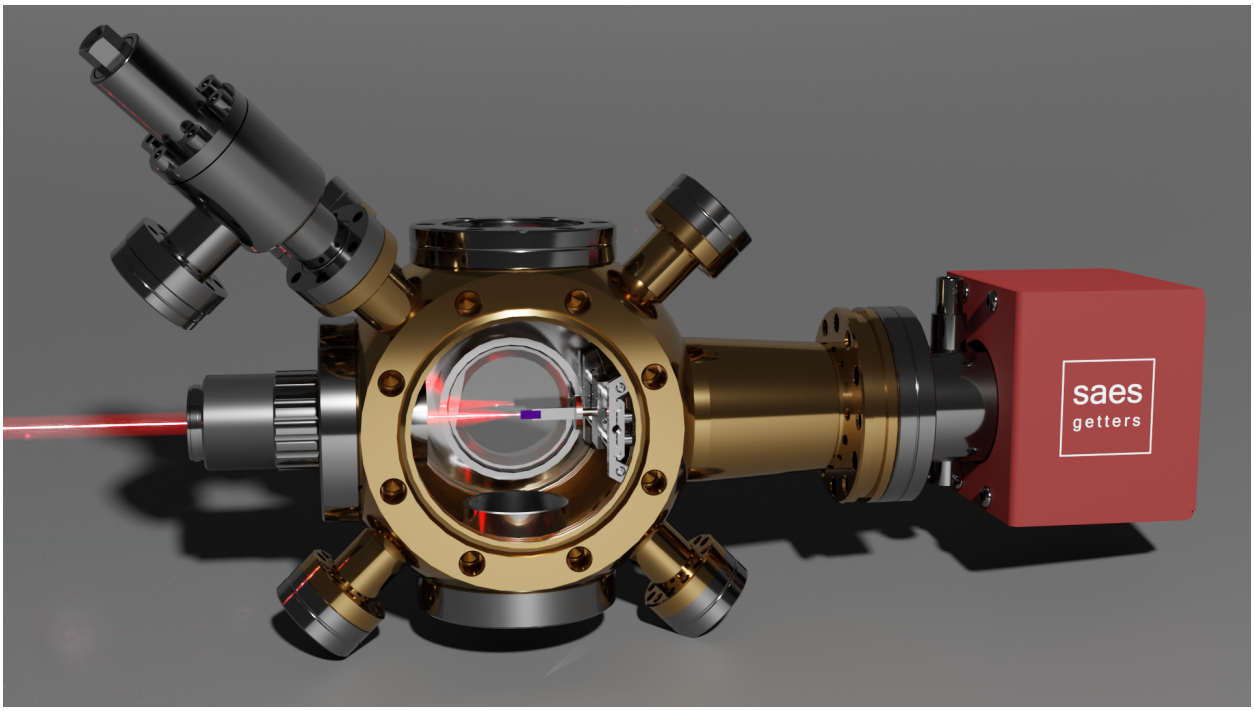

Figure 3.9: **A realistic rendering of our vacuum chamber with the front flange removed made in Blender.** Here, the free-space coupling beam path is shown explicitly.

3.2 Vacuum Chamber

An ultrahigh vacuum (UHV) environment is essential for our experiments, as collisions with background gas particles will eject atoms from the optical tweezer traps. In recent years, many atom array experiments have opted for a modular vacuum chamber design, separating the "source cell" from the "science cell" with a differential pumping tube. The motivation for this arrangement is to minimize the background pressure in the science cell near the atom array and decouple that local pressure from the operation of the atom source. In order to generate reasonable atomic flux through the differential pumping tube, a 2D MOT is typically created in the source cell, a push beam guides these atoms through the differential pumping tube into the science cell, where they are captured and further cooled in a 3D MOT. These two cells tend to be made entirely of glass to maximize optical access.

Our vacuum system, on the other hand, foregoes this design in favor of a more traditional

steel chamber. The primary motivation for this choice was to have a simple and robust mounting structure for our nanophotonic chip. While nanophotonics have been mounted in glass cells on long mounting arms [118] as well as via silicate bonding directly to the wall of the glass cell [94], it is much more straightforward to construct a mounting system in a steel chamber. Our mount consists of a pair of groove grabbers that attach to the interior of the chamber connected by two metal rods that hold a modified commercial scanning electron microscope (SEM) mount. This modified SEM mount clamps down with a screw to hold our chip.

Our custom Kimball Physics stainless steel vacuum chamber has two 4.5-inch ConFlat (CF) flanges with re-entrant "bucket" windows (MPF Products), enabling our objectives to lie within their 15.6 mm working distance of the chip mounted at the center of the chamber. Our objectvies are glass corrected for the 3.5 mm thick glass used for the windows. The orthogonal axes are 2.75-inch CF flanges, one of which is modified and extended into a tube to facilitate mounting of our NextTorr Z200 combination ion-getter pump. The chip mount is positioned directly in front of the pump. Opposite to it is another 2.75-inch re-entrant window which is used for free-space coupling of light into and out of our nanophotonic cavities as described in Chapter 3.3.1.

On the bottom of the chamber, a 2.75-inch electrical feedthrough is mounted to the chamber. Two SAES alkali caesium dispenser wires are mounted to the electrical feedthrough and dispense atoms directly toward the chip and MOT region, just a few centimeters away. Only one dispenser is operated at a time, while the second functions as a backup. The dispensers are independently controllable and share a ground connection. A 2.75-inch viewport on the top of the chamber is used to view the inside of the chamber with a small camera for alignment or to inject UV light into the chamber for light induced atomic desorption (LIAD). Five additional 1.33-inch conflats protrude along the diagonals, four of which are used for MOT beams. The fifth connects to a gate valve which is used for the initial pump down

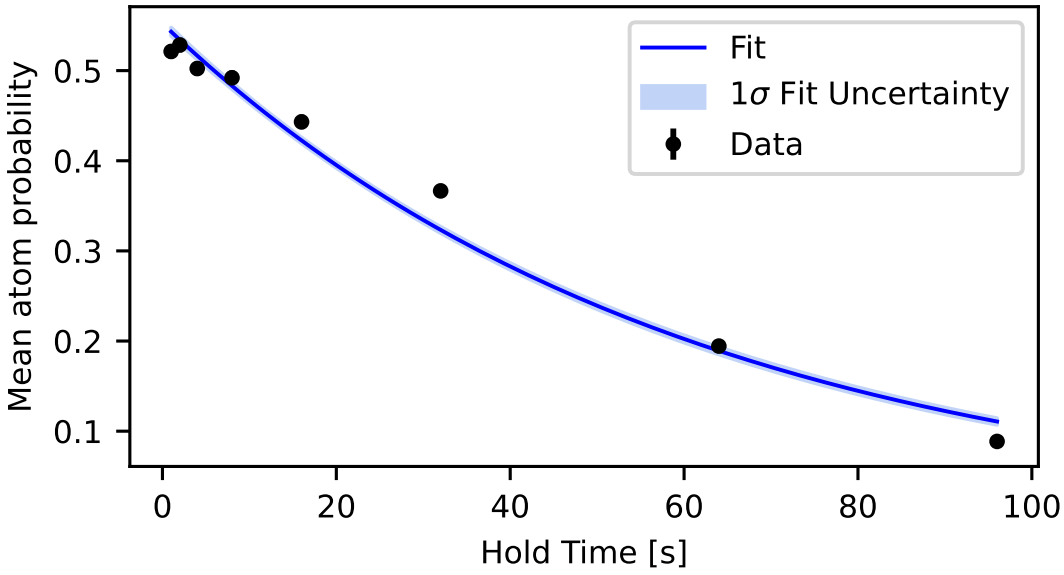

Figure 3.10: **Background limited lifetime of atoms in optical tweezers prior to the chip and mount installation.** The exponential fits yields a lifetime of 59.7 ± 1.2 seconds and a loading probability of 0.552 ± 0.004, typical for the experiment.

from atmospheric pressure with a combination roughing and turbo pump.

In lab tours over the years, many visitors to the lab have expressed surprise that we simply dispense caesium into the main chamber and load directly into a 3D MOT. They have expressed the concern that this would compromise our vacuum considerably. However, this has not been a limitation in practice. We primarily attribute this to the small internal volume of our chamber, which is further reduced by the re-entrant windows. Before installing the chip and its mount into the chamber, we measured background limited lifetimes in our optical tweezers of approximately one minute as seen in Fig. 3.10. After mounting the chip, which partially clips our MOT beams, we increased the dispenser current in order to trade off the MOT loading rate with the background pressure. We primarily operated at a point where our MOT loaded in 100 ms and the atomic lifetimes in the tweezers was approximately 14 seconds as seen in Fig. 4.8.

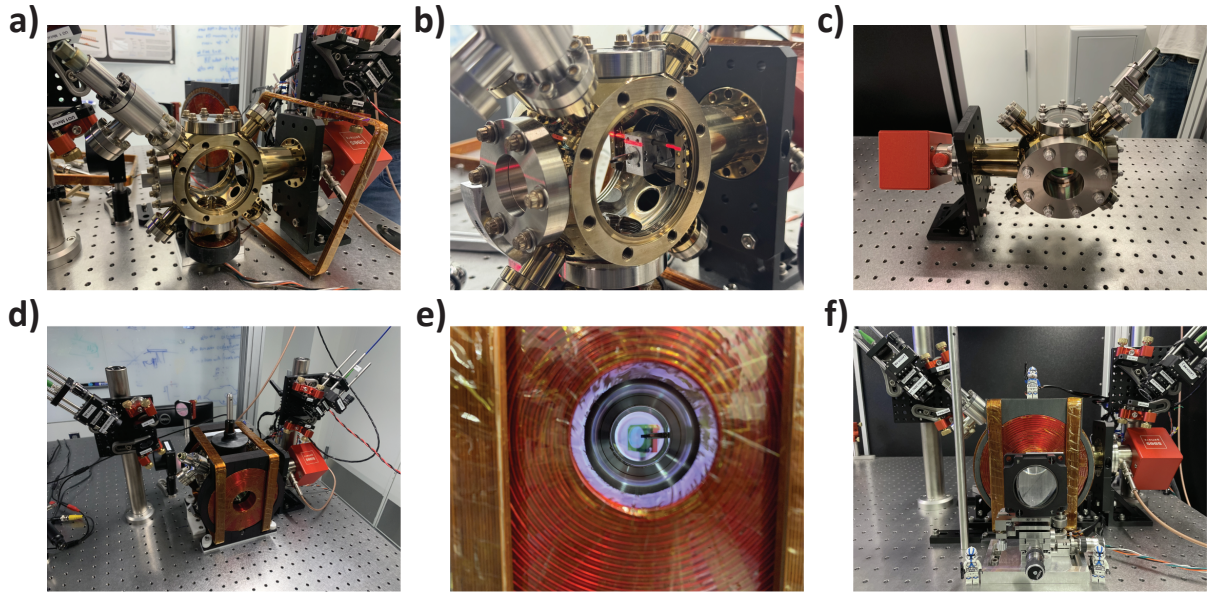

Figure 3.11: **Photographs of our vacuum chamber at various stages of construction.** **a**, Chamber with the front flange removed. The caesium dispensers are visible at the bottom of the chamber. The gate valve is angled towards the camera at the top left of the photo. **b**, The nanophotonic chip is mounted on its modified SEM mount secured into the rectangular base plate by two vented set screws. The base plate is mounted on two horizontal rods which are secured in place by two groove grabbers at the edges of the open chamber flanges. A laser level reference is used to assist in alignment. **c**, The fully assembled chamber on a Kimball mount. **d**, The fully assembled chamber with the magnetic field coils and MOT optics constructed. One axial MOT beam reflects off of the 2-inch mirror in the background and propagates along the axis of the objectives which have not yet been installed in this photo. The diagonal MOT beams are delivered via the optics mounted to the two small breadboards affixed to the two large posts next to the chamber. They are retroreflected by mirrors mounted on the white 3D printed angled mounts. **e**, A view of the nanophotonic chip along the optical tweezer axis with the objectives removed. **f**, The fully assembled chamber with the objective telescope assembly mounted on its translation stage. The manual screw which adjusts the focus of the tweezers has since been replaced with a piezoelectric screw for our auto-focusing protocol.

3.2.1 Magnetic Field Coils

In order to control the magnetic field environment in our chamber, we have surrounded the chamber with four pairs of magnetic field coils custom-built by Custom Coils, Inc. One pair of coils is oriented along the optical tweezer axis and set up in an anti-Helmholz configuration to generate the quadrupolar magnetic field gradient needed for the MOT. These gradient coils are mounted just inside a slightly larger pair of coils arranged in a Helmholtz configuration to provide a static offset field along this axis. Our high NA objectives are mounted such that they extend through the centers of these two coil pairs into their respective re-entrant windows. The final two pairs of Helmholz coils are oriented along the two orthogonal axes. The pair along the axis defined by the SAES pump and coupling re-entrant are large and square due to the geometric constraints surrounding the chamber. The coils along the vertical axis are quite small and circular deviating slightly from an ideal Helmholtz condition. Despite this, the magnetic field they produce is quite uniform over a roughly 1 cm region around our atom array, though crosstalk between this pair of coils and the other axes is slightly more pronounced and measurable in the experiment due to their geometry.

The three large pairs of coils are all mounted on custom 3D-printed mounts made of glass bead infused nylon 6,6. These mounts are affixed to the optical table and the large 3D printed washers used to clamp them assist in holding the square coils in place. The final small pair of coils along the vertical axis is also housed within similar 3D printed mounts, which are instead secured and referenced to the chamber mounting structure directly. This ensures that their central axis is well aligned to the center of the chamber. The vacuum chamber itself is supported by a custom metal clamp on the 4.5-inch flange, on the tweezer output side of the chamber. A secondary Kimball mount supports the chamber at the SAES pump connection point as a redundancy, though this mount is not fully tightened to prevent applying any torque on the chamber.

3.2.2 Optics Layout

A simplified schematic of the beam delivery optical layout surrounding the vacuum chamber is shown in Fig. 3.12. This diagram illustrates how many of the laser beam paths are combined with dichroic mirrors and routed to the vacuum chamber along a single optical axis through the tweezer input objective. This enables all of these beams to be delivered to the atoms while they are trapped above the nanophotonic cavities.

These lasers include the 895 nm and 1470 nm beams used for the atom-telecom photon entanglement scheme first described in Ref. [119] and summarized in Chapter 5.1, a 1064 nm beam used for cavity frequency stabilization as described in Chapter 3.3.3, the 935 nm optical tweezers, and the 852 nm axial MOT beams described in the next section. Addtionally, a separate 852 nm beam from the fast pulse generation setup is merged into the MOT beam path to achieve a higher Rabi frequency for use in the atom-telecom photon entanglement protocol.

For imaging, we use a dichroic to separate out the atomic fluorescence from the main input beam path. The atomic fluorescence is collected in reflection via the tweezer input objective for improved stability and suppression of background light from the optical tweezers near the imaging frequency. Our imaging is performed utilizing the background-free method described in Chapter 4.2.

3.2.3 MOT

An unusual feature of our magneto-optical trap (MOT) is that two of the six beams are input through the high NA objectives along the optical tweezer axis. This configuration is atypical because it complicates standard fluorescence imaging. Specifically, the imaging objective collects the counter-propagating MOT beam, which is significantly brighter than the atomic fluorescence and at nearly the same frequency. This makes it difficult to isolate the atomic fluorescence signal. Fortunately, the background-free imaging technique we de-

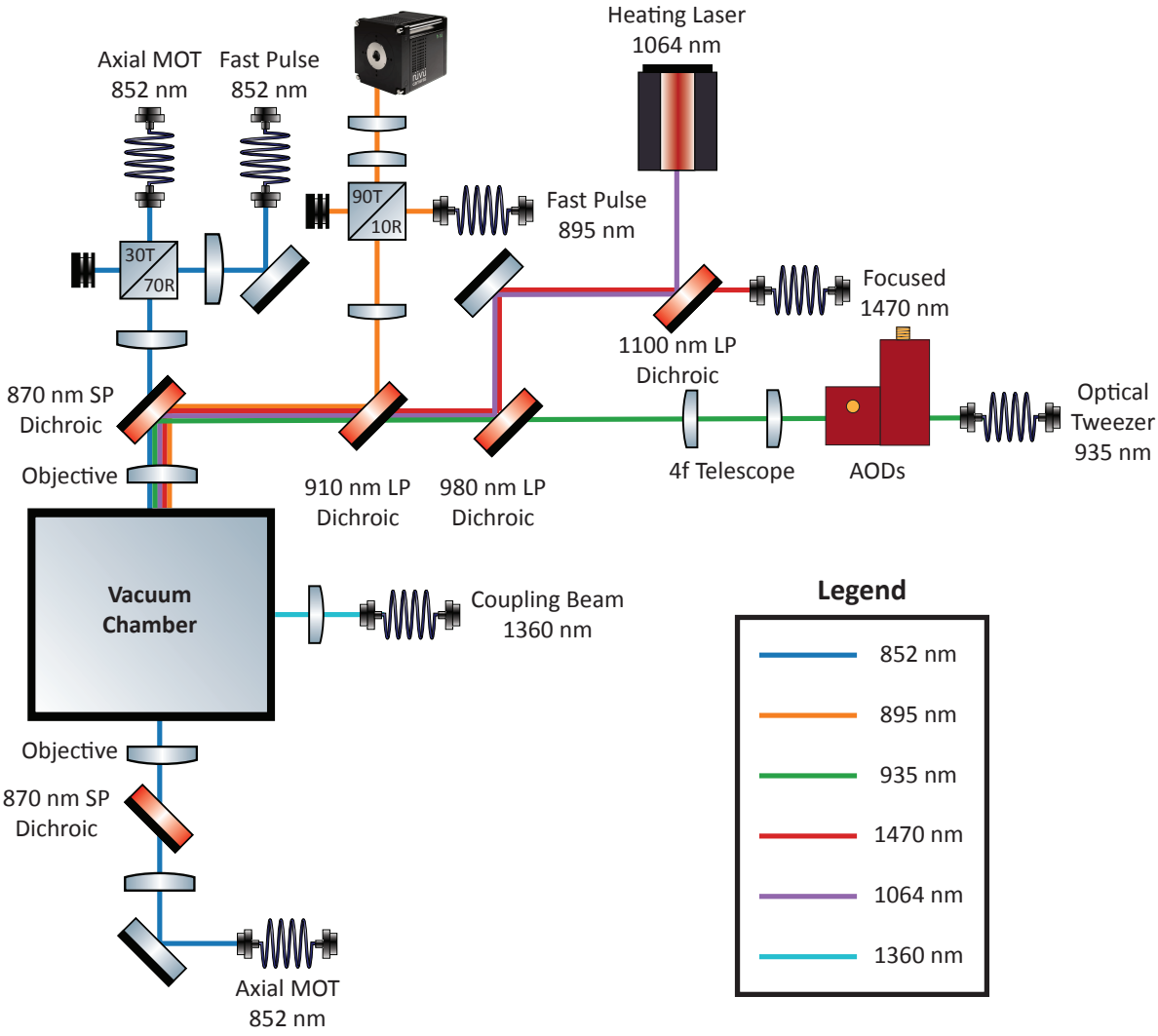

Figure 3.12: **A simplified schematic illustration of the optical beam delivery layout around the vacuum chamber.** This figure was made using Alexander Franzen's Component Library [102]. For an alternative depiction of this layout, see Shankar's thesis [120].

veloped to address the similar challenge of bright scattering from our nanophotonic chip also addressed this challenge.

Several alternative solutions to this challenge were considered but not pursued. The first was to re-design the vacuum chamber geometry to support an eight-beam MOT, removing the 852 nm beam path from the objective axis. Another solution involves implementing a two-color MOT [121, 122], using 1470 nm light for the axial MOT beam. This wavelength can be easily spectrally separated from the atomic fluorescence and our camera is not sensitive to it. Other groups have addressed similar challenges by boring a hole through the center of their objective or using a small mirror in the back focal plane to pick off focused MOT light [123].

Delivering the MOT beams through the objectives introduces a couple of additional design considerations. First, retroreflecting the beam on this axis is impractical due to the loss of optical power traversing the objectives, which would cause an intensity imbalance along the axial direction. In order to address this, we align two counterpropagating beams outcoupled from separate fiber outcouplers through each of our objectives such that they experience symmetric losses. Second, since the objectives themselves are strong lenses, it is difficult to achieve a large collimated beam along this axis inside the chamber. As a result, our diagonal MOT beams are approximately 1 cm diameter, while the axial MOT beams are only around 1 mm in diameter.

Two floating broadboards perpendicular to the optical table are mounted onto two thick posts secured next to the vacuum chamber. These breadboards contain fiber outcouplers, polarization optics, and mirrors to align the diagonal MOT beams through the chamber. The breadboard on the coupling beam side, opposite from the SAES pump, additionally combines the 1470 nm beam used in our imaging protocol onto the MOT beam path for delivery into the chamber. This 1470 nm beam is not focused down as tightly as the one routed through the objective which is used in the telecom photon entanglement protocol. Both beams are

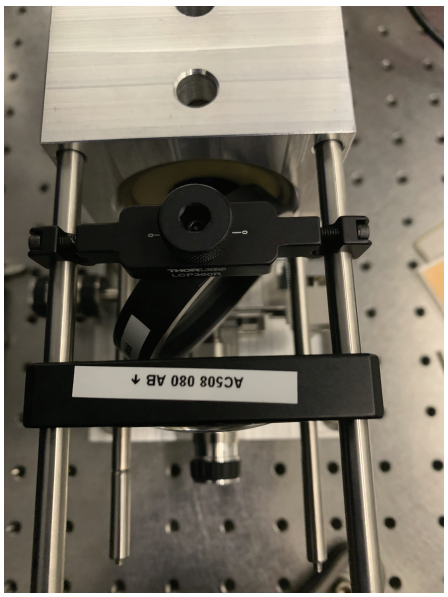

Figure 3.13: **A photograph of the axial MOT beam telescope assembly and dichroic used for beam combining.**

sourced from the same laser setup and a fiber-optical switch is used to control which path the beam takes to the chamber.

The axial MOT beams are collimated by telescopes that reduce their beam sizes down from almost 2 inches at the telescope input using an 80 mm focal length lens. The design of this telescope was constrained by the need to incorporate a 2-inch diameter custom short-pass dichroic between the first lens and the objective. This dichroic is used to combine many other beam paths that must be focused inside the chamber and thus cannot traverse the telescope. The fast pulse 852 nm beam path incorporates an additional lens before merging with the MOT beam path such that it can be focused into the chamber. To minimize beam clipping, the thickness of the dichroic mount was reduced in-house at the machine shop. The entire telescope and dichroic assembly is self-referenced using a cage rod system and mounted on a Newport 561-TILT two-axis tip-tilt stage atop a Newport 562-XYZ three-axis precision translation stage. This configuration provides full five-axis control for precise alignment. A photograph of the telescope and dichroic assembly can be seen in Fig. 3.13.

The objectives themselves are angled carefully to match the slight tilt angle of the re-entrant window glass. Similarly, when mounting the nanophotonic chip, its angle is adjusted to match the glass angle such that all three components, the objectives, the glass, and the chip, are as close to coplanar as possible.

Our MOT beams are partially clipped inside the chamber by the chip and its mounting structure. Initially, it was unclear to what degree this would compromise the performance of the MOT. Fortunately, we found that while this clipping renders the MOT slightly more sensitive to the beam alignments, it nonetheless cools and traps atoms reliably. The clipping is primarily on one side of the MOT, introducing an escape pathway for some atoms where the cooling is not as effective and causing it to load at a slower rate. Experimentally, we found that the MOT itself is quite robust to the ratio of intensities between the axial and diagonal beams, however, the efficiency of loading atoms from the MOT into the optical tweezers is highly sensitive to this ratio.

3.2.4 Custom Oven

Replacing the nanophotonic chip requires venting the vacuum chamber to atmospheric pressure, a process that necessitates re-baking to restore UHV conditions. This challenge has been addressed in the literature with a load-lock chamber design where the chamber is partitioned into sections by a valve [124]. This design enables the user to maintain UHV in the main section of the chamber while venting only the partitioned section during chip replacement. We instead opted to keep our chamber as small and compact as possible. We designed and built a custom oven to streamline and automate the baking process of the fully assembled chamber following a chip replacement.

Our first bake was performed using heating tapes controlled manually by variable AC transformers. The heating tape was wound around a layer of thermal insulation surrounding the chamber and further encases in a second layer of thermal insulation. This approach,

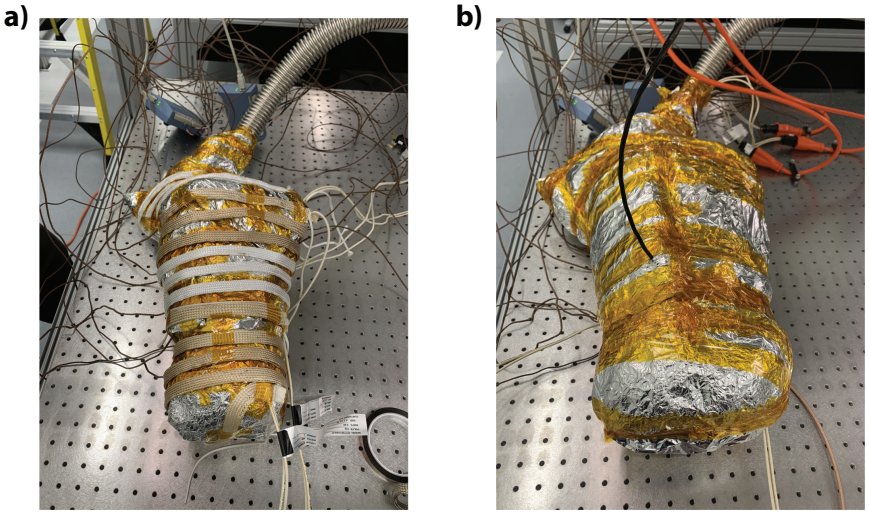

Figure 3.14: **Photos from our initial, manually controlled bakeout. a**, Thermocouples were attached to the chamber before it was encased in a layer of aluminum foil and fiberglass insulation. Heating tapes, manually controlled with variable AC transformers, were wrapped around the insulation layer. **b**, An additional layer of aluminum foil and fiberglass insulation encases the heating tapes.

while effective, was clearly not a sustainable solution for future bakes as the process was quite tedious. This was largely due to our chamber's thermal constraints, which require limited heating and cooling rates under 10°C per hour and minimal thermal gradients across the chamber, particularly across the glass-to-metal transitions of the windows. These requirements demanded constant monitoring and frequent fine adjustments to the transformers to ensure slow, even heating and cooling of the chamber.

To address this, we designed and built a custom oven to automate the baking process. The oven is constructed from half-inch thick aluminum walls bolted together with 1/4"-20 screws. Custom silicone heater pads (Phoenix Thermal Supply) with integrated, internal Type J thermocouples are affixed to the outer surface of each wall using a high temperature 3M adhesive. These heaters were designed with cutouts aligned to feedthrough holes machined into the oven walls. These holes were designed to accommodate the vacuum tubing connection from the chamber to the roughing and turbo pump for the initial pump

down, electrical feedthroughs to power our NextTorr Z200 combination ion-getter pump, and additional thermocouples to monitor the temperature profile across the chamber and oven interior. The heaters can operate continuously at 190-200°C and up to 230-240°C for short periods. At high temperature, the temperature profile across the over interior is highly uniform with a typical peak thermal gradient of less than 3-5°C, comparable to the accuracy of our Type J thermocouples.

The heaters are controlled by a commercial ramp-and-soak PID controller (Omega Platinum Series CN8DPT-444), which outputs DC pulses to several solid-state relays (Omega SSRL240DC25) that regulate the 120 V AC power supplied to the heaters. This setup allows the user to program temperature over time profiles, automating the entire bake process, including gradual ramps to the target temperature, extended high-temperature holds, and slow cooldowns. A monitoring system alerts the lab team via email and Slack if temperature readings exceed preset limits or if thermal gradients across the oven interior become too large. This system reads in thermocouple temperatures using a Measurement Computing USB-TEMP data acquisition system and the alerting is controlled via a remotely accessible Grafana dashboard which logs the bake temperature profile.

As an additional safety measure, a high-temperature grounding wire is connected to the oven walls to protect against an unlikely failure mechanism where the internal wiring of the heaters short to the oven walls. Inline 15 A fact-acting ceramic fuses protect each heater circuit and are designed to trip before the lab's 20 A circuit breakers in case of a short. The heaters draw significant power, as the top and bottom pair of heaters are rated at 910 W each, the right and left wall heaters are 490 W each, and the front and back wall heaters are 980 W each. This totals approximately 40 A of current draw at 120 V AC, assuming a unity power factor. The system is therefore distributed across four independent electrical circuits, each drawing less than 15 A. Overall, this oven significantly reduces the manual effort required for baking by completely automating the process and ensuring that

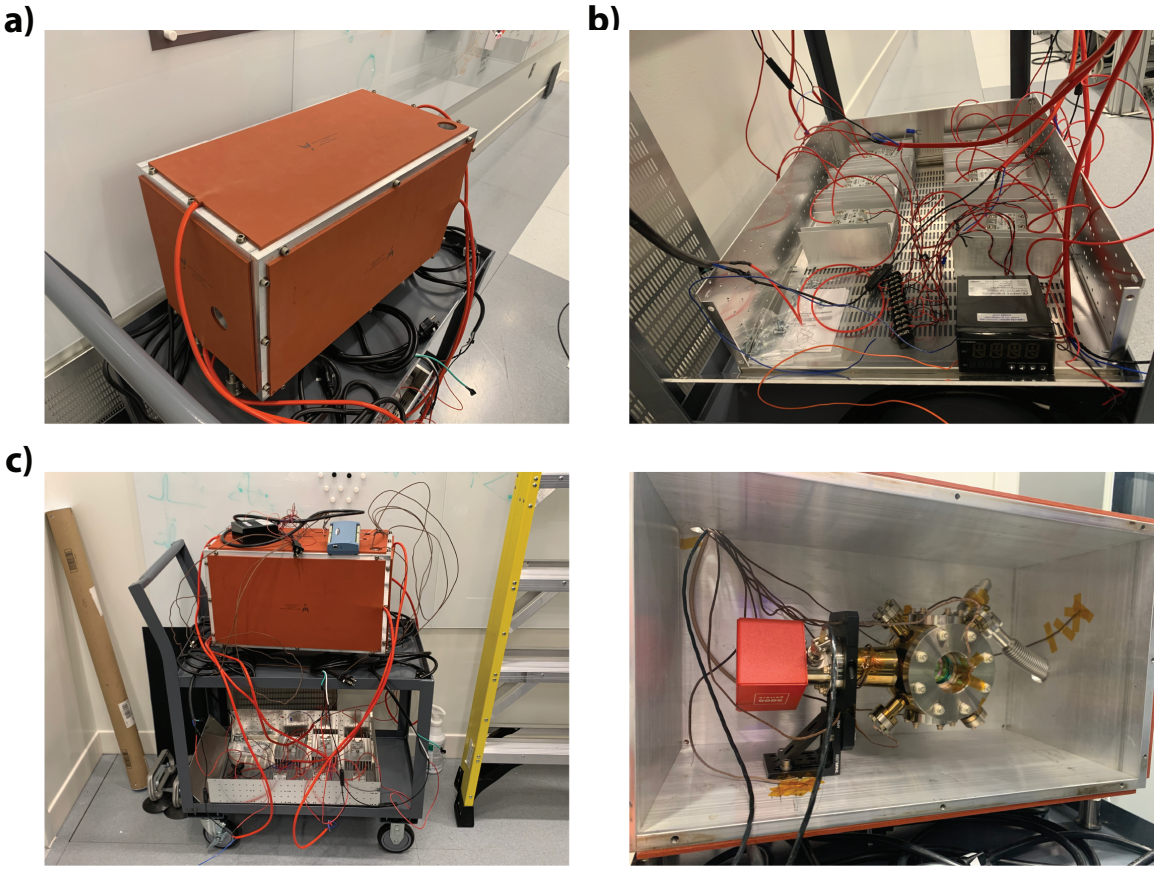

Figure 3.15: **Images of the custom aluminum oven used for automated baking. a**, The fully sealed oven mounted on a cart with two of the heater/wall feedthroughs visible. **b**, The electrical control box with the lid removed. The six solid-state relays are each mounted on heatsinks in the back and the PID control box can be seen in the front right. **c**, The two layer cart assembly with the blue data acquisition module resting on top of the oven. **d**, The vacuum chamber mounted inside the oven with the SAES pump power provided by the feedthrough in the top left and the roughing and turbo pump connection connected to the gate valve and routed out via the feedthrough on the right. Kapton tape is used to affix the thermocouples in place inside the oven.

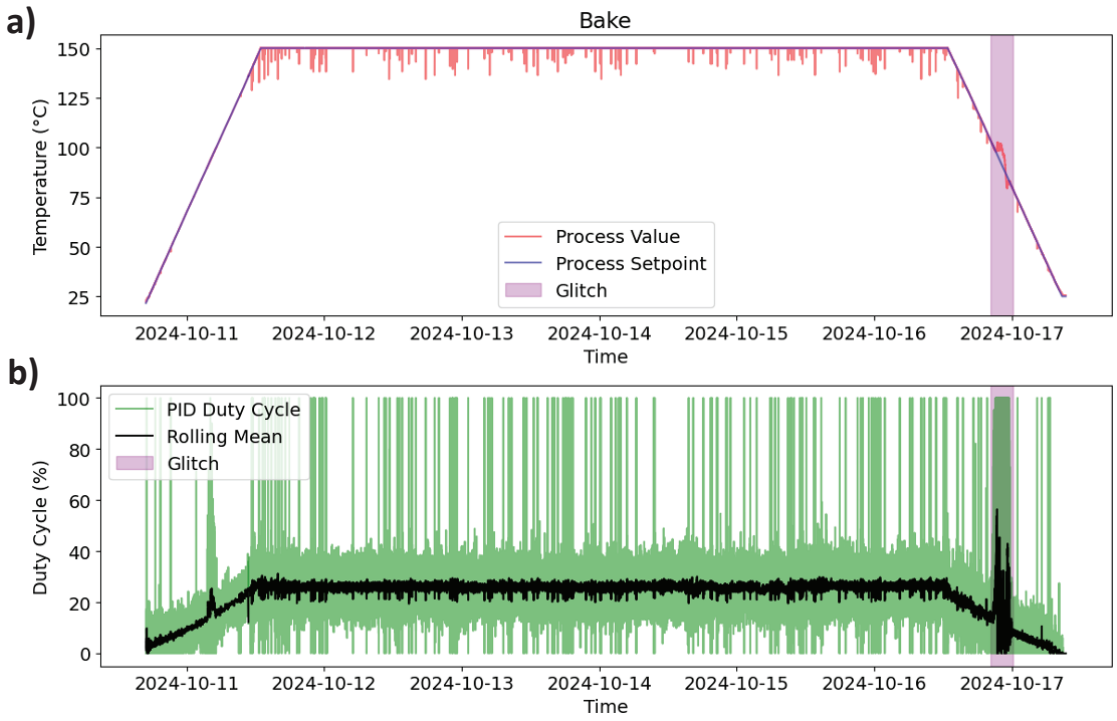

Figure 3.16: **An example temperature over time profile from an automated oven bake. a**, The temperature readings over time recorded by the PID controller plotted alongside the setpoint over time. A small transient deviation is marked as a glitch. **b**, The PID controller duty cycle, or the fraction of time for which the heaters are active, with its rolling mean overlaid. The PID began to ring about the setpoint with a peak to peak amplitude of about 10 degrees over the course of two hours before re-stabilizing at the indicated glitch region for this bake.

the thermal requirements of the chamber are met throughout each bake.

3.3 Nanophotonic Chip

This section provides a brief high level overview of the key design features of our nanophotonic chip. For an in-depth discussion of the chip design principles and nanofabrication process, refer to Shankar Menon's thesis [120].

The nanophotonic chip is fabricated from commercially sourced wafers consisting of a 330 nm thick layer of silicon nitride atop a 500 μm thick silicon base layer (Silicon Valley Microelectronics). The photonic crystal cavities are patterned into the silicon nitride layer

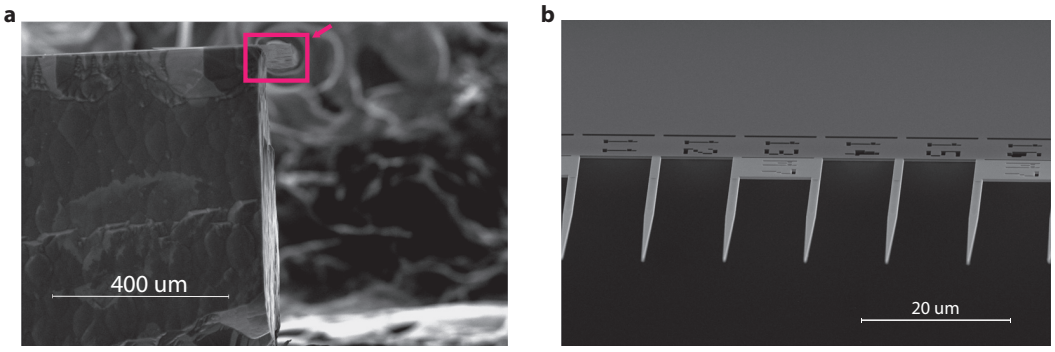

Figure 3.17: **SEM images of the nanophotonic chip displaying the cantilevered nanophotonic cavities overhanging the edge. a**, The red box marks the devices, fabricated at the top from the silicon nitride layer of the chip, above the silicon base layer. The silicon base layer is undercut beneath the devices by etching the chip from the side. **b,** An SEM image of the cavities taken from the angle marked by the red arrow in **a**. This figure was originally published in the Supplementary Information of our paper, Ref. [31].

using electron beam lithography. The wafer is diced such that the cavities are aligned to the edge of the chip structure. The silicon base layer is completely undercut from the device region, leaving behind the cantilevered cavities overhanging the edge of the chip. The final lateral dimensions of the chip are approximately 2 mm $\times$ 7 mm.

The semi-open chip geometry, with the cavities overhanging from the 2 mm edge, is a key feature enabling integration of the chip with our free-space atom array. The undercut of the silicon base layer is also essential as it prevents the optical tweezers from heating and reflecting off of the base layer while translating the atoms to load them onto the cavities.

The chip edge hosts $\sim$150 cavities spaced by 11 μm. These cavities are divided into three sections, of 50 cavities each, with each section hosting a slightly different design. The number of holes used to define the Bragg reflector on the outcoupling edge of the photonic crystal cavities varies across the sections. Increasing the number of holes enhances the reflectivity of the Bragg mirror, improving the quality factor of the resonance and reducing the outcoupling efficiency. The three sections allow us to experimentally explore this trade-off without replacing the chip.

3.3.1 Free-space Coupling

We couple light in and out of our nanophotonic cavities via free space. This section reviews the main concepts of our coupling technique, while a more detailed discussion can be found in Shankar Menon's thesis [120].

Two common methods used to couple light to nanophotonic devices utilize tapered fibers and lensed fibers. In the tapered fiber approach, direct contact is made between the tapered fiber and the nanophotonic. As the fiber diameter adiabatically decreases, the optical mode shifts from being well contained within the fiber core into the evanescent field surrounding the fiber. This evanescent field can strongly overlap with the nanophotonic mode and faciliate the efficient transfer of optical power into the nanophotonic device. In the lensed fiber approach, a lensed fiber tip is carefully aligned microns away from the end facet of the nanophotonic device to focus light and inject it into the end facet. Both of these methods can achieve high coupling efficiencies [90, 125, 126, 127, 128].

For our system, which emphasizes scalability of both the atom array and the number of cavities on the chip, these methods pose significant practical challenges. Accomodating tens to hundres of fiber feedthroughs, alongside the inevitable reduction in optical access and further obstruction of beam paths in the chamber, is impractical. A piezo-actuated stage inside the chamber to enable re-positioning of fewer fibers to new cavities is conceivable, though this would require significantly increasing the size and complexity of our chamber.

Instead, we decided to pursue a free space coupling technique inspired by the methods developed in the Kimble group [94]. Unlike their Y-coupler designs, we opted for a simpler tapered waveguide geometry where adiabatically tapered waveguide regions are appended to the outcoupling edge of our photonic crystal cavities. The end width of these tapered waveguides is chosen to maximize the modal overlap of the ejected mode and a focused Gaussian beam provided by a coupling lens. This coupling lens is mounted outside the vacuum chamber on a 5-axis translation stage, similar to the system used for our high NA

optical tweezer objectives.

Theoretically, this simple tapered waveguide method can achieve coupling efficiencies exceeding 90%, as indicated by the Lumerical FDTD simulations shown in Fig. 3.18. Experimentally, we have measured coupling efficiencies as high as 64% in our nanophotonic characterization setup, though we have been limited to lower coupling efficiencies around 20% in the vacuum chamber. We identified the geometric constraints limiting this number, caused by an inability to bring the optimal coupling lens close enough to the chip. In the most recent chip replacement and vacuum bake, we exchanged the re-entrant window for a longer version to address this. This approach provides us with the flexibility to switch between cavities completely externally and offers future scaling compatibility with multiplexing. For example, a fiber array paired with an appropriate telescope can map the outcoupling edges of multiple cavities to the fiber array. Alternatively, the light could be routed through on-chip waveguides or outcouplers for external coupling.

3.3.2 Nanophotonic Characterization Microscope

In order to characterize our nanophotonic chips and provide feedback to iterate on the nanofabrication process, we designed and built a custom microscope equipped with a short wavelength infrared (SWIR) camera (Raptor Photonics Owl 640 M). The SWIR camera enables the user to see the telecom wavelength coupling beam, which standard silicon based camera sensors are insensitive to, and precisely align it to the cavities. The characterization setup can also operate utilizing tapered optical fibers for coupling to the cavities.

The characterization setup consists of two high-precision translation stages (Newport 562-XYZ), enabling independent positioning of the chip and the coupling apparatus with respect to the microscope objective lens. One stage hosts a mounting structure for the chip, while the other contains the coupling optics, either a free space coupling lens or a mount for a tapered optical fiber. For imaging and alignment, we use a 0.42 NA NIR-coated commercial

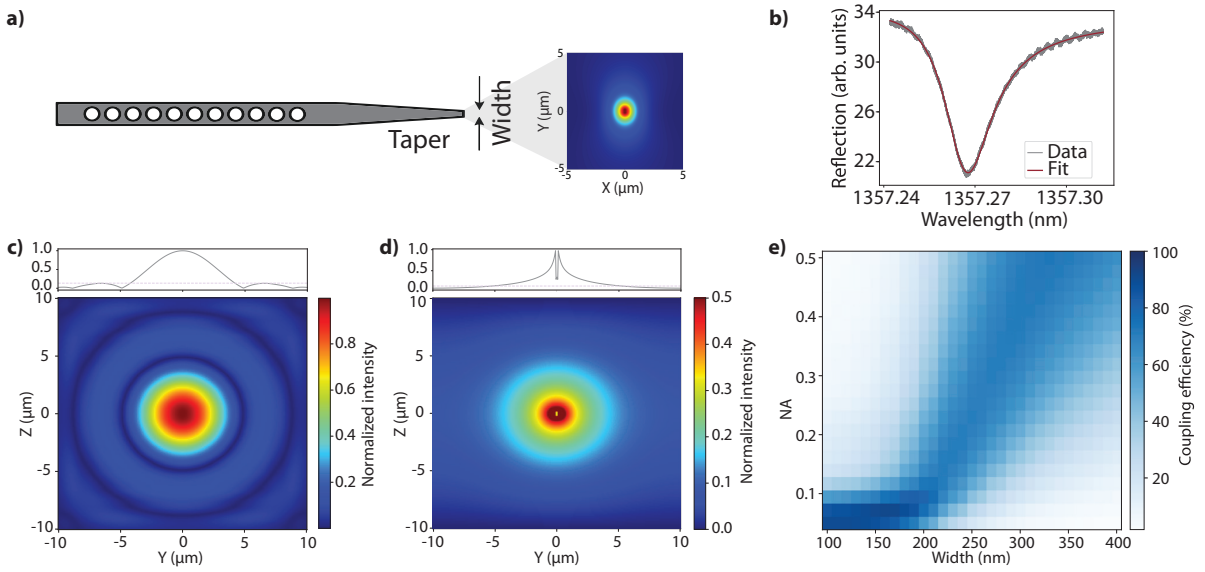

Figure 3.18: **Free-space coupling of light to the nanophotonic crystal cavities.** **a**, Schematic illustration of an adiabatically tapered waveguide appended to the photonic crystal cavity and the ejected mode profile. **b**, A typical cavity reflection spectrum from a cavity mounted on the chip inside our vacuum chamber taken via this free space coupling technique. **c**, Simulated intensity profile of a diffraction-limited focal spot from a 0.17 NA lens. The top panel shows a line cut along the Y axis at Z=0 and the dashed horizontal line indicates the $1/e^2$ amplitude. **d**, The simulated profile of the second TE mode supported by the end of the waveguide taper with the corresponding line cut displayed along the top panel as in **b**. **e**, The estimated coupling efficiency from Lumerical FDTD simulations as a function of the NA of the coupling lens and the end width of the taper. This plot assumes a constant waveguide thickness of 330 nm. Parts **b**–**e** are adapted from our published work, Ref. [31].

microscope objective lens (Boli Optics) along with a 200 mm focal length microscope tube lens (Thorlabs). We introduce an LED light source with a 50/50 beamsplitter positioned in the infinity space between the objective and the tube lens.

Our photonic crystal cavities are designed to be near resonant with the caesium transition between the $6P_{3/2}$ and $7S_{1/2}$ states at 1359.2 nm. Around this wavelength, strong water vapor absorption lines appear in our spectra due to vibrational modes of water molecules. These manifest as cavity-like dips in the reflection spectra. They appear very similar to cavity resonances with quality factors in the tens of thousands, complicating the process of identifying true cavity resonances. To mitigate this challenge, we have thoroughly characterized these absorption features and mark them on our cavity scans to avoid misidentification. As expected, the magnitude of these absorption features depends strongly on the free space propagation length, making them significantly less pronounced when coupling via tapered fibers.

3.3.3 Cavity Frequency Stabilization

In order to couple atoms to the cavities, the cavity resonance must match the atomic transition frequency. We therefore require the ability to tune and stabilize the cavity resonances while they are mounted inside the vacuum chamber. We employ an established thermal tuning method which uses an external laser to heat the cavities and redshift their resonances [24]. This technique provides a tuning range of $\sim$2 nm in our system, though the frequency shift is inherently unidirectional towards longer wavelengths since the cavities can only be heated with this method. The underlying mechanism exploits the temperature dependence of silicon nitride's refractive index.

In our implementation, we aim a 1064 nm laser (Aerodiode 1064LD-1-1-2) at the base of the cavity. This choice of wavelength may seem unusual considering silicon nitride's large bandgap corresponding to ultraviolet wavelengths around 230-275 nm, rendering the

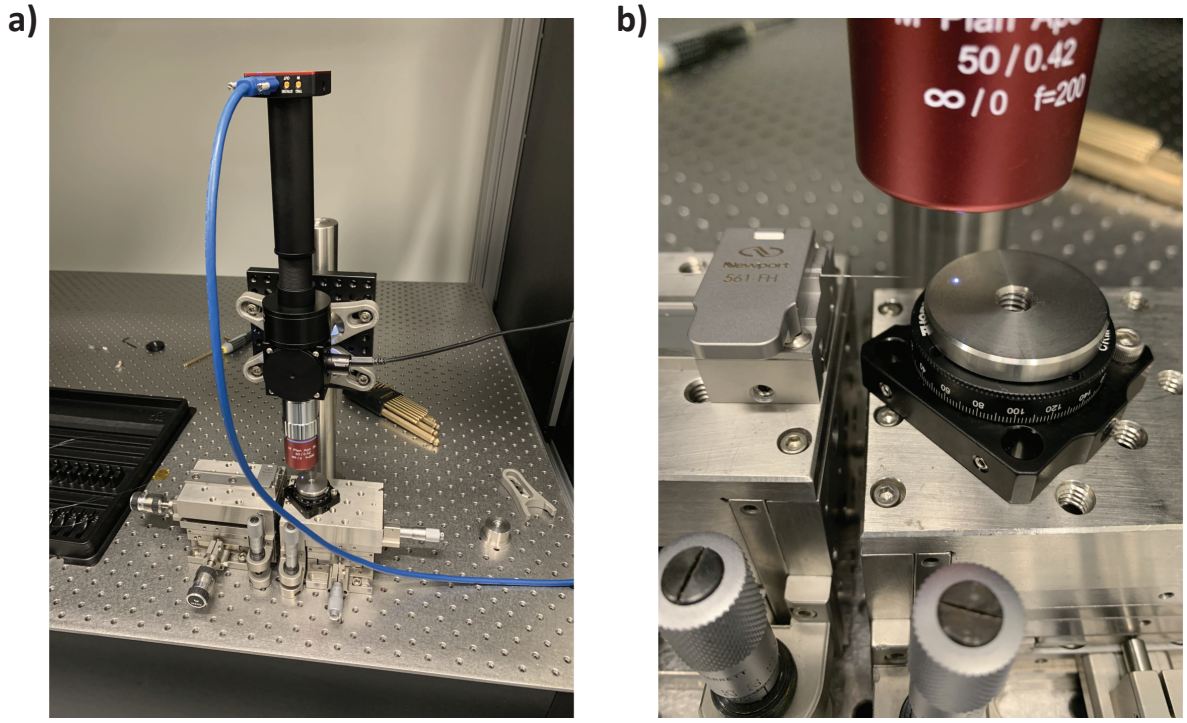

Figure 3.19: **Photographs of our nanophotonic characterization microscope. a**, The full microscope setup with two high precision three-axis translation stages beneath the objective. Here, a ThorCam is used for imaging at the top of the microscope assembly, which has since been upgraded to a SWIR camera that is sensitive to the telecom coupling beam wavelength. **b**, A zoomed in view of the original tapered fiber, which has since been swapped out for a free space setup similar to the one used in our experiments. The steel mounting surface held in the rotation mount shown here has also since been upgraded to an SEM mount similar to the one used in our chamber.

material largely transparent to this beam. However, by aiming at the base of the cavity, this beam can transmit through the silicon nitride layer and effectively heat the silicon base layer underneath since silicon has a much smaller bandgap, corresponding to ∼1107 nm. This heat is then transferred via direct thermal contact to the cavity, tuning its resonance. In this way, we avoid fabricating heater pads onto our cavities as in Refs. [91, 24]. The use of 1064 nm light is also advantageous as it is quite far red-detuned from our caesium transitions, minimizing its impact on our experiments beyond heating of the cavities.

We actively stabilize the cavity resonances using a PID feedback loop controlled by a QNimble Quarto. This feedback is based on the cavity reflection signal. The 1360 nm probe beam we use to monitor to the cavity reflection is of a sufficient power to induce an asymmetry in the cavity resonance, allowing us to use the long tail of the reflection signal for locking slightly off resonance. Ideally, this lock would be engaged at all times, though this would require a secondary cavity mode, as demonstrated in Ref. [91]. Instead, our system freezes the cavity lock mid-sequence upon an external trigger signal. Meanwhile, a fiber-optical switch re-routes the coupling beam pathway from injecting the probe beam to collecting telecom single photons for detection on our superconducting nanowire single-photon detector (SNSPD). The custom programmed PID logic enables a user-controllable offset in the setpoint upon freezing the lock to counteract any thermal changes introduced by the optical tweezer translating to aim directly at the cavity and to shift the cavity directly onto resonance for atom-cavity coupling. We briefly explored alternative PDH and dither locking schemes to lock the cavity directly on resonance instead of the side of fringe lock described here. However, we struggled to obtain a high quality error signal after demodulating due to the weak intensity of the cavity reflection signal, even after employing a highly amplified photodetector.

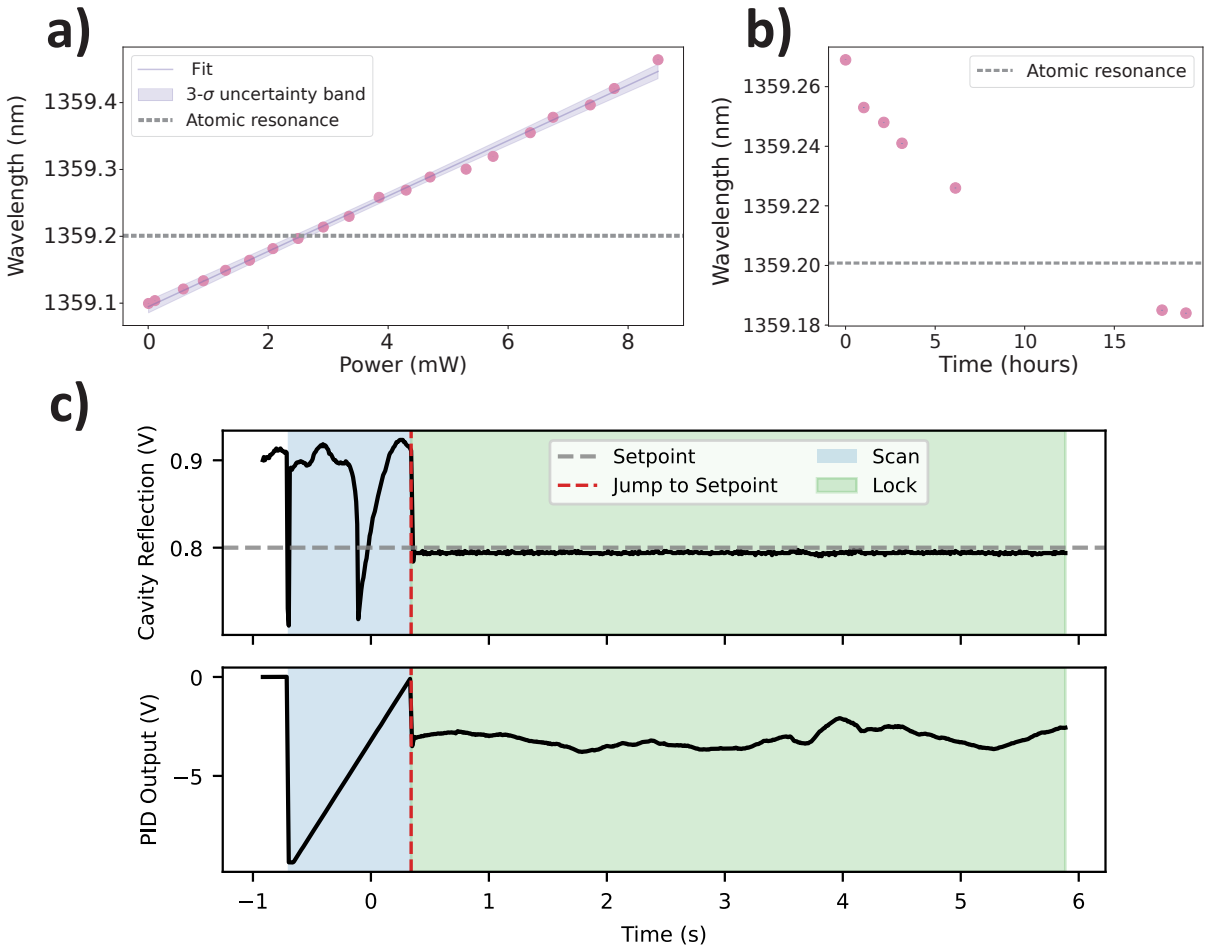

Figure 3.20: **Plots depicting cavity stabilization and drift. a**, The shift of the cavity resonance frequency as a function of the applied 1064 nm heating laser power. This is the underlying mechanism used for our cavity frequency stabilization. **b**, The effect of LIAD in restoring the cavity resonance frequency over time following a long-term redshift due to caesium adsorption on the cavity surface. **c**, An example time trace of our cavity frequency stabilization. The QNimble Quarto contorller begins by scanning the heating laser power, controlled by the PID output via an AOM, and monitors the cavity reflection signal. After the scan, the controller identifies the cavity resonance, jumps the heating laser setpoint close to the user-specified setpoint, and engages the PID.

3.3.4 Cavity Limits

Inside the vacuum chamber, the absence of air removes convective cooling as a mechanism for heat dissipation from the cavities. Therefore, the cavities can only dissipate heat via radiation or conduction through the bulk of the chip. This results in reduced thermal limits with respect to those observed in our characterization setup. To understand these limits under operational vacuum conditions, we conducted destructive testing of our nanophotonic cavities in October 2024, a few months before our chip replacement upgrade in January 2025. These tests involved resonantly driving the cavities with 1360 nm light via the coupling probe beam path as well as heating them to their limits with our 1064 nm heating laser. The results of these tests are detailed in Tables 3.1 and 3.2.

We found that coupling more than ∼1.5 mW of 1360 nm light into the cavities risked approaching the failure thresholds of 2-2.5 mW. To ensure safe operation, we typically operate using sub-milliwatt powers for the coupling beam. For the heating laser, the failure thresholds varied quite broadly depending upon the precise beam alignment. When focused directly on the photonic crystal cavity, powers around 140 mW were sufficient to physically break the cavity in half. Aiming the laser at the base of the cavity, as we do in typical operation, increased this limit. In one case, a cavity lost its resonance after being heated with ∼220 mW of 1064 nm light. This cavity's resonance had redshifted by a maximum of 3.4 nm before it broke and the cavity never showed any physical sign of breakage except that it's resonance no longer appeared in its reflection spectra after this event. To ensure non-destructive operation, we generally restrict our heating laser power to less than 100 mW and limit the applied frequency shifts less than 1-2 nm. These precautions maintain a comfortable margin below the observed destructive limits, minimizing the risk of damage during experiments.

Cavity ID	Limit	Notes
5	2.54 mW	Set laser on resonance, increase laser output in 0.1 dBm steps until breaking point.
6	2.05 mW	Set laser to scan from 1355-1375 nm to ensure we cross the resonance, increase laser power by 1 dBm steps until breaking point.
7	2.59 mW	Set laser to scan from 1370-1372 nm to avoid the cavity resonance, increase laser power by 1 dBm steps until breaking point.

Table 3.1: For each of these cavities, we investigated the maximum power limit of the 1360 nm probe beam. All cavities physically broke in half right around the center of the cavity mode. The optical powers quoted are measured just out of the optical fiber and do not account for the coupling efficiency into the cavities which was not optimized for these experiments. Therefore, these are generous upper bounds and the probe beam should be kept far from these limits to ensure the cavity does not break under high coupling efficiency conditions.

3.3.5 Cavity Degradation

The long term stability of the photonic crystal cavity resonances is critical for reliable operation of experiments coupling atoms to nanophotonics. Based on our experiences in lab and anecdotal accounts from colleagues working on similar experiments, the observed long-term drift behavior and the efficacy of experimental techniques used to counteract these drifts vary widely. Here, we summarize the key phenomena observed with our cavities over the past several years.

In our system, the primary source of resonance shifts over time appears to be the adsorption of caesium onto the cavity surfaces, resulting in a slow redshift of the resonances over time. The rate of this effect clearly correlates with the rate at which caesium is dispensed into the chamber. To counteract these shifts, we employ light-induced atomic desorption (LIAD), using a high power ultraviolet LED to desorb caesium from the cavity surface and blueshift the resonances back toward their original frequencies, as seen in Fig. 3.3.3. As expected, activating our dispensers, a process which is known to introduce background vapor into the chamber, has also caused redshifts and slight quality factor reductions across our cavities. These shifts were more robust against LIAD and must be accounted for in fabri-

Cavity	Alignment	Limit	Notes
8	Cavity Base	N/A	Did not break at max power of ∼337.5 mW.
8	Cavity Center	337.5 mW	This cavity broke when we reached the maximum power of the heating laser.
9	Cavity Center	277 mW	N/A
10	Cavity Center	254 mW	N/A
11	Cavity Center	142 mW	N/A
12	Cavity Center	142 mW	We let this cavity sit at each power for a few minutes before increasing the power to ensure that it had fully thermalized.
4	Cavity Base	∼220 mW	For this cavity, we also tracked the resonance shift as we varied the power. At ∼170 mW, we shifted the resonance by 2.1 nm. At ∼195 mW, we shifted the resonance by 2.8 nm. By ∼220 mW, the shift had reached 3.4 nm, though it was not stable and began to experience strong fluctuations. As we continued to heat the cavity, the resonance was lost and was not recoverable after turning off the heating beam. The neighboring cavity also lost any detectable resonance after this. Additionally, at the highest heating powers, the cavity reflection signal reduced, likely due to heating beam induced misalignment.

Table 3.2: For each of these cavities, we investigated the maximum power limit of the 1064 nm heating beam. The optical powers are overestimated as they are measured before several lossy dichroics.

cation. During our most recent chamber bake with the newest chip, we observed a nominal and quite uniform 0.3 nm blueshift of the cavity resonances. This was not consistent with the first chip and bake process, which maintained stable resonances through the bake.

From late 2022 to late 2024, the system was stable. We monitored these slow drifts and occasionally applied LIAD to counteract them and reset the resonances. However, we experienced two sudden, unexplained device failures which prompted us to upgrade and replace the original chip. The first failure occurred while we were not actively monitoring the cavity in question. Upon performing routine measurements, we noticed that the cavity has physically broken off from the chip, though its neighboring devices all remained intact.

The second failure, on the other hand, occurred during active monitoring of the cavity resonance and was characterized by a rapid, irreversible redshift of the resonance. This shift occurred over the course of approximately one day, much faster than the weeks to months long timescale that we had seen from caesium adsorption and pushed the resonance past the atomic resonance. Attempts to reverse this shift with LIAD, resonant driving of the cavity with high probe powers, focused blue laser light, and heating with our 1064 nm laser were all unsuccessful.

Unfortunately, these device failures affected the only two cavities on our original chip that were within thermal tuning range of the atomic resonance. On the bright side, the replacement chip now in use hosts many more cavities within thermal tuning range and is thus much more robust for future experiments. For further detail characterizing the drifts we observed at various stages of the experiment, see Shankar's thesis [120].

3.4 Experiment Control

The control system that drives the experiment is composed of many interconnected hardware and software components. The overarching framework is based upon repeated execution of user-defined sequences of events with the ability to sweep experimental parameters across repetitions to optimize and refine the system performance.

3.4.1 Experiment Control Hardware

The modular Adwin-Pro II system operates as the central "conductor" of our experiments. At its core is the Adwin-Pro-CPU-T12 processor module, which executes programs written in the ADbasic language and interfaces with the system's input and output modules. We utilize the AOut 8/16-B module, which provides eight ± 10 V analog BNC outputs with 16-bit DACs and a 3 μs settling time, as well as the DIO-32 module, which provides 32 digital TTL channels which can be configured as inputs or outputs, though we exclusively operate

in output mode in our setup. Our system contains two of each of the output modules. We additionally incorporate a digital buffer box to prevent voltage drops on the Adwin digital channels by decoupling the load from the Adwin. This buffer box was built in-house and designed by Ahmed Omran. The Adwin system coordinates the outermost layer of timing control in our experimental sequences, providing triggers and analog voltages to control and synchronize various additional hardware in the lab.

Additional control hardware utilized in our experiment includes the Quantum Machines OPX, which drives our AODs for optical tweezer control, rearrangement, and loading atoms onto cavities. The Quantum Instrumentation Control Kit (QICK) is an open source firmware and software stack that enables the use of Xilinx RFSoC (radio frequency system-on-chip) development boards as a control system for quantum experiments. We use this system for our fast optical pulse generation as it has a very high sampling rate of $\sim$6 GHz on its output DACs. We additionally employ several versatile, programmable controllers such as the Moku Go and the QNimble Quarto as needed.

Our setup features a range of auxiliary control hardware for more specific applications such as fast PID controller boxes from Newport, Timebase AOM drivers, as well as a range of home built electronics modules constructed by Roberto Cohen during his time as undergraduate researcher in our lab. We use the Laser Shutter System from Stanford Research Systems for slow but high extinction ratio switching of our lasers. For our single photon time tagging, we use a time tagger system from Swabian.

3.4.2 Experiment Control Software

Our primary interface for programming experiments and analyzing data is a custom Python-based experiment control framework. During his year as a postdoc in our lab, Matteo Pompili led the development of this framework. I had the privilege of collaborating closely with him throughout the process and continuing to build upon it after his departure from

the lab. This brief section does not do justice to this project that forms the backbone of our experimental workflow.

Our framework not only facilitates programming and controlling the experiment, but also supports real-time data visualization, crucial for debugging and monitoring experimental progress. Our data is saved in HDF5 format, accompanied by metadata specifying the sequences and experimental parameters used to generate the dataset. Our standardized analysis and calibration pipeline ensured that processed data and plots are saved alongside the unaltered raw datasets. We utilize a modular sequencing structure to enable additional control hardware to be programmed along with each Adwin sequence as needed.

Our codebase heavily leverages the following open-source repositories:

- **quantify-core**: Underlies our data management and analysis infrastructure
- **xarray**: Enables user-friendly multidimensional data analysis
- **pyqtgraph**: Used for real-time data visualization

We also use the following open-source projects developed by Matteo Pompili:

- **yamlpars**: Provides a straightforward dot notation interface to our experimental parameters
- **easypubsub**: A lightweight interface to publish-subscribe functionality for inter-process communication
- **caniusethat**: A user-friendly interface to remote procedure call (RPC) functionality

Lab conditions such as temperature, humidity, magnetic fields, and laser lock statuses are monitored via a Grafana dashboard, enabling remote monitoring and alerting.

CHAPTER 4

INTEGRATING AN ATOM ARRAY WITH A NANOPHOTONIC CHIP

In the previous chapter, we reviewed the modules that collectively comprise our experimental apparatus. With this foundational understanding of the laser systems, vacuum chamber design, semi-open nanophotonic chip geometry, and experiment control infrastructure, we shift focus in this chapter to discuss the methods used to operate an atom array in close proximity to the nanophotonic chip.

We begin with a brief discussion of a typical framework for our experimental sequences, followed by an explanation of one of the key elements of our system: background-free imaging. We then describe our implementation of atom array rearrangement and provide further details on our optical tweezer control system. These capabilities naturally enable us to load atoms onto the nanophotonic cavities. Lastly, we present data characterizing this loading and conclude with a discussion of the current status of the experiment. The content of this chapter draws heavily from our published results in Ref. [31].

4.1 Experimental Sequences

The most generic experimental sequence for our system proceeds according to the following steps:

1. Load a magneto-optical trap (MOT)
2. Turn off the magnetic field gradient and perform polarization gradient cooling (PGC)
3. Allow the remaining cold atom cloud to disperse while continuing PGC
4. Apply experiment-specific operations (if necessary)

5. Image the atoms

6. Apply experiment-specific operations (if necessary)

7. Image the atoms (if necessary)

8. Ramp all equipment controls back to ambient setpoints

We typically load our MOT in 100-200 ms. During this step our cycler beam is approximately 12 MHz red-detuned of the $6S_{1/2}$ F=4 $\rightarrow$ $6P_{3/2}$ F'=5 transition and our repump beam is approximately 20.5 MHz red-detuned of the $6S_{1/2}$ F=3 $\rightarrow$ $6P_{3/2}$ F'=4 transition. Each of the two diagonal MOT beams delivers 7-8 mW of cycler power and 0.2-0.4 mW of repump power into the chamber with 1 cm beam diameters. The axial MOT beams deliver 1.2-1.3 mW of cycler power and 0.10-0.12 mW of repump power with 1 mm beam diameters after telescope formed with the objective lens. The anti-Helmholtz magnetic field coils are driven to generate an axial magnetic field gradient of $\sim$25 G/cm. By adjusting current through the caesium dispenser, we can trade off between the MOT loading rate and the background-limited lifetime in the chamber. We typically operate the system at a balanced point where the MOT loads in 100 ms and measure background-limited lifetimes of about 14 seconds.

Following the MOT loading, we shut off the current to the gradient coils and sweep the cycler laser frequency to a red-detuning of approximately 45 MHz while simultaneously reducing its power by 80-90% over 10 ms. We additionally adjust the currents applied to the offset magnetic field coils reposition the cold atom cloud with respect to the tweezers. These parameters are optimized by maximizing the observed tweezer loading efficiency. We remain at these PGC parameters and continue to apply the 852 nm light for an additional 50 ms to continue cooling and allow the remaining cold atom cloud to disperse from the array region. At this point, our tweezers have stochastically loaded single atoms with an average occupation across the array of 50-55%.

From here, our experimental sequences branch into many different specific sequences depending upon the goal of the experiment. Broadly speaking, we may apply some additional control operations or proceed directly to imaging the array once the tweezers have been loaded. This initial image of the array provides information used to determine the loading configuration. We then proceed to apply any further experiment specific operations. A second image of the atoms provides information about the atomic survival through the experiment, which is often a proxy for other observables. Finally, we ramp all of our equipment back to ambient setpoint values to keep the system thermalized and maintain stability over time.

4.2 Background-free Imaging

The standard method of readout for atom arrays is fluorescence imaging, where the desired observable is mapped onto to the presence or absence of an atom in each tweezer site. This technique presents a particular challenge for experiments aiming to couple atoms with nanophotonic structures due to the inevitable scattering of the imaging beams from the nearby solid surface, which can be orders of magnitude brighter than the atomic fluorescence signal.

Previous experiments have circumvented this challenge in various ways. Transmission and reflection measurements of the nanophotonic device can be used to readout global system information such as the number of atoms coupled to the structure [25, 28, 129, 130, 131, 132, 93, 133, 134, 91, 22, 21]. The advantage of these methods is that they are much faster than imaging, to such a degree that cavity-based readout is being explored as a general fast readout method for atom arrays [135, 136, 137, 138, 139, 140, 86]. The drawback of these methods is that as the number of atoms coupled to the device scales, they can only provide global system information rather than site-resolved atomic state information. Other approaches including confocal microscopy [91], excitation via propagating waveguide modes [89], careful

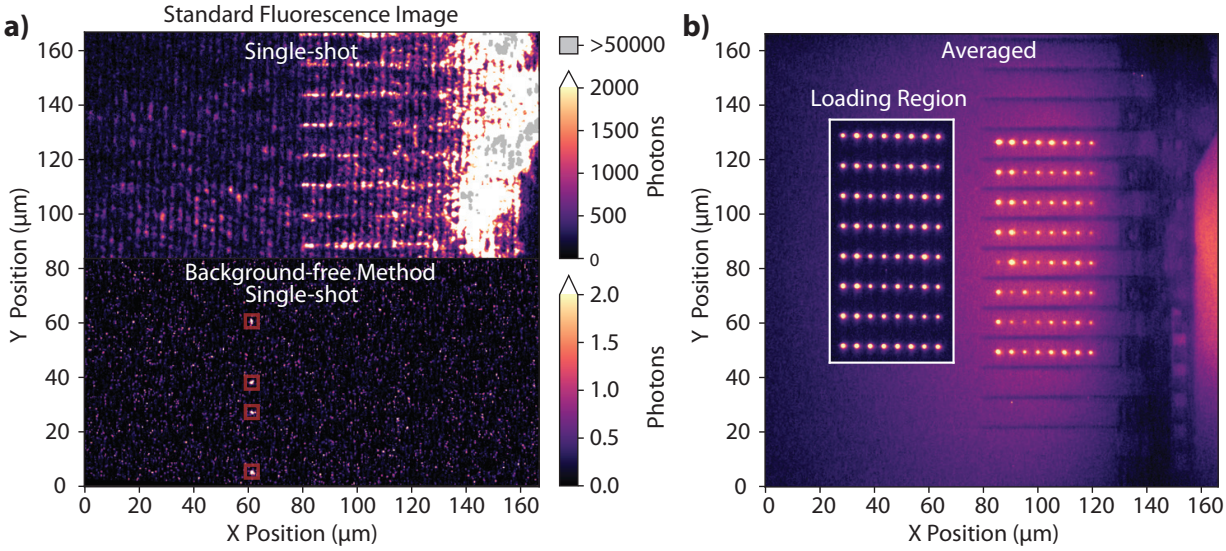

Figure 4.1: **Images illustrating the scattering challenge and the successful implementation of our background-free imaging technique. a**, Top: A single-shot fluorescence image taken using the standard 852 nm (D2) cycling transition near our nanophotonic chip. Despite reducing the electron multiplying gain of our camera by two orders of magnitude compared to the value used to image single atoms, the scattering detected is orders of magnitude brighter than the atomic fluorescence, even of microns away from the devices. Bottom: A single-shot image of atoms (marked by red boxes) taken using our background-free technique. Both images were taken with a 40 ms exposure time. **b**, Averaged fluorescence images of an 8×8 atom array both in the loading region (inset) and interleaved between the photonic crystal cavity array. No post-processing has been applied beyond averaging across the individual images. The devices are visible as shadows due to a small residual background which we attribute to fluorescence at our imaging wavelength from the silicon base layer of the nanophotonic chip. This figure is adapted from our published work, Ref. [31].

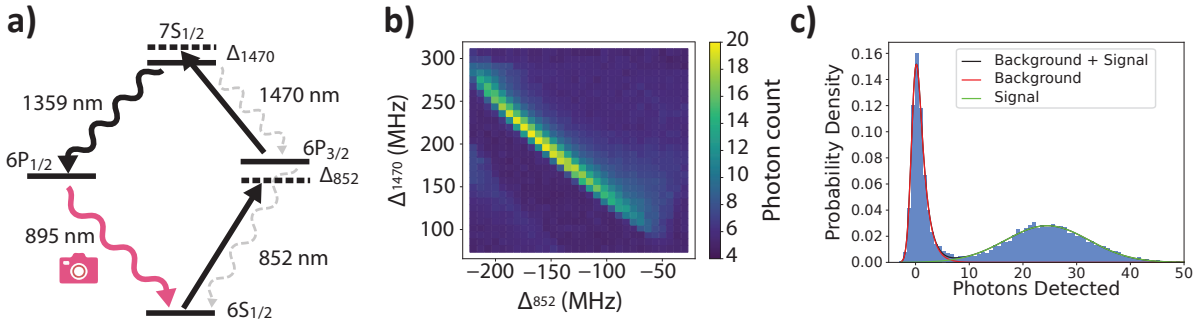

Figure 4.2: **Background-free imaging.** **a**, A caesium fine level structure diagram illustrating the background-free imaging technique. The atoms are doubly excited from the $6S_{1/2}$ ground state along the straight black arrows, through the $6P_{3/2}$ intermediate state. The imaging pathway to the camera is spectrally filtered such that the camera only images photons via the 895 nm decay path from the $6P_{1/2}$ level shown in red. Here, Δ_{852} is the detuning from the bare $6S_{1/2}$ F=4 $\rightarrow$ $6P_{3/2}$ F$'$=5 transition and Δ_{1470} is the detuning from the bare $6P_{3/2}$ F$'$=5 $\rightarrow$ $7S_{1/2}$ F$''$=4 transition. **b**, The average number of detected photons from each atom as a function of the two imaging laser detunings. The signal decays as the 852 nm laser approaches hyperfine resonances on each side of the plot due to resonant heating ejecting the atoms from the tweezers. **c**, A typical histogram of the number of detected 895 nm photons in a 4×4 pixel region of interest over a 40 ms exposure time in the loading region. The bimodal distribution enables us to distinguish between the presence and absence of an atom with a high fidelity $\gtrsim$99.2%. This figure is adapted from our published work, Ref. [31].

background subtraction [89], and combined polarization and spatial filtering [96] have been employed to achieve site-resolved readout. However, these methods are either limited in scalability or rely upon specific system design features which do not generalize. Our goal was to develop a general and scalable method that would enable single-shot, site-resolved readout of an atom array in close proximity to arbitrary nanophotonic devices.

To illustrate the scale of the scattering challenge, we attempted to image our array with the standard D2 line fluorescence imaging technique. In order to protect our electron-multiplying charge coupled device (EMCCD) camera (Nüvü HNü 512) sensor from damage, we reduce its electron multiplying (EM) gain by 2 orders of magnitude from 1000 to 10 for this test. Fig. 4.1 shows that the background due to the scattering is on the order of hundreds to thousands of photons per pixel, even tens of microns away from the cavities, with several pixels on the chip surface detecting over 350,000 photons each. For reference, our typical atomic signal is on the order of $\sim$1.6 photons per pixel across a 4×4 pixel region of interest for a total signal of approximately 25 photons per atom. At the higher EM gain settings used to image single atoms, background light this bright would saturate and potentially damage the camera sensor.

We developed a multichromatic, background-free imaging technique to suppress the effect of this scattering from our nanophotonic chip, enabling single-shot readout of our atom array close to our photonic crystal cavities [31]. This method works by driving a two-photon transition to the $7S_{1/2}$ state via the $6P_{3/2}$ intermediate state using our 852 nm MOT beams and an additional 1470 nm unidirectional imaging beam that co-propagates along one of the diagonal MOT beam paths. The $7S_{1/2}$ state has two branching decay pathways via the $6P_{1/2}$ and $6P_{3/2}$ intermediate states, since the direct $7S_{1/2}$ to $6S_{1/2}$ transition is forbidden. We spectrally filter out the excitation wavelengths on our imaging pathway using several bandpass filters (Semrock FF01-900/11-25) allowing only the atomic fluorescence at 895 nm via the $6P_{1/2}$ decay channel to be detected on the camera. This effectively filters out all of the

undesirable scattering background, recovering the ability to perform high fidelity, single-shot readout of our array near the noise floor of our camera. Fig. 4.1 shows a direct comparison of a single-shot image using this method next to the standard D2 line fluorescence test image described above.

Although similar techniques have been employed in microscopy of biological samples [112], for imaging atomic ensembles [141, 142, 143, 144, 145], and to image ions [146], it was not clear that this method would be effective for imaging single atoms in optical tweezers. Optical tweezer traps are much weaker than ion traps and this method causes additional heating with respect to standard fluorescence imaging since more photons must be scattered per photon detected. This increase in scattering arises from both the two photon excitation required per potentially detected photon and the branching ratio of the $7S_{1/2}$ state, which decays approximately 65% of the time towards the $6P_{3/2}$ state and approximately 35% of the time towards the $6P_{1/2}$ state. Fortunately, these effects are not limiting and we are able to achieve $\sim$99.2% imaging fidelity in our loading region a few tens of microns away from our cavities. This number is calculated from the overlap of the signal and background fits to the bimodal histogram of our atomic fluorescence as shown in Fig. 4.2. Averaged fluorescence images of our array in the loading region as well as interleaved between our nanophotonic cavity array can be found in Fig. 4.1.

Fig. 4.2 depicts the magnitude of the atomic fluorescence signal as a function of the two imaging laser detunings. The 852 nm laser detuning along the x-axis is measured with respect to the bare $6S_{1/2}$ F=4 to $6P_{3/2}$ F'=5 hyperfine transition. The 1470 nm laser detuning along the y-axis is measured with respect to the bare $6P_{3/2}$ F'=5 to $7S_{1/2}$ F"=4 hyperfine transition. The magnitude of the detected signal exhibits an optimal point when the 852 nm laser is in between the $6S_{1/2}$ F=4 to $6P_{3/2}$ F'=5 (0 MHz on the x-axis of the plot) and the $6S_{1/2}$ F=4 to $6P_{3/2}$ F'=4 (-251 MHz on the x-axis of the plot) transitions. The detected signal decays as the 852 nm laser approaches either of these resonances. We

attribute this to atom loss form the tweezer due to resonant heating. As this laser approaches a resonance, the atom is more likely to cycle between the ground state and the first excited state, heating the atom without generating the 895 nm photons needed for our imaging. When the laser is off-resonant from both of these transitions, the two-photon excitation can become the dominant process leading to improved signal and reduced heating of the atoms. The overall feature in the plot tracks the two photon resonance, though it is blue-shifted from the bare two photon resonance by tens of MHz due to the AC Stark shift from the tweezer, which stretches the two photon transition as the ground state is trapped while the doubly excited state is slightly anti-trapped.

4.3 Rearrangement

With the ability to image atoms established, we can begin to rearrange them into defect-free configurations. This is a necessary capability due to the stochastic loading process not only for free space atom array operations but also to load atoms deterministically onto our nanophotonic cavities. To begin rearranging, the stochastic initial loading pattern must be identified via an initial image of the array. Then the atoms must be moved into their target locations. Finally, we can verify whether this process was successful with a second image. Currently, we are limited to one-dimensional rearrangement in our experiment, as we have yet to incorporate a second set of optical tweezers via a spatial light modulator (SLM) to facilitate 2D rearrangement protocols. However, we retain the ability to translate the entire array to facilitate simultaneous loading onto our photonic crystal cavities.

A plot of our rearrangement data can be found in Fig. 4.3. In these experiments, we were most limited by atomic loss from the tweezers. This can be broken down into two separate effects, the first of which is 10-15% loss during the first image. Several pathways to improving this metric include stroboscopic imaging, Raman sideband cooling to the motional ground state before imaging to improve survival, and reworking the 1470 nm imaging beam path.

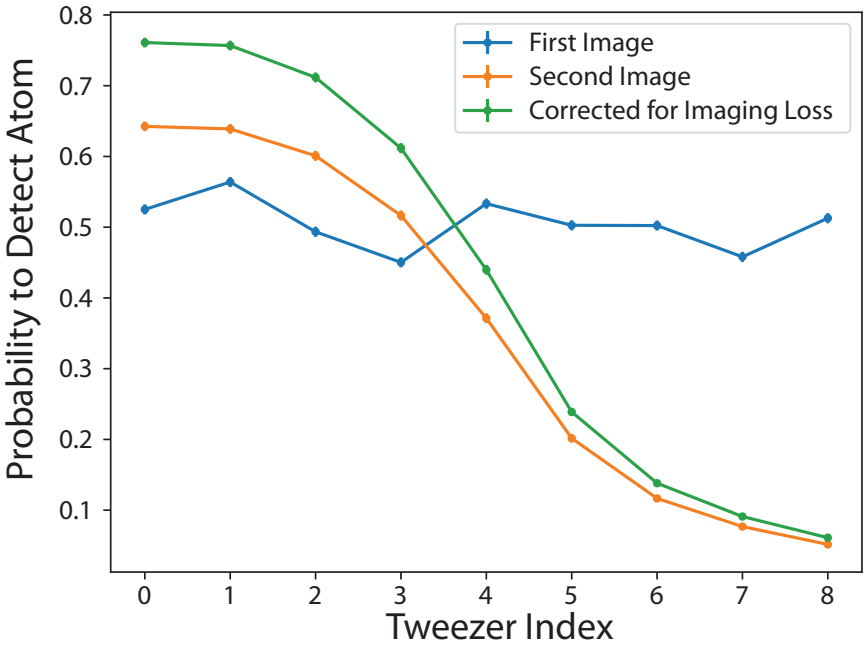

Figure 4.3: **One dimensional rearrangement of the atom array.** Stochastically loaded atoms (blue) are imaged and rearranged to fill the gaps in the stochastic loading pattern (orange). Atom loss of 10-15% during the first image reduces the post-rearrangement atom detection probability. The green line corrects the rearrangement curve for the imaging losses. This figure is adapted from our published work, Ref. [31].

Currently, this beam is unidirectional. Modifying the layout to counterpropagate this beam along all MOT axes will balance out the scattering and should reduce the heating rate. After correcting our rearrangement curve for this loss, we can see that there is another 23% loss that occurs during our rearrangement. This can be improved with improved characterization and optimization of our tweezer intensities during motion as well as improving our frequency chirp profiles. We currently chirp the AOD frequencies according to a symmetric, piecewise quadratic profile, though a minimum jerk profile is likely to improve our atomic retention during motion.

4.3.1 Optical Tweezer Control System

We generate our optical tweezers by driving a pair of crossed acousto-optic deflectors (AODs). The RF drive for each AOD is sourced from a Quantum Machines OPX, which is amplified by high power RF amplifiers from Minicircuits. We generally operate the OPX in one of two modes, which I will designate AWG Mode and Oscillator Mode. In AWG Mode, we program the OPX very similarly to an arbitrary waveform generator, providing the OPX with precalculated waveform samples for it to output. We generally use this mode to generate large, static arrays for system characterization tests. In Oscillator Mode, we take advantage of the OPX's real-time parametric waveform generation, which we primarily use for rearrangement, real-time control of our optical tweezers, and loading atoms onto our nanophotonic cavities. We occasionally operate in a hybrid mode where one AOD is driven statically in AWG Mode while the other is driven in Oscillator Mode. This hybrid modality allows us to perform unidirectional translations of larger arrays without reaching the limit on the number of oscillators supported by our first-generation OPX.

Fast Image Processing and Feedback

For applications such as rearrangement or loading atoms to cavities, we need to act mid-sequence upon the information contained in the initial image which tells us the stochastic loading pattern of the tweezer array. Processing this image on the computer and relaying the tweezer occupation matrix back to the OPX would be prohibitively slow. In order to address this potential cause for latency in the experiment, we utilize a module produced by Quantum Machines called the Observe module. The Observe module eavesdrops on the CameraLink communication line between our EMCCD and our computer and rapidly processes each image into a tweezer occupation matrix based upon pre-calibrated region of interest and threshold information. This processed tweezer occupation matrix is then communicated to the OPX via a fast analog input channel. Once the OPX has received this information, it

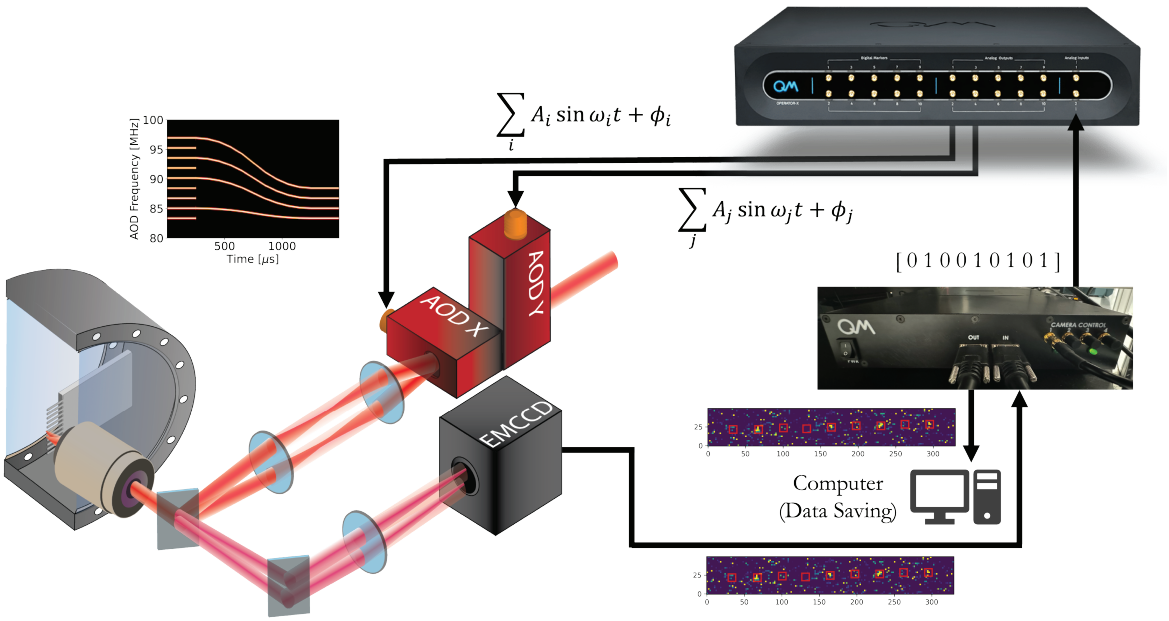

Figure 4.4: **Schematic illustrating our optical tweezer control system.** The Quantum Machines OPX in the top right generates the multisine RF tones that drive the AODs. The atomic fluorescence is imaged with our EMCCD. The data is relayed over a CamerLink connection to the Quantum Machines Observe module, which rapidly processes the image into a binary occupation matrix and relays this information to one of the OPX's analog input channels. The OPX drops tones corresponding to the unfilled tweezers and sweeps the remaining tweezer frequencies to compress the array as shown in the spectrogram in the top left. Part of this figure is adapted from our published work, Ref. [31].

calculates which moves need to be made and execute the rearrangement of the array into a defect-free configuration.

Optical Tweezer Optimization

The relative phases of the multisine tones used to drive the AODs are quite important for at least two reasons. The first is related to the crest factor, or the ratio of the peak to the root-mean-square value of the multisine tone. Since the control system has a maximum output voltage, the generated waveform must be scaled such that the peak of the waveform corresponds to the peak output possible from the system, otherwise the tone will be clipped and undesired frequency components will be introduced. If the tone has a large crest factor, then the bulk of the waveform will be scaled down drastically and may introduce noise and distortions due to the finite bit depth of the system. From this perspective there are optimal sets of phases for the sines that make up the AOD drive tone which result in a mimimal crest factor.

Intermodulation effects, whereby amplifier nonlinearities as well as acoustic nonlinearities in the AODs lead to the generation of sum and difference tones, are also phase dependent. The second and third order tones generated via this mechanism can lead to interference between the tweezer traps, causing crosstalk between the trap amplitudes and inhomogeneity across the tweezer array [147].

In order to address these challenges, we seed random phases for our optical tweezers, then run them through a crest factor minimization algorithm similar to the one presented in Ref. [148]. We then test whether the optimized phases exhibit strong intermodulation effects, and repeat this protocol until we find a set of phases that have a minimal crest factor and do not suffer from intermodulation.

We homogenize our tweezer arrays based upon measurements of the atoms, feeding back on either the atom-by-atom trap frequencies or the atom-by-atom optimal 1470 nm laser

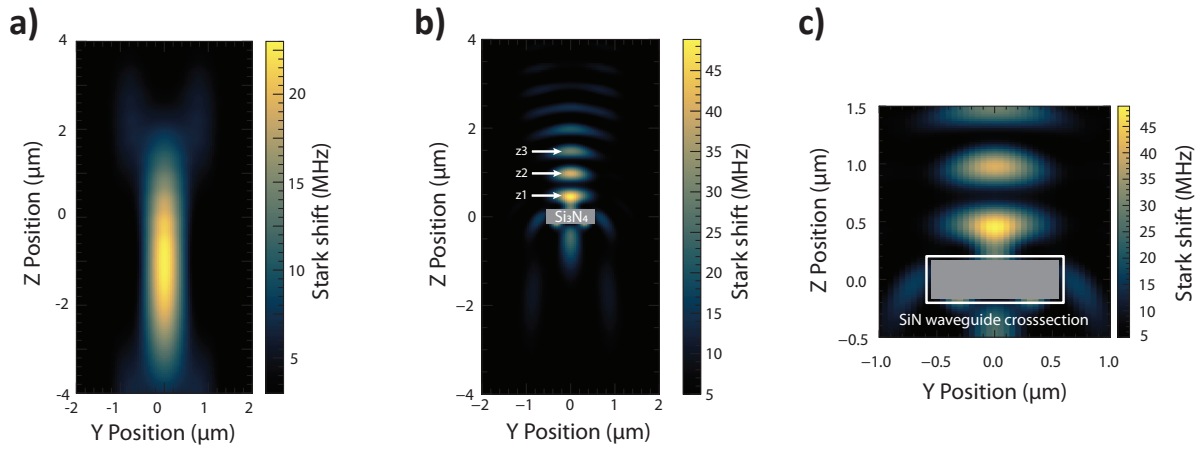

Figure 4.5: **Atom trapping potentials as measured by the AC Stark shift induced on the D1 line transition. a**, A plane slice of the AC Stark shift induced on the 895 nm D1 line transition by a 2.4 mW, 935 nm optical tweezer with a 1.1 μm beam waist. **b**, The modified standing wave trapping potential and D1 line AC Stark shift due to the partial retroreflection of the same tweezer as in **a** from the silicon nitride nanophotonic cavity at the origin. **c**, A zoomed in view of **b**. This figure is adapted from our published work, Ref. [31].

frequency for our imaging. Both of these metrics depend directly upon the AC Stark shift from the optical tweezer, making them good proxy measurements for the optical tweezer intensities. We routinely achieve less than 3% variation across the array.

4.4 Loading Atoms onto Cavities

Now that we have demonstrated the ability to cool, trap, image, and rearrange atoms in optical tweezers close to our nanophotonic cavities, the next step towards atom-nanophotonic coupling is to bring the atoms close enough to the cavities that they can couple to the cavity modes. Since the atoms will couple to the evanescent mode, which is exponentially decaying with increasing distance from the cavity surface, they must be trapped within a few hundred nanometers of the cavity surface in order to interact strongly with the cavity mode.

We employ a side loading procedure as has been previously demonstrated in Ref. [21]. We translate a one dimensional atom array which is already spaced by 11 μm to match the

cavity spacing in between the cavity array, then we translate it laterally until the tweezers aim directly at the cavities. As the tweezer approaches the cavity, the trapping potential distorts from the free space tweezer potential to a standing wave trapping potential above the cavity caused by the partial reflection of the tweezer from the cavity. We currently do this adiabatically, performing each of these moves over the course of 1 ms. However, in practice this approach should be optimized for loading to each specific cavity.

Our cavity geometry does not support an adiabatic, continuous trapping potential during loading. While the tweezer is aimed at the edge of the cavity such that only part of the beam reflects from the cavity, the tweezer potential distorts in a way that does not stably trap the atom. Due to this, we observe ∼40-60% loss of atoms from the tweezers during this loading process. This is measured by loading the atoms onto the devices, holding the tweezer there for a short time of 1 ms, and then moving the atoms back to the loading region to take a high fidelity image of the survival. If we perform the same measurement, but only translate the atoms between the devices rather than loading atoms into the standing wave traps, we observe negligible losses, indicating that the majority of these losses are due to the side-loading procedure.

We believe that our loading process can be further optimized by varying the speed, angle, and AOD frequency chirp profile to encourage the atom to jump across this distorted potential more reliably. Alternatively, redesigning our cavities with a different thickness can enable stable, adiabatic loading with near perfect success probability [120, 21, 94].

4.4.1 Autofocus Protocol for Objective Z Positioning

The probability that an atom in free space successfully loads into the standing wave traps as we translate the tweezer onto the cavity, as well as which of the standing wave intensity maxima it loads into, depends strongly upon the distance between the focal plane of the tweezers and the plane of the cavities. Ideally, the tweezer should be focused a bit below

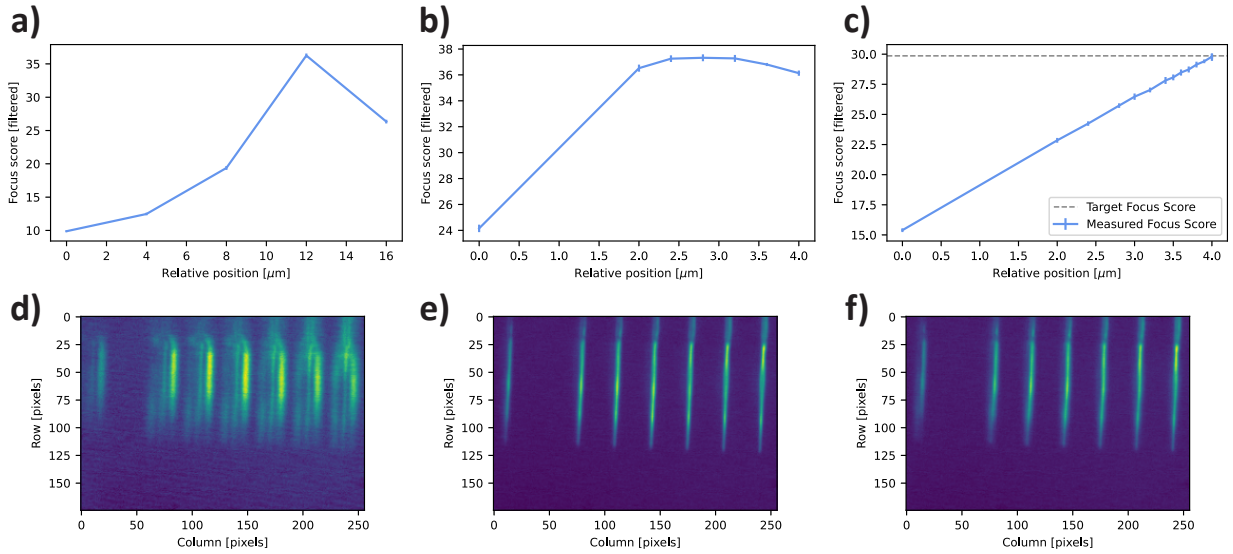

Figure 4.6: **Auto focus procedure.** **a**, The initial coarse scan, used to identify the rough position of the focus plane. **b**, The secondary fine scan, used to identify the maximum focus score to counteract long term drift. **c**, The final optimization scan, demonstrating the decreasing step size as the target position is approached. **d**, The initial blurry image taken at the first position of the coarse scan in **a**. **e**, The image at the position of maximum focus score from the fine scan in **b**. **f**, The final image taken at the target position in **c**, corresponding to 80% of the maximum score from the fine scan in **b**. For a high resolution scan across the entire focus feature, see Shankar's thesis [120].

the cavities in order to maximum the probability of successfully loading the atom into the closest standing wave trap where it couples most strongly to the cavity mode. We have developed the following autofocusing procedure to reliably calibrate and set the Z position of the tweezer input objective with respect to the plane of the cavities.

We image the cavities onto our EMCCD camera using the same imaging pathway that we use to image our atoms. We set the EM gain on the camera to its minimum value and translate a 900 nm LED into our optical tweezer path on a dual position optics mount translation stage (Thorlabs ELL6K) to illuminate the chip at our imaging wavelength. The LED is driven with a constant current supply (Wavelength Electronics LDD200P) to maximize the stability of its brightness. We adjust the objective lens position along the tweezer axis using a Thorlabs PIA13 piezo-actuated screw controlled by a Thorlabs KIM101 piezo controller.

The autofocus protocol proceeds via the following steps:

1. Retract the objective, moving it away from the chamber.
2. Perform a coarse scan of the objective position towards the chamber to locate the rough position at which the cavities are focused.
3. Retract the objective just behind the focus to perform a second fine scan to accurately calibrate the maximum focal score. The purpose of this step is to counteract any long term drift related to the LED brightness or positioning.
4. Retract the objective and scan it forward, reducing the step size as the target position is approached.
5. Stop when the focal score is within one standard deviation of the target position. Perform another imaging check to ensure that the focal score is again within one standard deviation of the target position. If this check succeeds, the procedure is complete. If this check fails, continue moving the objective.
6. If we have passed the target position, return to step 4.

This multiscan procedure is necessary as our piezo-actuated stage is open-loop and exhibits nonuniform step sizes and hysteresis. Therefore, we cannot simply perform one fine scan and immediately translate the objective to the target position reliably. The scans are performed by translating the objective and capturing ten images at each position. A focus score is calculated for each image by first applying a bilateral filter to reduce the noise while preserving the edges, calculating the Laplacian of the image, and finally taking the variance of the Laplacian. This variance is a great proxy for the focus as it is large when edges in the image are sharp, and it is small when edges in the images are blurred. We then take the average the variances of the Laplacians across the ten images as our focal score and calculate the standard deviation across the ten images. We specify the target position as

a fraction relative to the maximum focal score identified in the fine scan and additionally specify which side of the focus should be targeted. As the objective position is translated, the focal scores are calculated in real time, while the slope of the changing focal score and its magnitude with respect to the maximum are used to keep track of whether the objective is focused above or below the cavity plane.

The images used for the focal score are restricted to a small region of interest on the cavities themselves, not including the base of the chip, as we found that this generated a sharper focal score feature and thus improved our targeting precision. Lastly, due to a small angle that existed between the objective tweezer plane and the plane of the cavities, we could shift the position of the peak by selecting a subset of the cavities to use for the focal score calculation. This enabled us to speed up the autofocusing protocol by targeting a position on the positive slope of the focal score peak, even though we actually focused a bit behind the devices of interest.

Thermal Stability

The stability of the objective position along the axial direction is extremely important in order to keep our cavity loading characteristics consistent during data collection. We can always reoptimize the position by re-initiating our autofocus procedure, but it is crucial to properly understand the timescale over which this becomes necessary. Initially, we experienced inconsistent results and uncontrolled drifts occurring over the course of the day in lab. We tracked this down to a single primary contributor: our MOT gradient coils. These coils are very close to our objectives and are only driven during the MOT loading time. We found that as we ran different experimental sequences, with varying MOT on/off duty cycles, this would lead to notable drift of our tweezer objective with respect to the cavities.

We addressed this by calibrating an ambient intermediate current setpoint that mimics the heat output from operating our experiment and drive the magnetic field coils at this

setpoint when the experiment is not running. We then fixed our experimental sequences to ensure a constant duty cycle of the MOT coils, by either extending the MOT loading time or padding each repetition with additional waiting time as needed to maintain this constant MOT on/off ratio. After implementing this procedure, we found that we could operate for more than several days at a time without needing to adjust the focus, though we continued to re-focus at least daily as the procedure is automated and takes only a couple of minutes to run. This time is mostly limited by the stage movement time itself.

4.4.2 XY Positioning

In order to load atoms onto our nanobeam cavities, we must reliably translate our optical tweezers from their loading positions in free space to aim directly at the cavities. The precision required is on the order of hundreds of nanometers or better as the cavities are only 1.1 μm wide, which is comparable to the diffraction limited spot size of our tweezers. In order to automate the alignment of the tweezers to the cavities for loading, we take images of both the cavities and a spaced out array of atoms. These two images allow us to calculate mappings between the AOD drive frequencies, the pixel array of the camera sensor, and the cavity positions in real space. This procedure operates following these steps:

1. Calculate an affine mapping between the AOD RF frequency space and the EMCCD camera pixel space by uploading a known array of tones and averaging hundreds of atom images to determine the atomic positions on the camera sensor.

2. Take image of the cavities on the EMCCD by illuminating them with a 900 nm LED.

3. Rotate the device image to correct for the angle between the camera sensor and the nanophotonic chip.

4. Collapse the image vertically and convolve this one dimensional image with a step function. The first peak of the convolution marks the base edge of the cavities.

5. Take a column slice of the rotated cavity image along the centers of the cavity modes, a known horizontal distance away from the base edge of the cavities.

6. Identify peaks in this column slice and fit them to Lorentzians in order to extract the cavity center positions in camera pixel space.

7. Undo the image rotation and the affine mapping to retrieve the target positions in AOD RF frequency space with sub-pixel, $\lesssim$337.4 nm) precision.

This procedure can also be used along with the known 11 μm spacing between the devices to independently calibrate the imaging system magnification by enabling a comparison between the real space distance between cavities and the camera pixel distance between cavities. These steps are illustrated in Fig. 4.7.

4.4.3 Background-free Imaging on Cavities

We additionally investigated our ability to image the atoms while they are loaded directly on top of our nanophotonic crystal cavities. This is particularly challenging as the lifetime of the atoms is significantly reduced while they are loaded into the standing wave traps formed by the reflected optical tweezer potential above the cavities. A detailed theoretical investigation into the observed increased heating rates for nanofiber traps in the evanescent field of two-color (one red-detuned attractive potential combined with one blue-detuned repulsive potential) guided modes can be found in Ref. [149]. This work found that the primary cause of the heating is optomechanical coupling between the atom and the flexural mechanical modes of the waveguide structure. Similarly reduced lifetimes have also been observed in other experiments using the type of reflected optical tweezer traps that we employ [21, 24, 91]. Fig. 4.8 shows a comparison of our measured atomic lifetimes both in free space and when loaded into the standing wave traps above the cavities.

Despite this additional challenge, we have demonstrated the ability to image our atoms

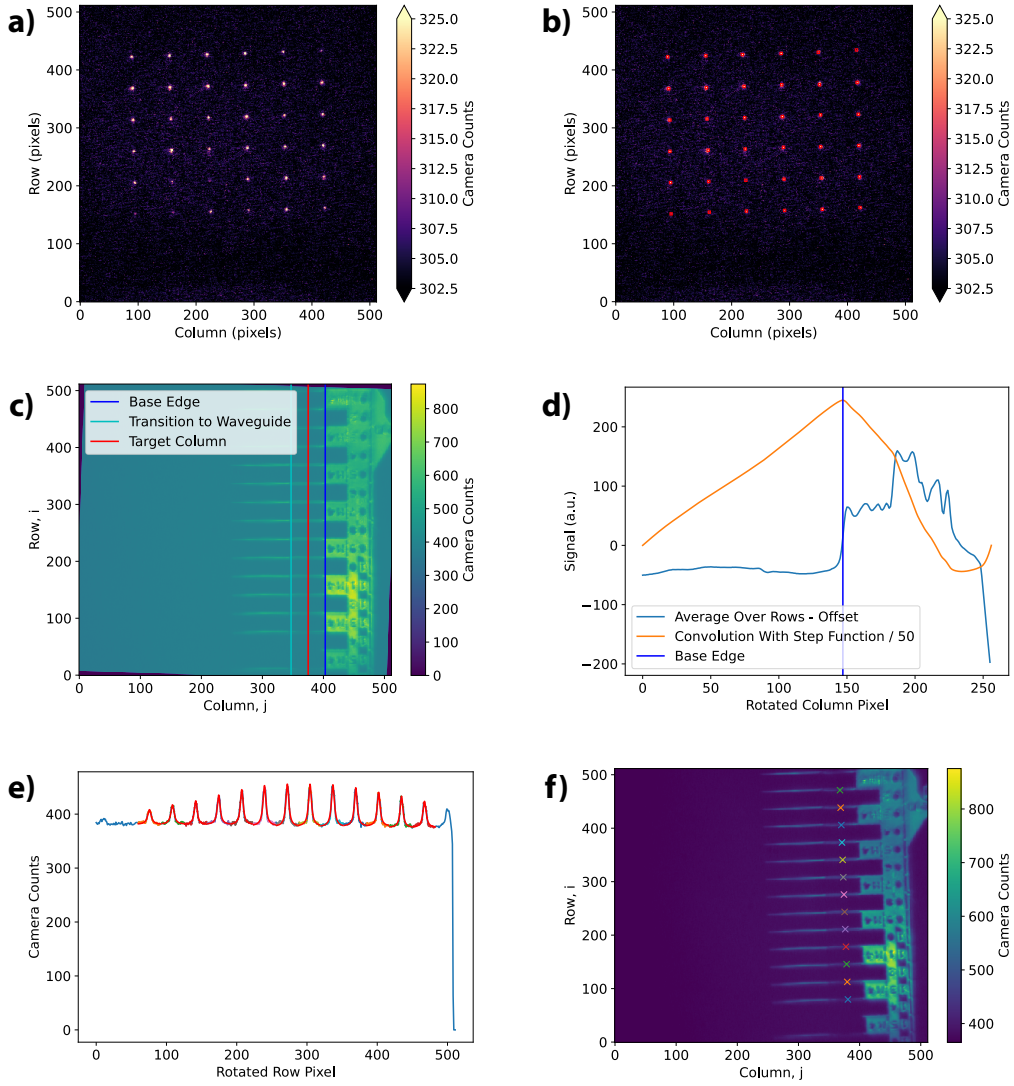

Figure 4.7: **XY calibration procedure to determine target positions on the cavities to load the atoms.** **a**, An averaged image of the atomic fluorescence from a large, spaced out tweezer array. **b**, The automatically identified atomic positions boxed in red. **c**, A rotated image of the cavities labeled with the base edge of the devices, the target column slice along the centers of the cavity modes, and the transition from the cavities to the tapered waveguides. **d**, The row-averaged one dimensional image of the cavities. Its convolution with a step function is plotted as well (scaled down by a factor of 50 for visualization purposes). The peak of the convolution is used to identify the base edge of the cavities. **e**, Lorentzian fits (red) to the one dimensional column slice along the red target column line in **c** (blue). **f**, The target positions for each cavity marked on the un-rotated device image. Note that the images of the devices in **c** and **f** have been rotated by ∼90 degrees counter-clockwise with respect to the images of the atoms in **a** and **b**. The cavities, while not visible, are positioned at the bottom edge of the images depicted in **a** and **b**.

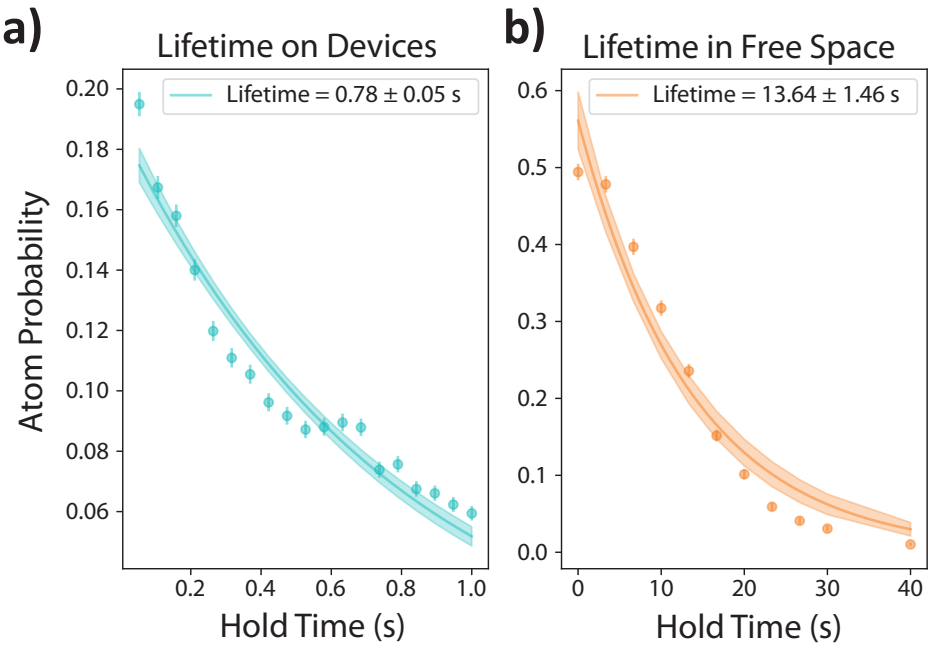

Figure 4.8: **Atom lifetimes. a**, The lifetime of the atoms in the reflected optical tweezer standing wave traps on top of the photonic crystal cavities. **b**, The atomic lifetime in free space optical tweezers. This figure is adapted from our published work, Ref. [31].

in these traps using our background-free imaging method. However, the imaging fidelity is reduced compared to imaging in free space. This reduction in fidelity is primarily due the additional heating and increased atomic loss rate. More often in this case, the atoms are ejected from their traps before enough photons have been detected on the camera to reliably detect their presence. We anticipate that implementing Raman sideband cooling will improve the imaging on cavity performance. Currently, we measure typical atomic temperatures of approximately 50 μK after loading into the tweezers as calculated from a Monte Carlo fit to a standard drop and recapture experiment shown in Fig. 4.9. Nonetheless, this capability has proved to be a powerful diagnostic tool in our experiments.

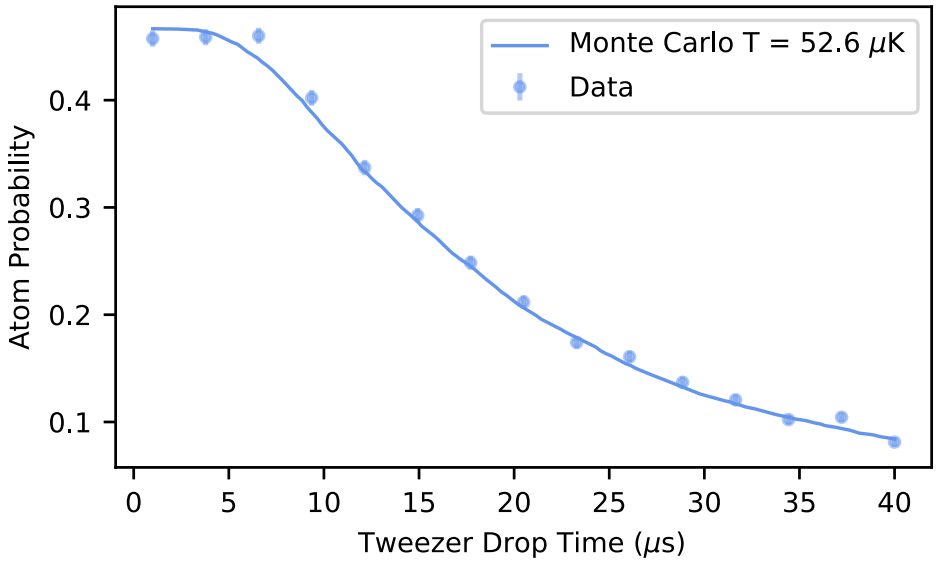

Figure 4.9: **Drop and recapture measurement of the atomic temperatures.** The temperature is calculated by fitting a Monte Carlo simulation to the recapture probability as a function of the tweezer drop time.

4.5 AC Stark Shift Measurements in Standing Wave Traps

When we first set out to demonstrate that we were loading into these standing wave traps, we had not yet built the cavity frequency stabilization system necessary to lock our cavity resonances to the atomic transition frequency. Without this system, probing the atom-cavity interaction directly is not possible as the cavity is not co-resonant with the atom. Therefore, we needed a different method to ensure that we were indeed loading atoms into the standing wave traps above the cavities. We set out to test this by investigating the tweezer-induced AC Stark shifts experienced by the atoms since the peak intensity of the closest standing wave trap to the cavity is nearly double that of the free space tweezer, see Fig. 4.5. Our optical tweezer wavelength of 935 nm is magic for the $6S_{1/2}$ to $6P_{3/2}$ transition at 852 nm, meaning that the AC Stark shift induced for the $6S_{1/2}$ and $6P_{3/2}$ levels is equal in sign and magnitude. Therefore, this specific transition frequency is insensitive to intensity variations of the optical tweezer and thus cannot be used for this measurement. We instead probe the

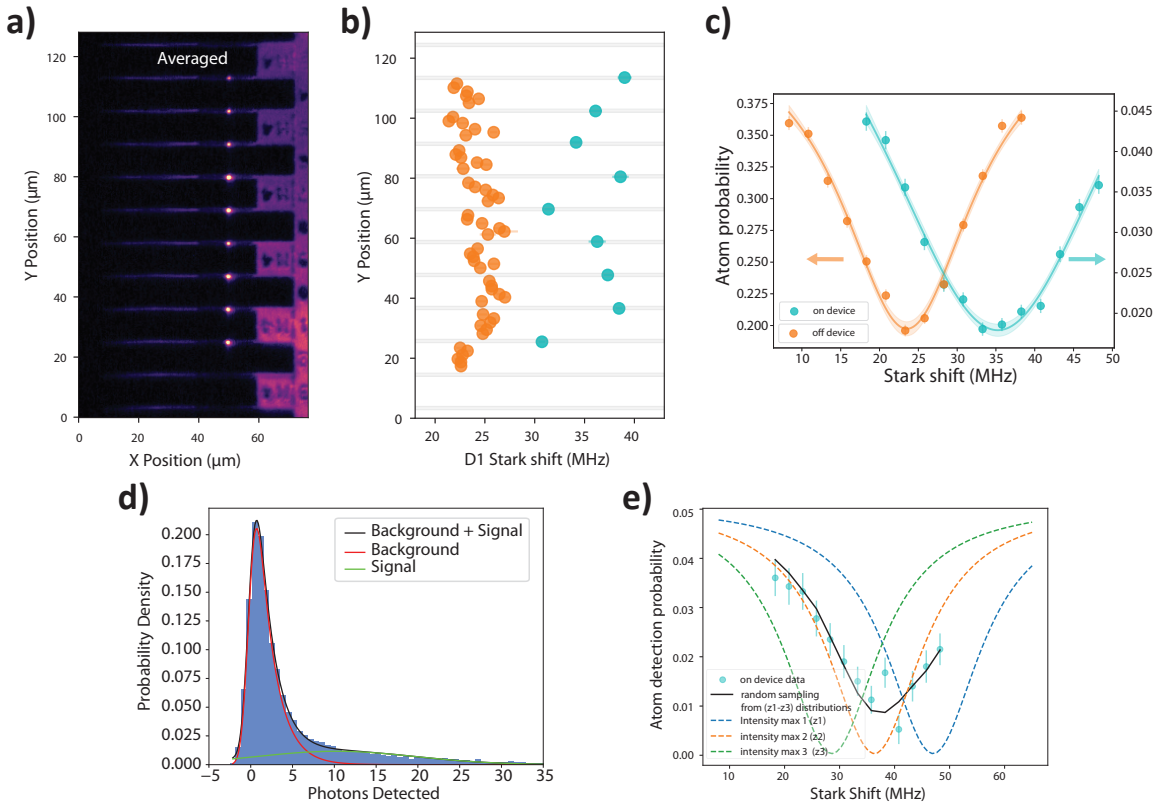

Figure 4.10: **Imaging atoms on top of the cavities and measurements of the modified trapping potential.** **a**, An averaged fluorescence image from 15,000 images of a 1×9 array of atoms loaded onto the nanophotonic cavities, without rearrangement. An image of the cavities is overlaid for illustrative purposes. **b**, The Stark shift induced on the D1 line measured atom-by-atom as a function of position showing that the atoms are indeed loading into the standing wave traps above the cavities. **c**, The orange and cyan points in **b** are extracted from fits to blowout curves such as this one. The D1 blowout pulse laser frequency is varied and most effectively ejects atoms from the traps when it is on resonance with the Stark shifted transition. **d**, A histogram of the atomic fluorescence counts when applying our background-free imaging method to image atoms in the standing wave traps on top of the cavities. Here, we extract an imaging fidelity of 86% using a binarization threshold of 5 photons. **e**, The expected Stark shift survival curves for atoms trapped in each of the closest three intensity maxima of the standing wave traps. We fit the experimental data in cyan to a random sampling from the three dashed curves to extract an estimated loading ratio, considering only the successful loading events, of 29% to the closest intensity maximum, 66% to the second, and 5% to the third. This figure is adapted from our published work, Ref. [31].

AC Stark shift induced on the D1 line transition from the $6S_{1/2}$ state to the $6P_{1/2}$ state at 895 nm.

We measure this Stark shift by first loading the tweezers in the loading region, translating these atoms in between the cavity array, and then translating them perpendicular to the cavity axis to load the atoms from the side into the standing wave traps above the cavities. We then apply an 895 nm laser pulse with varying frequency in order to eject the atoms from the traps. This blow out pulse most effectively ejects the atoms when the laser is resonant with the Stark-shifted atomic transition. Finally, we image the atoms to detect the atomic survival rate. In Fig. 4.10, we plot survival curves averaged across a 1×9 array for both free space tweezer traps as well as standing wave traps on the cavities. We extract the centers of the survival curves as determined by fits for each individual atom as a function of the final tweezer position where the 895 nm pulse was applied in Fig. 4.10. This data shows that the observed increase in the Stark shift only occurs when the atoms are directly on top of the devices in the standing wave traps.

We can also note that the large variation across the devices, which we attribute primarily to a small angle which existed between the plane of the chip and the focal plane of the objective. We have taken steps to minimize this angle with the new, replacement chip currently in the chamber. This angle changes the loading distribution across the standing wave intensity maxima. We performed Monte Carlo simulations sampling from the AC Stark shifts expected for atoms loaded into each of the first few intensity maxima of the standing wave potential. This model indicates that out of the $\sim$40-60% of atoms that successfully jump the potential barrier into the standing wave traps, up to 29% make it into the desired, closest trapping region, 66% make it into the second closest trapping region, and 5% make it into the third closest trapping region. The loading process was optimized using the array averaged data and should be readily improvable by optimizing with respect to loading to a specific cavity.

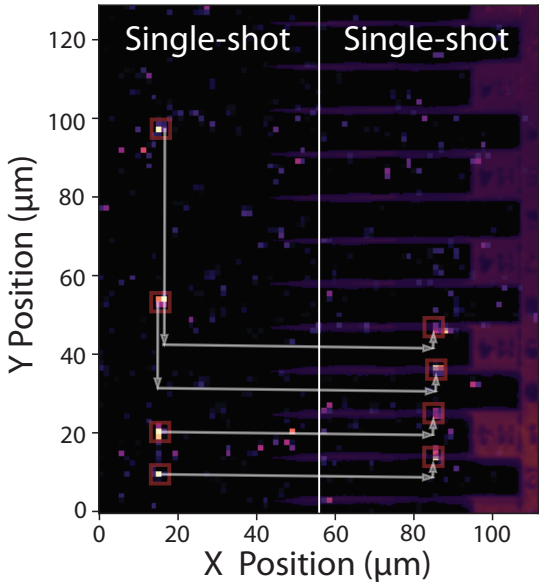

Figure 4.11: **Atomic trajectories used to perform rearrangement and defect-free loading to the cavity array.** This figure is adapted from our published work, Ref. [31].

4.6 Defect-free Loading to Cavities

Finally, we can combine the capabilities demonstrated in this chapter and demonstrate the ability to load defect-free arrays of atoms onto the nanophotonic cavities. This capability is a critical milestone on the path to realizing controlled, scalable atom-photon interfaces on a chip. We begin by loading our optical tweezer array stochastically and performing one dimensional rearrangement into a defect-free configuration. Then we translate the defect-free array laterally between the devices and then side load these atoms onto the nanophotonic cavities following the example trajectory marked in Fig. 4.11. Finally, we image the atoms on the devices to verify success. This experiment is performed in two ways: loading each atom onto its own cavity or loading the small array onto a single cavity.

A schematic representation of the experimental sequence, averaged images of the atoms loaded onto the cavities following this procedure, and examples of our best single-shot successes are shown in Fig. 4.12. The success rate of this overall procedure is limited due to

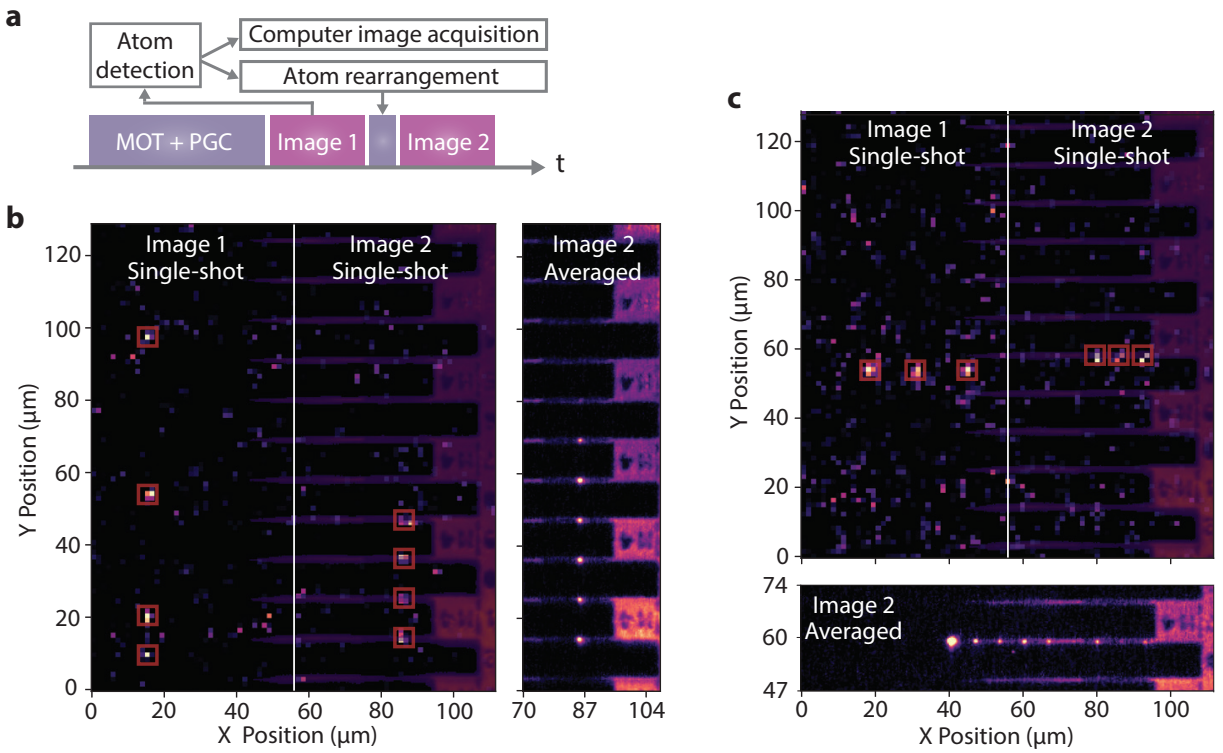

Figure 4.12: **Rearrangement and examples of defect-free loading onto devices. a**, The experimental sequence used to perform these experiments. After loading the tweezers, Image 1 detects the stochastic loading pattern which is used to rearrange the array before it is translated over and onto the devices, where we take Image 2. **b**, Single-shot images of our best example, loading a defect-free array of four initially loaded atoms successfully onto four neighboring cavities. The averaged image of many attempts is shown on the right. A reduced 25 ms exposure time was used to increase the atomic survival rate through the first image for every image in this figure. **c**, Same as **b**, but instead of loading each atom to its own cavity, we load them simultaneously onto the same cavity. This figure is adapted from our published work, Ref. [31].

atomic loss during the first image, which is mitigated by decreasing the exposure time of this initial image to 25 ms, as well as the losses experienced during rearrangement and side loading onto the cavities. Nonetheless, we were able to successfully load rearranged, defect-free arrays of up to four atoms to a set of neighboring cavities, one atom per cavity, and three atoms onto a single device. These results lay a strong foundation for future experiments coupling atoms to our nanophotonic devices.

4.7 Current Status

Following the publication of our initial results last year, both of the near-resonant cavities on our original chip broke, prompting Shankar to return to the cleanroom to fabricate a new and improved chip. The updated chip design hosts significantly more cavities whose resonances lie within our thermal tuning range of 1-2 nm red-detuned from the atomic resonance. The new chip has been successfully mounted into our vacuum chamber where it will serve as the foundation for our next round of experiments. Further details regarding the new chip can be found in Shankar's thesis [120].

Meanwhile, we continued to develop and refine our experimental capabilities to prepare for future experiments probing atom-cavity coupling. This involved improving and testing our cavity frequency stabilization setup as well as incorporating our single photon detectors and time tagger into our experimental sequences and data analysis infrastructure. Our fast pulse generation setup, used in the telecom-photon entanglement protocol and described in the next chapter, was also upgraded with an automated minimization of the EOM's DC bias to improve the extinction ratio of the pulses.

Much of the effort in the lab since the start of 2025 has been focused on rebaking, rebuilding, and realigning the system following the chip replacement. These efforts have also provided an opportunity to transfer knowledge about the setup to the next set of graduate students. Preparations are currently underway to move the entire experiment to Innsbruck, where the next generation of experiments will continue.

CHAPTER 5

FUTURE DIRECTIONS

With our successful realization of an atom array interfaced with a nanophotonic chip, the foundation has been laid for a wide range of future experiments. In this chapter, we outline two future directions exploring the diverse range of applications of integrated atom-nanophotonic systems. The first is the development of a direct telecom quantum network node, which we have been directly pursuing for some time. The second is the realization of a waveguide QED quantum simulator, based upon theoretical insights and pioneering experimental work from the Kimble group and others [58, 150, 22, 151, 152, 153].

5.1 Telecom Quantum Network Node

The nanophotonic cavities currently fabricated on our chip were designed specifically for quantum networking. They are resonant with a telecom transition between two caesium excited states to facilitate direct entanglement between the atom and a telecom photon. This is desirable to circumvent the commonly implemented frequency conversion step in quantum networking experiments, which tends to be quite lossy. In this section, we explain the protocol and chart a path towards implementing this goal. The core ideas here were first developed by my colleague Shankar G. Menon and presented in Ref. [119].

5.1.1 Probing Atom-Cavity Interactions

Our next major experimental milestone, which we were preparing to implement before the failure of our original cavity chip, is to directly probe the interaction between a single atom and one of our telecom nanophotonic cavities. One straightforward way to probe this interaction is to measure the Purcell enhancement of the decay from the $7S_{1/2}$ state to infer the atom-cavity coupling strength g. This can then be used to calculate the atom-

cavity cooperativity C, a key figure of merit comparing the ratio of coherent atom-cavity interactions to the primary dissipative losses from the cavity and atomic decay.

This measurement is quite similar in spirit to our AC Stark shift measurements described in the last chapter. After loading the atoms onto the cavities, the D1 line ejection pulse would be replaced with a pulse of both 852 nm and 1470 nm light to excite the atom up to the $7S_{1/2}$ state. The atom will then preferentially decay into the coupled cavity mode, which we would collect through our free space coupling pathway, routing the collected photons to our single photon detector via an optical fiber. Constructing a histogram from the time tags following this pulsed excitation would yield a decay curve with a decay timescale faster than the known decay timescale for the $7S_{1/2}$ state, enabling us to extract the atom-cavity coupling strength.

We have already developed the necessary experimental infrastructure to perform this measurement, including the cavity frequency stabilization, fast pulse generation, and single photon detection. The unfortunate failure of our original chip was especially disappointing given how close we were to performing this measurement.

5.1.2 Telecom Single Photon Source

Beyond probing the atom-cavity interaction, this same experiment enables the system to operate as a telecom-band single photon source. An autocorrelation measurement, performed by routing the collected signal through a fiber beamsplitter to two channels of our superconducting nanowire single photon detector (SNSPD), would allow us to verify the single photon nature of the emission by plotting the second order correlation function $g^{(2)}(\tau)$. This photon source could be operated in "rapid-fire" mode, by continuously exciting the atom as it is coupled to the cavity. Alternatively, the pulsed excitation approach described above would enable on-demand generation of single photons.

This measurement will additionally provide us with an improved, faster method of opti-

mizing the proportion of atoms that load into the closest intensity maximum of the standing wave traps above the cavities. The previous AC Stark shift measurements were quite slow and relied on long data collection runs, whereas measurements of the collected telecom photons would provide clear information about the atom-cavity coupling and thus the distance between the atom and the cavity.

5.1.3 Telecom Time-bin Entanglement Protocol

The current version of our nanophotonic chip is specifically designed to explore the possibility of directly entangling the hyperfine ground state of an alkali atom with a time-bin telecom photon. This would lay the groundwork for a scalable quantum network composed of atom array modules capable of operating over long distances spanned by optical fibers. The original idea and proof of concept simulations for this application were developed and presented in Ref. [119]. Additional information and further details on how this fits into a larger picture of quantum networking can be found in Shankar's thesis [120].

The general protocol starts assuming that we have our atom trapped in the closest intensity maximum of the standing wave traps above the cavities and that the cavity resonance is stabilized to match the atomic transition wavelength. We also require Raman hyperfine state manipulation, which is currently being developed in the lab. The idea is to first prepare a superposition of the $6S_{1/2}$ hyperfine ground states, apply an 852 nm laser pulse to excite the portion of the atomic population in the $6S_{1/2}$ F=4 state to the $6P_{3/2}$ F'=5 state, which is then further excited to the $7S_{1/2}$ F=4 state via a continuous 1470 nm beam. From here, the cavity Purcell enhances the decay to the $6P_{1/2}$ F=4 level and we apply a final 895 nm pulse to coherently map this population back to its original $6S_{1/2}$ F=4 ground state.

We follow this "diamond-scheme" pulse protocol with a Raman pulse to flip the hyperfine qubit ground state populations and repeat the diamond-scheme pulse protocol once again. At the end of the second pulse sequence, we will have prepared an entangled state where the

correlation structure exists between the hyperfine ground state of the atomic qubit and the time of emission (or time-bin) of the collected telecom photon. This time-bin entanglement is robust to most optical fiber perturbations and provides a great method of encoding quantum information for long distance entanglement generation and applications in quantum networking. A core advantage of this scheme is that it directly entangles our atomic qubit with a telecom photon with no need for frequency conversion. This atom-telecom photon entangled state can be used to generate long-distance entanglement between two such atom-cavity systems located far apart by measuring out the interfered photons at a beamsplitter between the two quantum network nodes, erasing the which-path information and casting the entanglement to the two atomic qubits.

5.1.4 Fast Optical Pulse Generation

One technical detail required to implement this scheme is that the pulses must be quite fast, on the order of one nanosecond or ideally even shorter. This is due to the short lifetimes of each of the three excited states that we route the atomic population through, which range from 30 ns to 48 ns. Thus, the diamond-scheme pulse sequence must be fast compared to this timescale in order to mitigate atomic decay mid-sequence which would destroy the entangled state before it is prepared.

In order to generate the fast sub-nanosecond-scale pulses necessary for our telecom entanglement protocol, we use an amplitude EOM (iXBlue NIR-MX800-LN-20) in series with a semiconductor optical amplifier (Superlum SOA with an Aerodiode driver). The EOM provides high speed pulse shaping, while the SOA acts as a fast, high extinction ratio switch. We require high extinction ratio to prevent dephasing of the atomic qubit due to small leakage when the pulses are switched "off." The SOA has an extinction ratio of $\sim$50 dB while the EOM has a $\sim$20 dB extinction ratio, which would not be sufficient for our applications. Yuhao Deng performed simulations of the dephasing effect that small leakage would have

during the Raman pulse to flip the hyperfine qubit in between the two diamond-scheme pulse sequences and developed this EOM and SOA solution to increase our extinction ratio to a level that will not appreciably affect our projected entanglement fidelities. We control these two devices with electronic control pulses generated by the QICK (Quantum Instrumentation Control Kit) running on the Xilinx ZCU216 RFSoC board. We amplify the EOM pulse with an iXBlue DR-PL-20-MO pulse amplifier.

5.1.5 Multiplexing

One unique opportunity enabled by our chip architecture is the potential to implement spatial multiplexing across the cavity array. By coupling multiple atoms to distinct cavities, we can significantly increase the overall entanglement generation rate, an important metric for scalable quantum networking.

This relies on our ability to independently frequency stabilize the cavities. Thus a measurement of the degree of thermal crosstalk between nearby cavities is essential to accurately determine the feasibility of this approach. If this crosstalk is limiting, then utilizing non-neighboring cavities spaced further apart would present a short term path forward for proof of principle experiments. Future versions of the chip could incorporate cavity specific heater pads, such as those developed in Ref. [91, 24], to further mitigate this potential challenge.

Additionally, the coupling beam pathway will require some additional engineering to separate out these multiplexed signals. One promising path to accomplish this would be to use a telescope to map the outcoupling edges of the cavities to couple into a linear fiber array. Alternatively, an AOD or SLM could be used to couple these multiple beam paths into a single fiber, particularly if paired with time-multiplexed emission.

5.1.6 Rydberg Prospects

An important open question in the field regarding future efforts to incorporate Rydberg-based two-qubit gates into atom-nanophotonic systems concerns the effect of the nearby dielectric surface on the gate fidelity. To date, only one measurement of two-qubit Rydberg gate fidelity as a function of the distance between the atoms and a nearby dielectric has been reported [92]. This experiment was performed near a single nanophotonic crystal cavity mounted at the end of a tapered optical fiber. The results suggest that the primary detrimental effect was due to stray charges that had accumulated on the insulating optical fiber.

It remains unclear how these effects will generalize to larger chip-based platforms like ours. Optimistically, the grounded metal mounting structure used to secure our chip may provide a better pathway for stray charges dissipation, mitigating the observed fidelity reductions. On the other hand, the substantially larger dielectric surface of the chip may exacerbate the charge noise effects and further reduce measured fidelities.

Future experiments investigating the degree to which the effects can be mitigated with dynamical decoupling or whether continuous LIAD can help dissipate charges in real-time are essential for future experiments aiming to couple atoms to nanophotonic structures.

5.1.7 Utilizing Chip Surface

The current version of our chip does not utilize the majority of the chip's surface, leaving room for significant enhancements of the chip's functionality. Further developments on the chip nanofabrication process could enable on-chip control, photon routing, beamsplitters, and detectors. Alternative geometries coupling light to and from the system via grating couplers on the chip surface could be explored. Two-dimensional nanophotonic structures such as ring resonators [154] or two-dimensional photonic crystals [151, 155] could be incorporated onto the chip surface as well. To facilitate loading atoms further onto the chip surface,

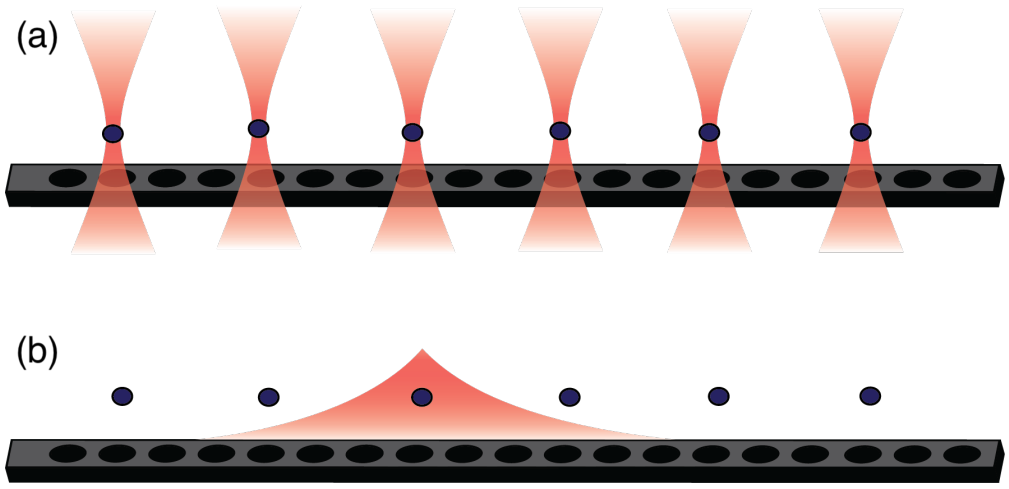

Figure 5.1: **Schematic depictions of atom waveguide coupling a**, An illustration of an array of atoms trapped in reflected optical tweezer traps coupled to a nanophotonic waveguide. **b**, An illustration of the induced cavity mode that mediates atom-atom interactions when the atom is excited and its transmission lies within the photonic bandgap of the photonic crystal waveguide (with the optical tweezers removed for clarity). This excitation can hop to nearby atoms simulating a spin exchange Hamiltonian as discussed in the text.

atoms could be side-loaded from free space onto unpatterened cantilevered "loading tracks" which provide a path for the atoms to follow towards the surface mounted nanophotonic structures. Future extensions such as these represent an exciting path towards scalable atom-nanophotonic systems.

5.2 Waveguide QED Quantum Simulator

Our experiment, incorporating arrays of individually trapped and controlled atoms with a nanophotonic chip, is also particularly well suited to explore exciting directions exploring quantum many body physics and waveguide-mediated interactions, a direction pioneered by Jeff Kimble and colleagues [58, 150, 22, 151, 152, 153, 94]. These ideas represent only a small part of the larger, rapidly growing field of waveguide QED with wide ranging applications [59, 60, 61, 62, 63, 64, 65, 19].

5.2.1 Band Gap Mediated Interactions

One interesting regime of operation for atom waveguide systems aligns the atomic transition close to the band edge, where the group velocity of the propagating modes is slow and there exists a high local density of photonic states due to the van Hove singularity at the band edge. This leads to enhanced, preferential decay into the photonic crystal guided modes and strong atom-field coupling. An enhanced ratio of the decay rate into the waveguide relative to the total decay to all other modes including free space $\Gamma_{1D}/\Gamma' \geq 1$ can readily be achieved and is projected to reach $\Gamma_{1D}/\Gamma' \sim 100$ in the near future with experimental improvements [156]. It is in this regime that phenomena such as collective dissipation and superradiance are being explored in the literature.

An alternative regime with which to explore highly tunable quantum many body physics arises when atoms are coupled to a nanophotonic crystal waveguide such that the atomic transition is situated within the waveguide's photonic band gap. A trapped atom coupled to a waveguide in this regime induces a localized photonic cavity mode centered around the atom with an exponentially decaying profile along the waveguide [157, 158]. This bound photon state can mediate interactions with another nearby trapped atom [159, 160, 161]. A mapping between this system and the interaction Hamiltonian of the Jaynes-Cummings model has been established and shown to agree well with exact numerical calculations based upon the full electromagnetic Green's function [58]. The interaction Hamiltonian describing the effective dipole-dipole spin exchange between atoms trapped along the nanophotonic waveguide takes the following form:

$$\hat{H}_{BG} \approx \frac{\hbar g_{eff}^2}{\delta_{eff}} \sum_{i,j}^{N} \hat{\sigma}_{eg}^{i} \hat{\sigma}_{ge}^{j} e^{-|x_i - x_j|/L} u(x_i) u(x_j) \tag{5.1}$$

Here g_{eff} is the effective coupling of a cavity with mode volume $V_m = A_{eff} L$, where A_{eff} is the effective transverse mode area of the band edge mode of the photonic crystal waveguide

and $L = \sqrt{\alpha\omega_{BE}/k_{BE}\Delta_{BE}}$ is the length scale of the exponentially decaying profile of the bound photon state. We also have the effective detuning $\delta_{eff} = 2\Delta_{BE} = 2(\omega_a - \omega_{BE})$ which is twice the detuning between the atomic transition and the band edge frequency Δ_{BE}. The interaction length scale L depends on both the detuning of the atomic transition into the band gap and α, the curvature of the band at the band edge, which can be well approximated by a local quadratic fit. Lastly, the $u(x)$ functions account for the Bloch periodic mode profile of the guided modes.

What makes this Hamiltonian interesting to study is that the length scale of the interactions is tunable by altering the detuning Δ_{BE}. This can be accomplished via the same heating laser induced thermal tuning we implement in our system [22, 91]. The interaction strength can also be tuned by altering the interatomic distance. This is in direct contrast to the typical Jaynes-Cummings spin exchange interaction, which is is not distance-dependent within the cavity mode volume. Tunable, long-range interactions are a core requirement to probe novel regimes of quantum many-body phenomena and this platform naturally provides a route towards achieving this goal. One thing to note is that while the interactions here are characterized by exponential decay, typically understood as short-range, they can exhibit length scales approaching the length of the photonic crystal rendering them effectively long-ranged.

5.2.2 Freezable Dynamics

The two primary dissipation channels to consider for this system are similar to those of standard atom-cavity experiments: an atom in the excited state can decay, emitting a photon either to free space or to a defect waveguide mode with total rate γ' or the bound photon can be lost due to imperfections in the photonic crystal with rate κ. The atomic decay rate γ' should be slightly less than the free-space atomic decay rate γ_0 because decay to modes along the waveguide are prevented due to the photonic band gap. The bound

photon loss rate κ in these systems has yet to be measured, though it is expected to be similar to that of photonic crystal cavities fabricated with the same techniques, as loss from both systems is due primarily to fabrication imperfections [19, 162]. It has been shown that since the excitation is predominantly atomic in nature with a small photonic component, the photonic loss is suppressed to leading order by a factor of $\kappa/4\Delta_{BE}$ [58]. This term can be neglected to first order as we expect $\Delta_{BE} >> \kappa$ and we can slightly overestimate $\gamma' \simeq \gamma_0$.

One improvement to the setup involves considering an atomic Λ scheme whereby we encode our spin in the metastable ground state manifold $\{|g\rangle, |s\rangle\}$ where the $|g\rangle - |e\rangle$ transition is coupled via the photonic crystal band edge as before with detuning Δ_{BE} and the $|s\rangle - |e\rangle$ transition is off-resonantly driven by a Raman laser with Rabi frequency Ω_R and detuning δ_R satisfying $|\delta_R| >> |\Omega_R|$. This leads to a spin exchange Hamiltonian of the same form as Equation (5.1) where the following replacements are made: $\delta_{eff} = 2\Delta_{BE} \rightarrow 2\overline{\Delta} = 2(\omega_a - \omega_{BE} - \delta_R)$; $g_{eff} \rightarrow \overline{g}_{eff} = g_{eff}(\Omega_R/\delta_R)$; $\sigma_{eg}\sigma_{ge} \rightarrow \sigma_{sg}\sigma_{gs}$. This scheme reduces the interaction strength and thus the timescale of the dynamics by a factor of $(\Omega_R/\delta_R)^2$, yet also reduces the virtual excited state population and loss dynamics by the same factor. Overall, this maintains a constant cooperativity [58]. Note that we must also replace the factor of Δ_{BE} in the equation for the bound photon length scale L with the new $\overline{\Delta}$. This scheme is advantageous as it allows for dynamic control of the interaction length scale L via the detuning of the Raman laser rather than relying upon precise control over the band edge of the nanophotonic structure via thermal effects. It also enables the interaction to be removed by turning off the Raman beam, “freezing" the state of the system for readout, allowing for more precise probing of the system dynamics.

To briefly further motivate the long-term potential of this platform as a quantum many-body simulator, it has been shown that with additional Raman lasers, these interactions can be designed to approximate power law decay quite well over relevant experimental length scales [58]. Introducing local energy shifts via a magnetic field gradient or AC Stark shifts

along with sidebands to the Raman beams, which can be introduced for example with electro-optic modulators, allows for the realization of pairwise, tunable interactions and a very broad class of spin Hamiltonians [150]. Topological order in 1D chains can be introduced via Floquet driving [163]. In addition, extending this physics to 2D photonic crystals enables the study of 2D topologically nontrivial models [150, 151].

5.2.3 Waveguide Designs

Here we present some photonic crystal waveguide designs compatible with the tunable atom-atom interactions discussed above.

TE Mode Design

Let us begin by considering a typical nanophotonic crystal waveguide structure consisting of a periodic array of holes in silicon nitride. We choose silicon nitride for the same reasons we use it in our current experiments: it has well-established nanofabrication techniques, a suitably large electronic band gap of $\sim$5 eV to avoid issues with our atomic addressing beams, good mechanical properties, and a low refractive index that allows the evanescent fields to extend farther from the structure, increasing the coupling to nearby trapped atoms. In order to realize the desired tunable atom-atom interactions, we must design our structure such that it has a single band edge closely aligned with our atomic transition frequency, which we choose to be the D_2 line of caesium at 351.725 THz (852 nm). We must simultaneously consider the standing wave traps formed by our partially reflected optical tweezer since the dimensions of the waveguide, especially the thickness, appreciably affect this trapping potential and the distance between the atom and the waveguide surface [21, 119]. Let's assume we use the same 935 nm wavelength for the tweezers, which is magic for the caesium D2 line. The design parameters depicted and detailed in Figure 5.2 align the lower transverse electric (TE, y-polarized) band edge with the caesium D_2 transition as desired. The band

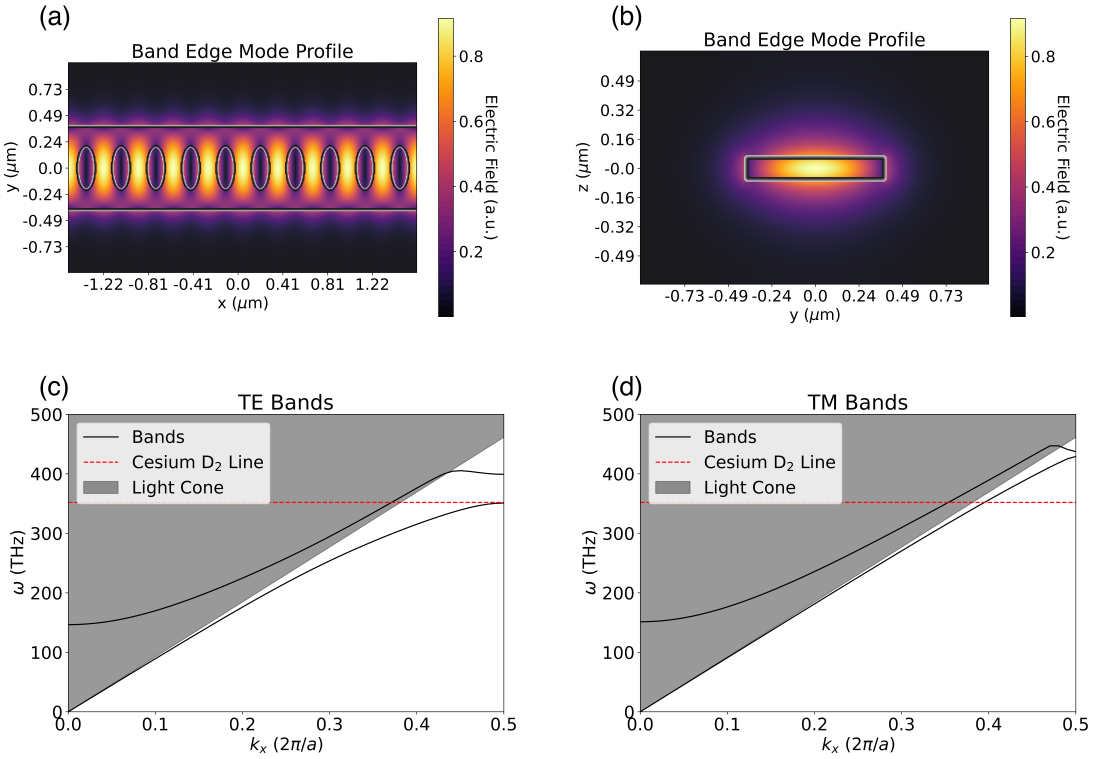

Figure 5.2: **A silicon nitride waveguide design featuring a width of 775 nm, a thickness of 125 nm, and a periodicity of 325 nm. The elliptical holes have major and minor radii of 200 nm and 80 nm respectively.** **a**, XY slice through the $z = 0$ plane of the electric field profile of the relevant TE band edge mode at 852 nm. **b**, YZ slice of the electric field profile of the TE band edge mode through the plane centered on the dielectric portion of the waveguide, halfway between the holes. **c**, TE band structure depicting the lowest two TE bands indicating the desired alignment of the lower band edge with the caesium D_2 transition. **d**, TM band structure depicting the lack of any band edges near the caesium transition.

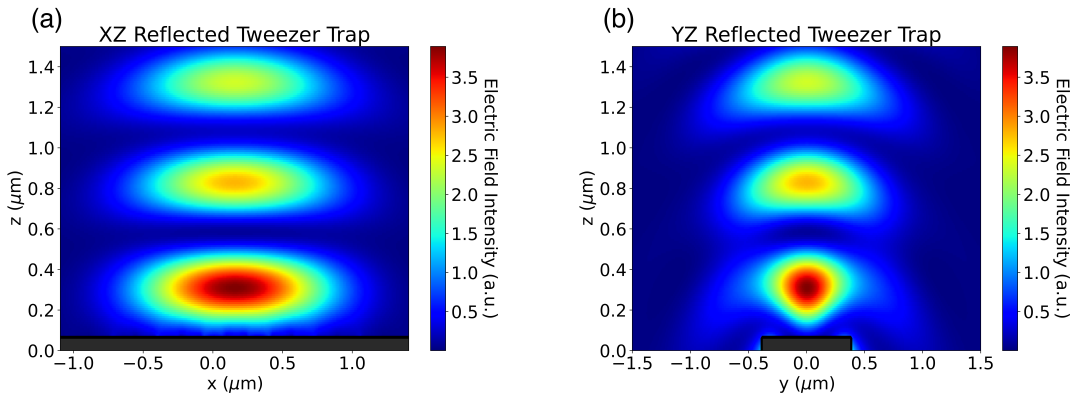

Figure 5.3: **Trapping potential above the nanophotonic crystal waveguide presented in Fig. 5.2 a**, XZ plane slice at $y = 0$. **b**, YZ plane slice centered between the waveguide holes of the reflected optical tweezer trap intensity profile. The gray region with black border indicates the waveguide.

structure of the transverse magnetic (TM, z-polarized) modes is also shown, however, the atom primarily couples to the nearby TE band edge modes due to the van Hove singularity in the density of states, and thus the approximately linear dispersion of the TM mode at the atomic transition frequency can be safely neglected.

Figure 5.3 depicts the trapping field intensity profile sliced along the XZ and YZ planes. These simulations were performed assuming we focus 935 nm light slightly below the waveguide with a 0.5 NA objective. Focusing slightly below the waveguide rather than directly on its top surface increases the relative intensity at the first maximum without appreciably altering the standing wave profile or trapping distance. This specific design yields a conservative trapping distance of 240 nm. This is quite far from the limit of ∼100 nm beyond which the atom will likely crash into the waveguide due to attractive surface forces for realistic laser intensities [21, 19]. Further details on reducing the trapping distance will be discussed in the following section along with projected improvements to the coherent interaction strength and dynamics.

Equipped with the band structure and trapping distance, we are in a position to examine the guided mode electric field profile at the band edge as shown in Figure 5.2 and to calculate the effective mode area A_{eff} and the band curvature α. We calculate the effective mode

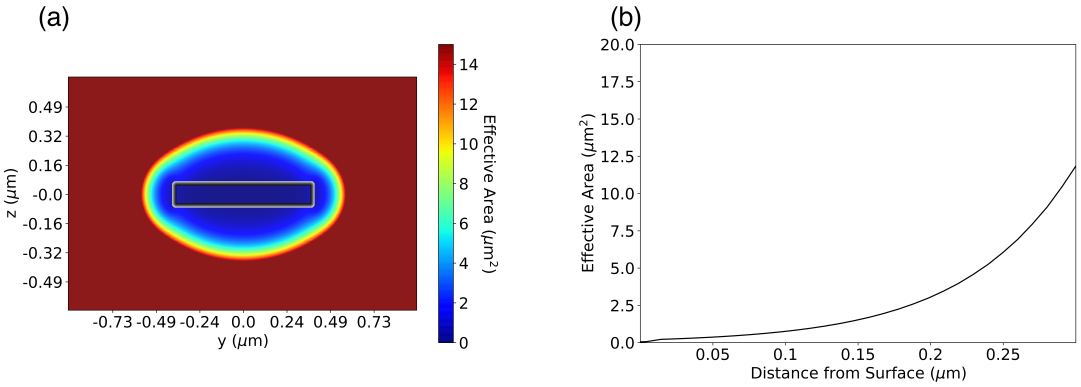

Figure 5.4: **Plots of the effective mode area used to calculate the effective atom-waveguide coupling. a**, The effective mode area used to calculate g_{eff} as a function of the atomic position near the waveguide. **b**, A slice along $y = 0$ as a function of the atom-surface distance.

area as a function of the atomic position r as in Ref. [93] with the following equation where a is the lattice constant of the waveguide and the integration runs over the unit cell along the waveguide and from $-\infty$ to ∞ in the transverse plane:

$$A_{eff}(r) = \frac{\int \epsilon(r')|E(r')|^2 d^3r'}{a\epsilon(r)|E(r)|^2} \tag{5.2}$$

Here, we note that the effective mode area increases as the atomic position moves farther from the waveguide and thus the coupling $g_{eff} \propto 1/A_{eff}$ decreases as expected. The effective mode area as a function of the atomic position is depicted in Figure 5.4. We calculate α by fitting the band near the band edge to the quadratic form given above to find $\alpha = 3.7$.

From here, there is one more detail to consider before simulating the Hamiltonian in Equation 5.1 for this specific set of experimental parameters, which is to discuss the detuning Δ, which determines the length scale of the interactions. In the atom-atom interaction scheme without the additional Raman laser, this detuning is controlled via an external heating laser that shifts the frequency of the band edge. Previous experiments have demonstrated the ability to tune this value to within an uncertainty of $\sim$5 GHz [22]. Initial results with our cavity frequency stabilization setup imply that this can be even more tightly controlled.

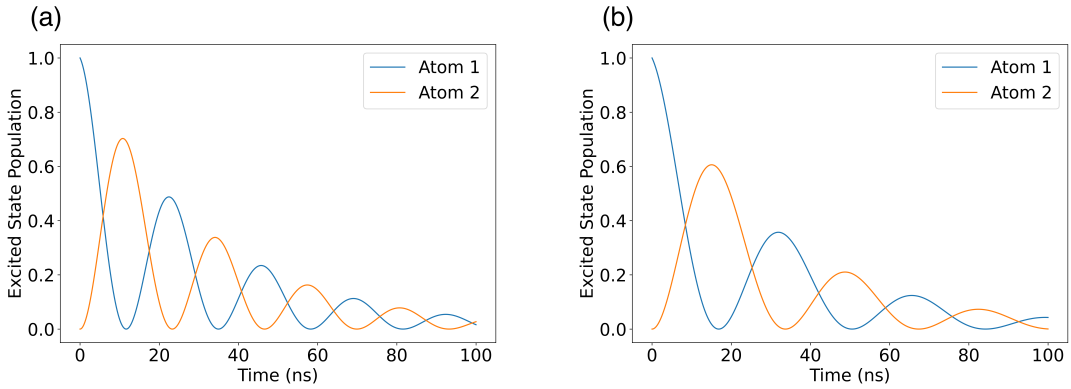

Figure 5.5: **Two atom excitation exchange dynamics mediated via the waveguide design presented in Fig. 5.2 a**, Assuming $\Delta_{BE} = 15$ GHz and $g_{eff} = 0.327 \times 2\pi$ GHz. **b**, Assuming $\Delta_{BE} = 30$ GHz and $g_{eff} = 0.388 \times 2\pi$ GHz. The coupling values g_{eff} were calculated using the mode area corresponding to a trapping distance of 240 nm. Here we have chosen the interatomic distance to be 10 unit cells or 3.25 μm.

In the spirit of making conservative predictions, we shall proceed to simulate our interactions with $\Delta_{BE} = 15$ GHz and $\Delta_{BE} = 30$ GHz, which are reasonable experimental values. More precise control and smaller effective detunings could be possible by utilizing the Raman scheme as the laser detuning can be very precisely controlled, though due to the constant cooperativity and consistent scaling of both interaction strength and loss mechanisms, it suffices to simulate the bare atom situation to get a feel for the competition between the coherent interactions and dissipation.

With this complete experimental design, we simulate our atom-atom interactions for the two atom case in order to characterize the system. As mentioned previously, we neglect the highly suppressed bound photon loss channels and take $\gamma' \simeq \gamma_0$. The results of the simulations are shown in Figure 5.5. The exchange dynamics are clearly visible and competing with dissipation. Keeping in mind that these design parameters have all been taken to be quite conservative and that there is much room for improvement, this is a good starting point for an initial feasibility study. The next section explores some further details and potential avenues towards improving these parameters along with some simulations of the projected improvements.

TM Mode Design

Here I briefly review some important details about trapping near nanophotonics. The scheme presented above is somewhat rudimentary and neglects the effects of attractive Casimir-Polder surface forces. In this specific trapping scheme, we are safely trapped quite far from the surface, and these forces should not pose an issue and may in fact prove to be helpful by slightly reducing our trapping distance and thus increasing our coupling. As our coupling g_{eff} is extremely sensitive to the atom-surface distance due to the exponential decay of the guided mode fields outside the waveguide and our atom-atom interaction strength is proportional to g_{eff}^2, a final design should not be so conservative. The trapping distance should be minimized as much as possible while maintaining a stable trapping potential, fully accounting for these surface force effects. To provide a general sense of scale and justify neglecting these forces here, we can use the approximate equation for the potential experienced by an atom near a planar dielectric surface $V_{CP} \approx -C_4/(d^3(d+\lambda\!\!\!^{-})$ [164, 165]. Here, d is the atom-surface distance, $\lambda\!\!\!^{-}$ is the length scale below which the potential transitions to $1/d^3$ and is given by the atomic transition wavelength divided by 2π. Lastly, C_4 is the coefficient of the $1/d^4$ potential, which can be approximated as $C_4/k_B \approx 5$ nK μK^4 for caesium near silicon nitride [165, 166, 167]. At the trapping distances in this proposal, the scale of this potential is $\sim$1-3 k$_B$ μK, while our trap depths are $\sim$2-4 k$_B$ mK for reasonable tweezer intensities $\sim$1 mW.

In addition, the trapping potential can be further modified by utilizing the nearly linear TM mode band. Alternative trapping schemes relying upon red-detuned (attractive) and blue-detuned (repulsive) guided mode fields have been used to create stable traps near dielectric surfaces and even incorporate these surface forces as part of the trap design [25, 26, 28, 30, 155]. With regard to the specific design above, changing the thickness to pull the reflected optical tweezer trap closer to the surface results in the electric field profile of the trapping potential penetrating the holes of the waveguide. This in itself is not

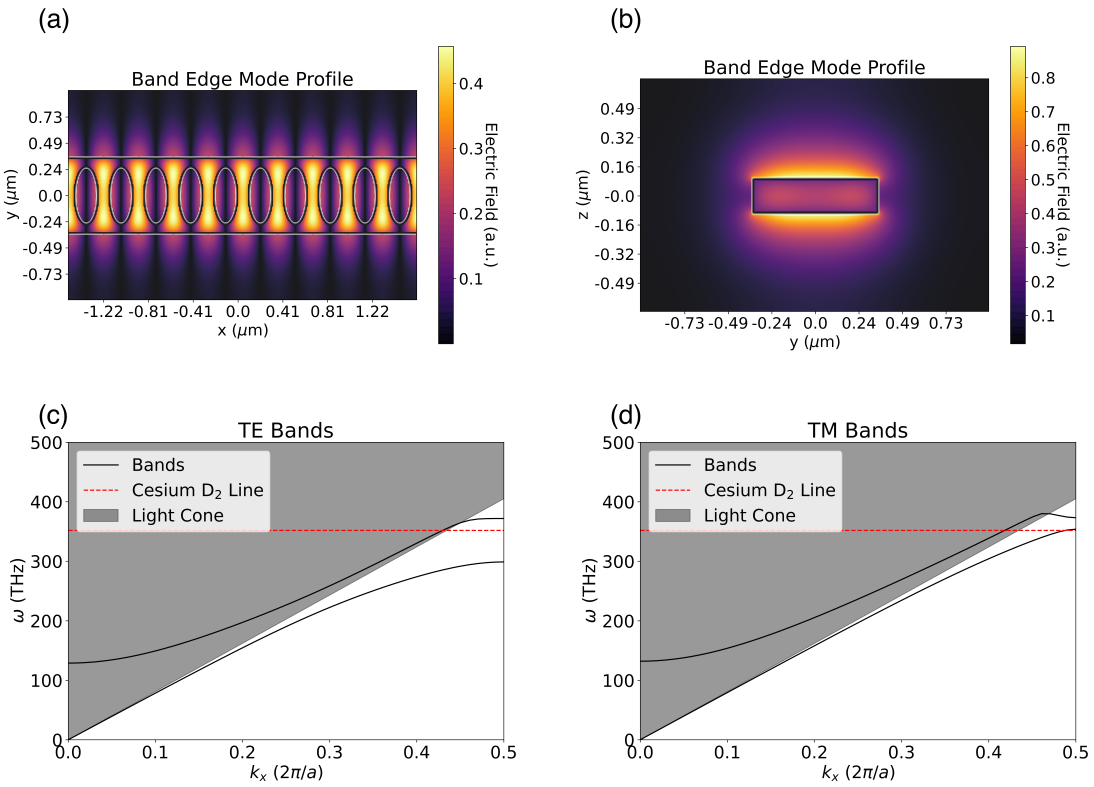

Figure 5.6: **An alternative silicon nitride waveguide designed to utilize the TM mode band edge featuring a width of 800 nm, a thickness of 220 nm, and a periodicity of 370 nm. The elliptical holes have major and minor radii of 300 nm and 120 nm respectively.** **a**, XY slice through the $z = 0$ plane of the electric field profile of the TM band edge mode. **b**, YZ slice centered between the waveguide holes of the electric field profile of the TM band edge mode. **c**, TE band structure depicting the lowest two TE bands showing the lack of band edge near the caesium D_2 transition. **d**, TM band structure depicting the desired alignment of the caesium transition to the lower band edge mode. Initial simulations show that the contribution of the upper band edge should be negligible despite the reduced band gap compared to the TE-based design.

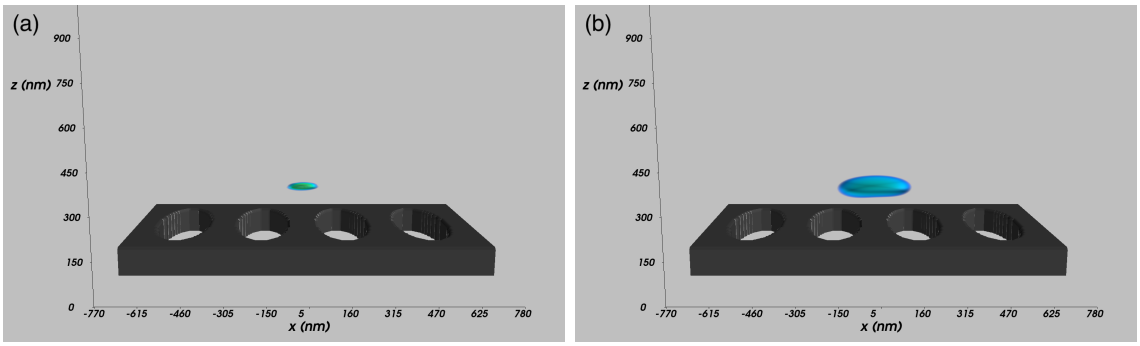

(a) Here we assume a tweezer power of 1.5 mW and an atomic temperature of 10 μK.

(b) Here we assume a tweezer power of 1 mW and an atomic temperature of 50 μK.

Figure 5.7: The atomic spatial distribution in the reflected tweezer trap above the redesigned TM waveguide. The edges of the visible atom clouds are chosen such that the probability to find the atom within the visible region is $\sim$90%.

a problem provided that the atomic confinement is strong enough in the z-direction near the first intensity maximum that the atom does not crash into the waveguide. However, if this is pushed too far and the atom is brought even closer, additional intensity maxima form at the edges of the waveguide holes, providing a route to crashing and rendering the trap unstable. One method to resolve this issue is by sending blue-detuned light through the waveguide TM mode, creating a larger potential barrier between the atom and the surface in order to prevent crashing and to re-stabilize the trap while maintaining a reduced atom-surface distance. It is also possible to pull the atom closer to the surface by launching a red-detuned mode into the waveguide to provide an additional attractive force to pull the atom closer to the surface, though a careful balance must be struck to maintain a stable trapping configuration. Utilizing a combination of these methods should allow for significant reduction of the trapping distance compared to the conservative design presented in the previous section.

Another proposal puts forth the idea to use superpositions of higher order Laguerre-Gauss beams rather than the typical Gaussian beams for reflected tweezer traps to reduce trap volume [153]. Increasing the confinement of the atom in the trap not only allows the trap to be brought closer to the surface of the waveguide but also reduces the range of couplings that the atomic wavepacket samples as it explores the trapping region at a given temperature

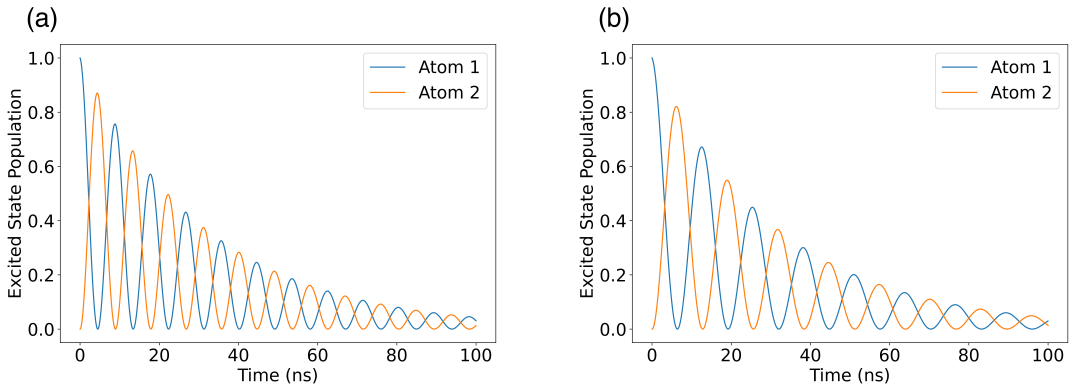

Figure 5.8: **Two atom excitation exchange dynamics for the TM design. a**, $\Delta_{BE} =$ 15 GHz and $g_{eff} = 0.524 \times 2\pi$ GHz. **b**, $\Delta_{BE} = 30$ GHz and $g_{eff} = 0.623 \times 2\pi$ GHz. Here we have chosen the interatomic distance to be 10 unit cells or 3.7 μm.

[91]. In addition, the reflections of these beams, which can be generated using a spatial light modulator, have much higher relative intensities in the closest intensity maximum, increasing the probability of loading into the desired trapping region.

The other main method by which g_{eff} can be increased beyond trapping the atom closer to the surface is by coupling to a mode that extends farther from the surface. One example is shown in Figure 5.6 where the physical design of the waveguide has been altered to align the lower TM band edge with the caesium D_2 line. The TE modes are also shown to demonstrate that we are still in a regime where the coupling is primarily to the single desired band edge. These TM modes are advantageous when the waveguide is thin enough as their mode profile predominantly exists above and below the waveguide and thus extends much farther from the surface, increasing the coupling. With this specific set of design parameters the polarization of the Gaussian trapping beam must be rotated by $\gtrsim 60^\circ$ with respect to the waveguide axis in order to create a stable trapping potential. Choosing a 60° polarization leads to stable trapping 180 nm above the waveguide surface. Figure 5.7 depicts the thermal atomic spatial distribution in 3D with this trapping scheme for two different temperature and tweezer power cases. The significant improvement to the coherent atom-atom dynamics relative to the initial design is shown in Figure 5.8. This improvement can be made even

more substantial if the curvature of the TM band can be reduced to be closer to that of the TE modes discussed above. This TM band has $\alpha = 8.4$, which increases the interaction length L and thus the mode volume, leading to slightly lower coupling than with flatter band edges.

Additional improvements can be made by reducing dissipation rather than by focusing on increasing the coupling. One method by which this can be achieved is to embed the waveguide in a 2D photonic crystal slab such that the atomic transition lies within the band gap for all wavevectors in the plane. By reducing the available modes that the atom can decay into, the atomic decay rate while coupled to the nanophotonic can be reduced relative to the free-space decay rate by up to a factor of nearly $\frac{1}{2}$ [168].

CHAPTER 6

CONCLUSION

This thesis has presented the design, construction, and operation of a novel experimental platform that integrates a reconfigurable atom array with a nanophotonic chip hosting an array of over 100 telecom-band nanophotonic crystal cavities. By combining two essential tools in atomic physics, optical tweezer arrays and cavity-enhanced light-matter interactions, this work lays a foundation for scalable, chip-integrated atomic systems.

Three essential features underlie the success of this platform. First, our semi-open chip geometry enables the operation of a free-space atom array, mere microns away from an array of cantilevered nanophotonic crystal cavities overhanging the edge of the chip. This design facilitates sufficient optical access for laser cooling and allows for straightforward side-loading of atoms into standing wave traps above the cavity surfaces. Second, our background-free imaging technique overcomes the scattering challenge due to the nearby dielectric surface, enabling parallel, site-resolved, single-shot readout via fluorescence imaging in close proximity to the nanophotonic chip. Third, we demonstrate free-space coupling of light to and from the photonic crystal cavities, opening the door to future multiplexing experiments leveraging the large array of cavities fabricated on our chip.

Using these capabilities, we have demonstrated essential atom array experimental techniques such as rearrangement, unhindered by the nearby chip. We have also laid the groundwork for the next phase of experiments probing atom-cavity coupling by implementing a thermal cavity frequency stabilization protocol, integrating fast, sub-nanosecond optical pulse generation, and incorporating single-photon detection and time tagging infrastructure. Looking ahead, we have outlined several promising paths forward including quantum networking directly in the telecom-band, spatial multiplexing across the cavity array, quantum simulation protocols enabled by coupling atom arrays to nanophotonic crystal waveguides, and further detailed investigations of Rydberg interactions near dielectric surfaces.

This work fits into a broader effort to build hybrid quantum systems that combine the unique strengths of distinct platforms. Here, we have focused on improving the scalability of integrated atom-nanophotonic systems, moving beyond the single-device, few-atom regime towards the many-atom, many-device regime. This step marks an important milestone on the path to distributed, modular quantum information systems and novel regimes of quantum many-body physics leveraging engineered photonic environments.

REFERENCES

[1] R. P. Feynman, "Simulating physics with computers," *International Journal of Theoretical Physics*, vol. 21, pp. 467–488, June 1982.

[2] Y. Manin, *Computable and Uncomputable*. Moscow: Sovetskoye Radio, 1980.

[3] J. Preskill, "Quantum computing 40 years later," Feb. 2023. arXiv:2106.10522 [quant-ph].

[4] D. Deutsch and R. Penrose, "Quantum theory, the Church–Turing principle and the universal quantum computer," *Proceedings of the Royal Society of London. A. Mathematical and Physical Sciences*, vol. 400, pp. 97–117, July 1985.

[5] P. W. Shor, "Polynomial-Time Algorithms for Prime Factorization and Discrete Logarithms on a Quantum Computer," *SIAM Journal on Computing*, vol. 26, pp. 1484–1509, Oct. 1997. arXiv:quant-ph/9508027.

[6] L. K. Grover, "A fast quantum mechanical algorithm for database search," in *Proceedings of the twenty-eighth annual ACM symposium on Theory of Computing*, STOC '96, (New York, NY, USA), pp. 212–219, Association for Computing Machinery, July 1996.

[7] C. H. Bennett and G. Brassard, "Quantum cryptography: Public key distribution and coin tossing," *Theoretical Computer Science*, vol. 560, pp. 7–11, Dec. 2014.

[8] D. P. DiVincenzo, "The Physical Implementation of Quantum Computation," *Fortschritte der Physik*, vol. 48, no. 9-11, pp. 771–783, 2000.

[9] H. J. Manetsch, G. Nomura, E. Bataille, K. H. Leung, X. Lv, and M. Endres, "A tweezer array with 6100 highly coherent atomic qubits," Dec. 2024. arXiv:2403.12021 [quant-ph].

[10] S. J. Evered, D. Bluvstein, M. Kalinowski, S. Ebadi, T. Manovitz, H. Zhou, S. H. Li, A. A. Geim, T. T. Wang, N. Maskara, H. Levine, G. Semeghini, M. Greiner, V. Vuletić, and M. D. Lukin, "High-fidelity parallel entangling gates on a neutral-atom quantum computer," *Nature*, vol. 622, pp. 268–272, Oct. 2023.

[11] M. Peper, Y. Li, D. Y. Knapp, M. Bileska, S. Ma, G. Liu, P. Peng, B. Zhang, S. P. Horvath, A. P. Burgers, and J. D. Thompson, "Spectroscopy and Modeling of ^{171}Yb Rydberg States for High-Fidelity Two-Qubit Gates," *Physical Review X*, vol. 15, no. 1, 2025.

[12] I. S. Madjarov, J. P. Covey, A. L. Shaw, J. Choi, A. Kale, A. Cooper, H. Pichler, V. Schkolnik, J. R. Williams, and M. Endres, "High-fidelity entanglement and detection of alkaline-earth Rydberg atoms," *Nature Physics*, vol. 16, pp. 857–861, Aug. 2020.

[13] J. A. Muniz, M. Stone, D. T. Stack, M. Jaffe, J. M. Kindem, L. Wadleigh, E. Zalys-Geller, X. Zhang, C.-A. Chen, M. A. Norcia, J. Epstein, E. Halperin, F. Hummel, T. Wilkason, M. Li, K. Barnes, P. Battaglino, T. C. Bohdanowicz, G. Booth, A. Brown, M. O. Brown, W. B. Cairncross, K. Cassella, R. Coxe, D. Crow, M. Feldkamp, C. Griger, A. Heinz, A. M. W. Jones, R. Morshead, S. Narayanaswami, C. Nishiguchi, T. Paule, K. A. Pawlak, K. L. Pudenz, D. Rodríguez Pérez, A. Ryou, J. Simon, A. Smull, M. Urbanek, R. J. M. van de Veerdonk, Z. Vendeiro, T.-Y. Wu, X. Xie, and B. J. Bloom, "High-Fidelity Universal Gates in the ^{171}Yb Ground-State Nuclear-Spin Qubit," *PRX Quantum*, vol. 6, no. 2, 2025.

[14] D. Bluvstein, S. J. Evered, A. A. Geim, S. H. Li, H. Zhou, T. Manovitz, S. Ebadi, M. Cain, M. Kalinowski, D. Hangleiter, J. P. Bonilla Ataides, N. Maskara, I. Cong, X. Gao, P. Sales Rodriguez, T. Karolyshyn, G. Semeghini, M. J. Gullans, M. Greiner, V. Vuletić, and M. D. Lukin, "Logical quantum processor based on reconfigurable atom arrays," *Nature*, vol. 626, pp. 58–65, Feb. 2024.

[15] M. Saffman, "Quantum computing with atomic qubits and Rydberg interactions: progress and challenges," *Journal of Physics B: Atomic, Molecular and Optical Physics*, vol. 49, p. 202001, Oct. 2016.

[16] S. Haroche, "A short history of cavity quantum electrodynamics," p. CTuF2, Optical Society of America, June 2007.

[17] A. Reiserer and G. Rempe, "Cavity-based quantum networks with single atoms and optical photons," *Reviews of Modern Physics*, vol. 87, pp. 1379–1418, Dec. 2015.

[18] A. Reiserer, "Colloquium: Cavity-enhanced quantum network nodes," *Reviews of Modern Physics*, vol. 94, p. 041003, Dec. 2022.

[19] D. Chang, J. Douglas, A. González-Tudela, C.-L. Hung, and H. Kimble, "Colloquium: Quantum matter built from nanoscopic lattices of atoms and photons," *Reviews of Modern Physics*, vol. 90, Aug. 2018.

[20] M. Brekenfeld, D. Niemietz, J. D. Christesen, and G. Rempe, "A quantum network node with crossed optical fibre cavities," *Nature Physics*, pp. 1–5, Apr. 2020.

[21] J. D. Thompson, T. G. Tiecke, N. P. de Leon, J. Feist, A. V. Akimov, M. Gullans, A. S. Zibrov, V. Vuletic, and M. D. Lukin, "Coupling a Single Trapped Atom to a Nanoscale Optical Cavity," *Science*, vol. 340, pp. 1202–1205, June 2013.

[22] J. D. Hood, A. Goban, A. Asenjo-Garcia, M. Lu, S.-P. Yu, D. E. Chang, and H. J. Kimble, "Atom–atom interactions around the band edge of a photonic crystal waveguide," *Proceedings of the National Academy of Sciences*, vol. 113, pp. 10507–10512, Sept. 2016.

[23] P. Lodahl, S. Mahmoodian, and S. Stobbe, "Interfacing single photons and single quantum dots with photonic nanostructures," *Reviews of Modern Physics*, vol. 87, pp. 347–400, May 2015.

[24] T. G. Tiecke, J. D. Thompson, N. P. de Leon, L. R. Liu, V. Vuletić, and M. D. Lukin, "Nanophotonic quantum phase switch with a single atom," *Nature*, vol. 508, pp. 241–244, Apr. 2014.

[25] E. Vetsch, D. Reitz, G. Sagué, R. Schmidt, S. T. Dawkins, and A. Rauschenbeutel, "Optical Interface Created by Laser-Cooled Atoms Trapped in the Evanescent Field Surrounding an Optical Nanofiber," *Physical Review Letters*, vol. 104, May 2010.

[26] E. Vetsch, S. T. Dawkins, R. Mitsch, D. Reitz, P. Schneeweiss, and A. Rauschenbeutel, "Nanofiber-Based Optical Trapping of Cold Neutral Atoms," *IEEE Journal of Selected Topics in Quantum Electronics*, vol. 18, pp. 1763–1770, Nov. 2012.

[27] C. Lacroûte, K. S. Choi, A. Goban, D. J. Alton, D. Ding, N. P. Stern, and H. J. Kimble, "A state-insensitive, compensated nanofiber trap," *New Journal of Physics*, vol. 14, p. 023056, Feb. 2012.

[28] A. Goban, K. S. Choi, D. J. Alton, D. Ding, C. Lacroûte, M. Pototschnig, T. Thiele, N. P. Stern, and H. J. Kimble, "Demonstration of a State-Insensitive, Compensated Nanofiber Trap," *Physical Review Letters*, vol. 109, p. 033603, July 2012.

[29] C.-L. Hung, S. M. Meenehan, D. E. Chang, O. Painter, and H. J. Kimble, "Trapped atoms in one-dimensional photonic crystals," *New Journal of Physics*, vol. 15, p. 083026, Aug. 2013.

[30] D. E. Chang, K. Sinha, J. M. Taylor, and H. J. Kimble, "Trapping atoms using nanoscale quantum vacuum forces," *Nature Communications*, vol. 5, p. 4343, July 2014.

[31] S. G. Menon, N. Glachman, M. Pompili, A. Dibos, and H. Bernien, "An integrated atom array-nanophotonic chip platform with background-free imaging," *Nature Communications*, vol. 15, p. 6156, July 2024.

[32] T. W. Hänsch and A. L. Schawlow, "Cooling of gases by laser radiation," *Optics Communications*, vol. 13, pp. 68–69, Jan. 1975.

[33] D. Wineland and H. Dehmelt, "Proposed $10^{14}\ \Delta\nu < \nu$ Laser Fluorescence Spectroscopy on Tl^{+} Mono-Ion Oscillator," *Bulletin of the American Physical Society*, vol. 20, no. 637, 1975.

[34] D. J. Wineland, R. E. Drullinger, and F. L. Walls, "Radiation-Pressure Cooling of Bound Resonant Absorbers," *Physical Review Letters*, vol. 40, pp. 1639–1642, June 1978.

[35] W. Neuhauser, M. Hohenstatt, P. Toschek, and H. Dehmelt, "Optical-Sideband Cooling of Visible Atom Cloud Confined in Parabolic Well," *Physical Review Letters*, vol. 41, pp. 233–236, July 1978.

[36] W. D. Phillips and H. Metcalf, "Laser Deceleration of an Atomic Beam," *Physical Review Letters*, vol. 48, pp. 596–599, Mar. 1982.

[37] S. Chu, L. Hollberg, J. E. Bjorkholm, A. Cable, and A. Ashkin, "Three-dimensional viscous confinement and cooling of atoms by resonance radiation pressure," *Physical Review Letters*, vol. 55, pp. 48–51, July 1985. Publisher: American Physical Society.

[38] E. L. Raab, M. Prentiss, A. Cable, S. Chu, and D. E. Pritchard, "Trapping of Neutral Sodium Atoms with Radiation Pressure," *Physical Review Letters*, vol. 59, no. 23, pp. 2631–2634, 1987.

[39] P. D. Lett, R. N. Watts, C. I. Westbrook, W. D. Phillips, P. L. Gould, and H. J. Metcalf, "Observation of Atoms Laser Cooled below the Doppler Limit," *Physical Review Letters*, vol. 61, no. 2, pp. 169–172, 1988.

[40] R. Grimm, M. Weidemüller, and Y. B. Ovchinnikov, "Optical dipole traps for neutral atoms," Feb. 1999. arXiv: physics/9902072.

[41] S. Chu, J. E. Bjorkholm, A. Ashkin, and A. Cable, "Experimental Observation of Optically Trapped Atoms," *Physical Review Letters*, vol. 57, no. 3, pp. 314–317, 1986.

[42] N. Schlosser, G. Reymond, I. Protsenko, and P. Grangier, "Sub-poissonian loading of single atoms in a microscopic dipole trap," *Nature*, vol. 411, pp. 1024–1027, June 2001.

[43] N. Schlosser, G. Reymond, and P. Grangier, "Collisional Blockade in Microscopic Optical Dipole Traps," *Physical Review Letters*, vol. 89, p. 023005, June 2002.

[44] S. K. Pampel, M. Marinelli, M. O. Brown, J. P. D'Incao, and C. A. Regal, "Quantifying Light-assisted Collisions in Optical Tweezers Across the Hyperfine Spectrum," *Physical Review Letters*, vol. 134, p. 013202, Jan. 2025.

[45] R. Dumke, M. Volk, T. Müther, F. B. J. Buchkremer, G. Birkl, and W. Ertmer, "Micro-optical Realization of Arrays of Selectively Addressable Dipole Traps: A Scalable Configuration for Quantum Computation with Atomic Qubits," *Physical Review Letters*, vol. 89, no. 9, 2002.

[46] D. Schäffner, T. Preuschoff, S. Ristok, L. Brozio, M. Schlosser, H. Giessen, and G. Birkl, "Arrays of individually controllable optical tweezers based on 3D-printed microlens arrays," *Optics Express*, vol. 28, pp. 8640–8645, Mar. 2020.

[47] M. Schlosser, S. Tichelmann, D. Schäffner, D. O. De Mello, M. Hambach, J. Schütz, and G. Birkl, "Scalable Multilayer Architecture of Assembled Single-Atom Qubit Arrays in a Three-Dimensional Talbot Tweezer Lattice," *Physical Review Letters*, vol. 130, p. 180601, May 2023.

[48] L. Pause, L. Sturm, M. Mittenbühler, S. Amann, T. Preuschoff, D. Schäffner, M. Schlosser, and G. Birkl, "Supercharged two-dimensional tweezer array with more than 1000 atomic qubits," *Optica*, vol. 11, pp. 222–226, Feb. 2024.

[49] T.-W. Hsu, W. Zhu, T. Thiele, M. O. Brown, S. B. Papp, A. Agrawal, and C. A. Regal, "Single-Atom Trapping in a Metasurface-Lens Optical Tweezer," *PRX Quantum*, vol. 3, p. 030316, Aug. 2022.

[50] M. Fox, *Quantum Optics: An Introduction*. OUP Oxford, Apr. 2006.

[51] E. M. Purcell, H. C. Torrey, and R. V. Pound, "Resonance Absorption by Nuclear Magnetic Moments in a Solid," *Physical Review*, vol. 69, no. 1-2, pp. 37–38, 1946.

[52] E. T. Jaynes and F. W. Cummings, "Comparison of quantum and semiclassical radiation theories with application to the beam maser," *Proceedings of the IEEE*, vol. 51, pp. 89–109, Jan. 1963.

[53] G. Rempe, H. Walther, and N. Klein, "Observation of quantum collapse and revival in a one-atom maser," *Physical Review Letters*, vol. 58, pp. 353–356, Jan. 1987.

[54] R. J. Thompson, G. Rempe, and H. J. Kimble, "Observation of normal-mode splitting for an atom in an optical cavity," *Physical Review Letters*, vol. 68, no. 8, pp. 1132–1135, 1992.

[55] A. Boca, R. Miller, K. M. Birnbaum, A. D. Boozer, J. McKeever, and H. J. Kimble, "Observation of the Vacuum Rabi Spectrum for One Trapped Atom," *Physical Review Letters*, vol. 93, no. 23, 2004.

[56] P. Maunz, T. Puppe, I. Schuster, N. Syassen, P. W. H. Pinkse, and G. Rempe, "Normal-Mode Spectroscopy of a Single-Bound-Atom–Cavity System," *Physical Review Letters*, vol. 94, no. 3, 2005.

[57] J. D. Joannopoulos, S. G. Johnson, J. N. Winn, and R. D. Meade, *Photonic Crystals: Molding the Flow of Light*. Princeton University Press, revised 2 ed., 2008.

[58] J. S. Douglas, H. Habibian, C.-L. Hung, A. V. Gorshkov, H. J. Kimble, and D. E. Chang, "Quantum many-body models with cold atoms coupled to photonic crystals," *Nature Photonics*, vol. 9, pp. 326–331, May 2015.

[59] A. S. Sheremet, M. I. Petrov, I. V. Iorsh, A. V. Poshakinskiy, and A. N. Poddubny, "Waveguide quantum electrodynamics: Collective radiance and photon-photon correlations," *Reviews of Modern Physics*, vol. 95, no. 1, 2023.

[60] V. Paulisch, H. J. Kimble, and A. González-Tudela, "Universal quantum computation in waveguide QED using decoherence free subspaces," *New Journal of Physics*, vol. 18, p. 043041, Apr. 2016.

[61] A. González-Tudela, V. Paulisch, H. Kimble, and J. Cirac, "Efficient Multiphoton Generation in Waveguide Quantum Electrodynamics," *Physical Review Letters*, vol. 118, p. 213601, May 2017.

[62] E. Sánchez-Burillo, A. González-Tudela, and C. Gonzalez-Ballestero, "Theory of waveguide QED with moving emitters," *Physical Review A*, vol. 102, no. 1, 2020.

[63] N. Fayard, L. Henriet, A. Asenjo-Garcia, and D. Chang, "Many-body localization in waveguide QED," *Physical Review Research*, vol. 3, p. 033233, Sept. 2021.

[64] G. Calajó, F. Ciccarello, D. Chang, and P. Rabl, "Atom-field dressed states in slow-light waveguide QED," *Physical Review A*, vol. 93, p. 033833, Mar. 2016.

[65] S. Mahmoodian, G. Calajó, D. E. Chang, K. Hammerer, and A. S. Sørensen, "Dynamics of Many-Body Photon Bound States in Chiral Waveguide QED," *Physical Review X*, vol. 10, p. 031011, July 2020.

[66] G. Pichard, D. Lim, Bloch, J. Vaneecloo, L. Bourachot, G.-J. Both, G. Mériaux, S. Dutartre, R. Hostein, J. Paris, B. Ximenez, A. Signoles, A. Browaeys, T. Lahaye, and D. Dreon, "Rearrangement of individual atoms in a 2000-site optical-tweezer array at cryogenic temperatures," *Physical Review Applied*, vol. 22, no. 2, 2024.

[67] M. A. Norcia, H. Kim, W. B. Cairncross, M. Stone, A. Ryou, M. Jaffe, M. O. Brown, K. Barnes, P. Battaglino, T. C. Bohdanowicz, A. Brown, K. Cassella, C. A. Chen, R. Coxe, D. Crow, J. Epstein, C. Griger, E. Halperin, F. Hummel, A. M. W. Jones, J. M. Kindem, J. King, K. Kotru, J. Lauigan, M. Li, M. Lu, E. Megidish, J. Marjanovic, M. McDonald, T. Mittiga, J. A. Muniz, S. Narayanaswami, C. Nishiguchi, T. Paule, K. A. Pawlak, L. S. Peng, K. L. Pudenz, D. Rodríguez Pérez, A. Smull, D. Stack, M. Urbanek, R. J. M. van de Veerdonk, Z. Vendeiro, L. Wadleigh, T. Wilkason, T.-Y. Wu, X. Xie, E. Zalys-Geller, X. Zhang, and B. J. Bloom, "Iterative Assembly of ^{171}Yb Atom Arrays with Cavity-Enhanced Optical Lattices," *PRX Quantum*, vol. 5, no. 3, 2024.

[68] D. Bluvstein, H. Levine, G. Semeghini, T. T. Wang, S. Ebadi, M. Kalinowski, A. Keesling, N. Maskara, H. Pichler, M. Greiner, V. Vuletić, and M. D. Lukin, "A quantum processor based on coherent transport of entangled atom arrays," *Nature*, vol. 604, pp. 451–456, Apr. 2022.

[69] A. W. Young, W. J. Eckner, W. R. Milner, D. Kedar, M. A. Norcia, E. Oelker, N. Schine, J. Ye, and A. M. Kaufman, "Half-minute-scale atomic coherence and high relative stability in a tweezer clock," *Nature*, vol. 588, pp. 408–413, Dec. 2020.

[70] D. Barredo, V. Lienhard, S. de Léséleuc, T. Lahaye, and A. Browaeys, "Synthetic three-dimensional atomic structures assembled atom by atom," *Nature*, vol. 561, pp. 79–82, Sept. 2018.

[71] M. Endres, H. Bernien, A. Keesling, H. Levine, E. R. Anschuetz, A. Krajenbrink, C. Senko, V. Vuletic, M. Greiner, and M. D. Lukin, "Atom-by-atom assembly of defect-free one-dimensional cold atom arrays," *Science*, vol. 354, pp. 1024–1027, Nov. 2016.

[72] D. Barredo, S. d. Léséleuc, V. Lienhard, T. Lahaye, and A. Browaeys, "An atom-by-atom assembler of defect-free arbitrary two-dimensional atomic arrays," *Science*, vol. 354, pp. 1021–1023, Nov. 2016.

[73] T. Wilk, A. Gaëtan, C. Evellin, J. Wolters, Y. Miroshnychenko, P. Grangier, and A. Browaeys, "Entanglement of Two Individual Neutral Atoms Using Rydberg Blockade," *Physical Review Letters*, vol. 104, no. 1, 2010.

[74] L. Isenhower, E. Urban, X. L. Zhang, A. T. Gill, T. Henage, T. A. Johnson, T. G. Walker, and M. Saffman, "Demonstration of a Neutral Atom Controlled-NOT Quantum Gate," *Physical Review Letters*, vol. 104, no. 1, 2010.

[75] W. B. Cairncross, J. T. Zhang, L. R. B. Picard, Y. Yu, K. Wang, and K.-K. Ni, "Assembly of a Rovibrational Ground State Molecule in an Optical Tweezer," *Physical Review Letters*, vol. 126, no. 12, 2021.

[76] D. W. Vernooy and H. J. Kimble, "Quantum structure and dynamics for atom galleries," *Physical Review A*, vol. 55, no. 2, pp. 1239–1261, 1997.

[77] J. R. Buck and H. J. Kimble, "Optimal sizes of dielectric microspheres for cavity QED with strong coupling," *Physical Review A*, vol. 67, no. 3, 2003.

[78] F. Le Kien, V. I. Balykin, and K. Hakuta, "Atom trap and waveguide using a two-color evanescent light field around a subwavelength-diameter optical fiber," *Physical Review A*, vol. 70, p. 063403, Dec. 2004.

[79] B. Lev, K. Srinivasan, P. Barclay, O. Painter, and H. Mabuchi, "Feasibility of detecting single atoms using photonic bandgap cavities," *Nanotechnology*, vol. 15, p. S556, July 2004.

[80] S. M. Spillane, T. J. Kippenberg, K. J. Vahala, K. W. Goh, E. Wilcut, and H. J. Kimble, "Ultrahigh-Q toroidal microresonators for cavity quantum electrodynamics," *Physical Review A*, vol. 71, no. 1, 2005.

[81] T. Aoki, B. Dayan, E. Wilcut, W. P. Bowen, A. S. Parkins, T. J. Kippenberg, K. J. Vahala, and H. J. Kimble, "Observation of strong coupling between one atom and a monolithic microresonator," *Nature*, vol. 443, pp. 671–674, Oct. 2006.

[82] D. O'Shea, C. Junge, J. Volz, and A. Rauschenbeutel, "Fiber-Optical Switch Controlled by a Single Atom," *Physical Review Letters*, vol. 111, p. 193601, Nov. 2013. Publisher: American Physical Society.

[83] I. Shomroni, S. Rosenblum, Y. Lovsky, O. Bechler, G. Guendelman, and B. Dayan, "All-optical routing of single photons by a one-atom switch controlled by a single photon," *Science*, vol. 345, pp. 903–906, Aug. 2014.

[84] Y. Colombe, T. Steinmetz, G. Dubois, F. Linke, D. Hunger, and J. Reichel, "Strong atom–field coupling for Bose–Einstein condensates in an optical cavity on a chip," *Nature*, vol. 450, pp. 272–276, Nov. 2007.

[85] J. Volz, R. Gehr, G. Dubois, J. Estève, and J. Reichel, "Measurement of the internal state of a single atom without energy exchange," *Nature*, vol. 475, pp. 210–213, July 2011.

[86] B. Grinkemeyer, E. Guardado-Sanchez, I. Dimitrova, D. Shchepanovich, G. E. Mandopoulou, J. Borregaard, V. Vuletić, and M. D. Lukin, "Error-detected quantum operations with neutral atoms mediated by an optical cavity," *Science*, vol. 387, pp. 1301–1305, Mar. 2025.

[87] K. P. Nayak, P. N. Melentiev, M. Morinaga, F. L. Kien, V. I. Balykin, and K. Hakuta, "Optical nanofiber as an efficient tool for manipulating and probing atomic fluorescence," *Optics Express*, vol. 15, no. 9, p. 5431, 2007.

[88] K. P. Nayak and K. Hakuta, "Single atoms on an optical nanofibre," *New Journal of Physics*, vol. 10, p. 053003, May 2008.

[89] Y. Meng, C. Liedl, S. Pucher, A. Rauschenbeutel, and P. Schneeweiss, "Imaging and Localizing Individual Atoms Interfaced with a Nanophotonic Waveguide," *Physical Review Letters*, vol. 125, p. 053603, July 2020.

[90] T. G. Tiecke, K. P. Nayak, J. D. Thompson, T. Peyronel, N. P. d. Leon, V. Vuletić, and M. D. Lukin, "Efficient fiber-optical interface for nanophotonic devices," *Optica*, vol. 2, pp. 70–75, Feb. 2015.

[91] P. Samutpraphoot, T. Đorđević, P. L. Ocola, H. Bernien, C. Senko, V. Vuletić, and M. D. Lukin, "Strong Coupling of Two Individually Controlled Atoms via a Nanophotonic Cavity," *Physical Review Letters*, vol. 124, p. 063602, Feb. 2020.

[92] P. L. Ocola, I. Dimitrova, B. Grinkemeyer, E. Guardado-Sanchez, T. Dordevic, P. Samutpraphoot, V. Vuletic, and M. D. Lukin, "Control and Entanglement of Individual Rydberg Atoms Near a Nanoscale Device," Oct. 2022. arXiv:2210.12879 [physics, physics:quant-ph].

[93] A. Goban, C.-L. Hung, S.-P. Yu, J. D. Hood, J. A. Muniz, J. H. Lee, M. J. Martin, A. C. McClung, K. S. Choi, D. E. Chang, O. Painter, and H. J. Kimble, "Atom–light interactions in photonic crystals," *Nature Communications*, vol. 5, p. 3808, May 2014.

[94] X. Luan, J.-B. Béguin, A. P. Burgers, Z. Qin, S.-P. Yu, and H. J. Kimble, "The Integration of Photonic Crystal Waveguides with Atom Arrays in Optical Tweezers," *Advanced Quantum Technologies*, vol. 3, no. 11, p. 2000008, 2020.

[95] S. Kato and T. Aoki, "Strong Coupling between a Trapped Single Atom and an All-Fiber Cavity," *Physical Review Letters*, vol. 115, p. 093603, Aug. 2015.

[96] M. E. Kim, T.-H. Chang, B. M. Fields, C.-A. Chen, and C.-L. Hung, "Trapping single atoms on a nanophotonic circuit with configurable tweezer lattices," *Nature Communications*, vol. 10, Dec. 2019.

[97] X. Zhou, H. Tamura, T.-H. Chang, and C.-L. Hung, "Subwavelength precision optical guiding for trapped atoms coupled to a nanophotonic resonator," *arXiv:2111.01119 [physics, physics:quant-ph]*, Nov. 2021. arXiv: 2111.01119.

[98] S. Sunami, S. Tamiya, R. Inoue, H. Yamasaki, and A. Goban, "Scalable Networking of Neutral-Atom Qubits: Nanofiber-Based Approach for Multiprocessor Fault-Tolerant Quantum Computers," *PRX Quantum*, vol. 6, p. 010101, Feb. 2025.

[99] D. A. Steck, "Cesium D Line Data," Jan. 1998.

[100] G. Yang, J. Wang, B. Yang, and J. Wang, "Determination of the hyperfine coupling constant of the cesium 7S1/2 state," *Laser Physics Letters*, vol. 13, p. 085702, July 2016.

[101] Y. He, J. Fan, L. Hao, Y. Jiao, and J. Zhao, "Precise Measurement of Hyperfine Structure of Cesium 7S1/2 Excited State," *Applied Sciences*, vol. 10, p. 525, Jan. 2020.

[102] A. Franzen, "ComponentLibrary: a free vector graphics library for optics."

[103] K. Singh, C. E. Bradley, S. Anand, V. Ramesh, R. White, and H. Bernien, "Mid-circuit correction of correlated phase errors using an array of spectator qubits," *Science*, vol. 380, pp. 1265–1269, June 2023.

[104] K. Singh, S. Anand, A. Pocklington, J. T. Kemp, and H. Bernien, "Dual-Element, Two-Dimensional Atom Array with Continuous-Mode Operation," *Physical Review X*, vol. 12, no. 1, 2022.

[105] S. Anand, C. E. Bradley, R. White, V. Ramesh, K. Singh, and H. Bernien, "A dual-species Rydberg array," *Nature Physics*, vol. 20, pp. 1744–1750, Nov. 2024.

[106] R. P. Abel, A. K. Mohapatra, M. G. Bason, J. D. Pritchard, K. J. Weatherill, U. Raitzsch, and C. S. Adams, "Laser frequency stabilization to excited state transitions using electromagnetically induced transparency in a cascade system," *Applied Physics Letters*, vol. 94, p. 071107, Feb. 2009.

[107] B.-D. Yang, J. He, and J.-M. Wang, "Off-resonant double-resonance optical-pumping spectra and their application in a multiphoton cesium magneto-optical trap," vol. 23, p. 054205, May 2014.

[108] H. S. Moon, L. Lee, and J. B. Kim, "Double resonance optical pumping effects in electromagnetically induced transparency," *Optics Express*, vol. 16, pp. 12163–12170, Aug. 2008.

[109] T.-T. Nguyen, T.-H. Chen, L. L. N. Thi, and C.-C. Tsai, "Polarization dependence of ^{133}Cs $6S_{1/2}$-$6P_{3/2}$-$11S_{1/2}$ electromagnetically induced transparency at room temperature," *Optics Express*, vol. 28, pp. 26313–26323, Aug. 2020.

[110] J. Wang, H. Liu, B. Yang, J. He, and J. Wang, "Determining the hyperfine structure constants of caesium 8S1/2 state aided by atomic coherence," vol. 25, p. 035501, Feb. 2014.

[111] B. Yang, Q. Liang, J. He, T. Zhang, and J. Wang, "Narrow-linewidth double-resonance optical pumping spectrum due to electromagnetically induced transparency in ladder-type inhomogeneously broadened media," *Physical Review A*, vol. 81, p. 043803, Apr. 2010.

[112] F. Helmchen and W. Denk, "Deep tissue two-photon microscopy," *Nature Methods*, vol. 2, pp. 932–940, Dec. 2005.

[113] H.-S. Chon, G. Park, S.-B. Lee, S. Yoon, J. Kim, J.-H. Lee, and K. An, "The dependence of transverse and longitudinal resolutions on incident Gaussian beam widths in the illumination part of optical scanning microscopy," May 2006. arXiv:physics/0411222.

[114] M. Mahamdeh, C. P. Campos, and E. Schäffer, "Under-filling trapping objectives optimizes the use of the available laser power in optical tweezers," *Optics Express*, vol. 19, pp. 11759–11768, June 2011.

[115] H. Urey, "Spot size, depth-of-focus, and diffraction ring intensity formulas for truncated Gaussian beams," *Applied Optics*, vol. 43, pp. 620–625, Jan. 2004.

[116] Thorlabs, "Spot Size Tutorial."

[117] M. Griot, "CVI Melles Griot Technical Guide Chapter 2 Gaussian Beam Optics."

[118] P. Samutpraphoot, *A quantum network node based on a nanophotonic interface for atoms in optical tweezers*. PhD Thesis, Harvard University, May 2021.

[119] S. G. Menon, K. Singh, J. Borregaard, and H. Bernien, "Nanophotonic quantum network node with neutral atoms and an integrated telecom interface," *New Journal of Physics*, vol. 22, p. 073033, July 2020.

[120] S. Girijavallabhan Menon, *Combining Nanophotonic Cavity-Arrays with Atomic Arrays: Scaling Quantum Computers and Networks*. PhD thesis, University of Chicago, June 2025.

[121] J. W. Jie Wang, G. Y. Guang Yang, J. H. Jun He, , and a. J. W. Junmin Wang, "Two-color cesium magneto-optical trap with 6S1/2-6P3/2-7S1/2 (852 nm+1470 nm) ladder-type system," *Chinese Optics Letters*, vol. 15, no. 5, pp. 050203–50207, 2017.

[122] S. Wu, T. Plisson, R. C. Brown, W. D. Phillips, and J. V. Porto, "Multiphoton Magnetooptical Trap," *Physical Review Letters*, vol. 103, p. 173003, Oct. 2009.

[123] A. Jenkins, J. W. Lis, A. Senoo, W. F. McGrew, and A. M. Kaufman, "Ytterbium Nuclear-Spin Qubits in an Optical Tweezer Array," *Physical Review X*, vol. 12, no. 2, 2022.

[124] B. M. Fields, *Integrating Trapped Neutral Atoms with Nanophotonic Resonators for a Novel Quantum Simulator*. PhD Thesis, Purdue University Graduate School, May 2021.

[125] T.-H. Chang, X. Zhou, H. Tamura, and C.-L. Hung, "Realization of efficient 3D tapered waveguide-to-fiber couplers on a nanophotonic circuit," *Optics Express*, vol. 30, pp. 31643–31652, Aug. 2022.

[126] B. Zeng, C. De-Eknamkul, D. Assumpcao, D. Renaud, Z. Wang, D. Riedel, J. Ha, C. Robens, D. Levonian, M. Lukin, R. Riedinger, M. Bhaskar, D. Sukachev, M. Loncar, and B. Machielse, "Cryogenic packaging of nanophotonic devices with a low coupling loss < 1 dB," Aug. 2023. arXiv:2306.09894 [physics].

[127] R. Marchetti, C. Lacava, L. Carroll, K. Gradkowski, and P. Minzioni, "Coupling strategies for silicon photonics integrated chips," *Photonics Research*, vol. 7, pp. 201–239, Feb. 2019.

[128] G. Son, S. Han, J. Park, K. Kwon, and K. Yu, "High-efficiency broadband light coupling between optical fibers and photonic integrated circuits," *Nanophotonics*, vol. 7, pp. 1845–1864, Dec. 2018.

[129] H. Sørensen, J.-B. Béguin, K. Kluge, I. Iakoupov, A. Sørensen, J. Müller, E. Polzik, and J. Appel, "Coherent Backscattering of Light Off One-Dimensional Atomic Strings," *Physical Review Letters*, vol. 117, p. 133604, Sept. 2016.

[130] P. Solano, P. Barberis-Blostein, F. K. Fatemi, L. A. Orozco, and S. L. Rolston, "Superradiance reveals infinite-range dipole interactions through a nanofiber," *Nature Communications*, vol. 8, p. 1857, Nov. 2017.

[131] N. V. Corzo, J. Raskop, A. Chandra, A. S. Sheremet, B. Gouraud, and J. Laurat, "Waveguide-coupled single collective excitation of atomic arrays," *Nature*, vol. 566, pp. 359–362, Feb. 2019.

[132] K. P. Nayak, J. Wang, and J. Keloth, "Real-Time Observation of Single Atoms Trapped and Interfaced to a Nanofiber Cavity," *Physical Review Letters*, vol. 123, p. 213602, Nov. 2019.

[133] C. Junge, D. O'Shea, J. Volz, and A. Rauschenbeutel, "Strong Coupling between Single Atoms and Nontransversal Photons," *Physical Review Letters*, vol. 110, p. 213604, May 2013.

[134] E. Will, L. Masters, A. Rauschenbeutel, M. Scheucher, and J. Volz, "Coupling a Single Trapped Atom to a Whispering-Gallery-Mode Microresonator," *Physical Review Letters*, vol. 126, p. 233602, June 2021.

[135] E. Deist, Y.-H. Lu, J. Ho, M. K. Pasha, J. Zeiher, Z. Yan, and D. M. Stamper-Kurn, "Mid-Circuit Cavity Measurement in a Neutral Atom Array," *Physical Review Letters*, vol. 129, no. 20, 2022.

[136] J. Goldwin, M. Trupke, J. Kenner, A. Ratnapala, and E. A. Hinds, "Fast cavity-enhanced atom detection with low noise and high fidelity," *Nature Communications*, vol. 2, p. 418, Aug. 2011.

[137] B. Hu, J. Sinclair, E. Bytyqi, M. Chong, A. Rudelis, J. Ramette, Z. Vendeiro, and V. Vuletić, "Site-Selective Cavity Readout and Classical Error Correction of a 5-Bit Atomic Register," *Physical Review Letters*, vol. 134, no. 12, 2025.

[138] J. Wang, D.-Y. Huang, X.-L. Zhou, Z.-M. Shen, S.-J. He, Q.-Y. Huang, Y.-J. Liu, C.-F. Li, and G.-C. Guo, "Ultrafast High-Fidelity State Readout of Single Neutral Atom," *Physical Review Letters*, vol. 134, no. 24, 2025.

[139] R. Gehr, J. Volz, G. Dubois, T. Steinmetz, Y. Colombe, B. L. Lev, R. Long, J. Estève, and J. Reichel, "Cavity-Based Single Atom Preparation and High-Fidelity Hyperfine State Readout," *Physical Review Letters*, vol. 104, no. 20, 2010.

[140] A. L. Shaw, A. Soper, D. Shadmany, A. Kumar, L. Palm, D.-Y. Koh, V. Kaxiras, L. Taneja, M. Jaffe, D. I. Schuster, and J. Simon, "A cavity array microscope for parallel single-atom interfacing," June 2025. arXiv:2506.10919 [quant-ph].

[141] J. P. McGilligan, K. R. Moore, A. Dellis, G. D. Martinez, E. de Clercq, P. F. Griffin, A. S. Arnold, E. Riis, R. Boudot, and J. Kitching, "Laser cooling in a chip-scale platform," *Applied Physics Letters*, vol. 117, p. 054001, Aug. 2020.

[142] B. Yang, Q. Liang, J. He, and J. Wang, "Background-free fluorescence detection of cold atoms in a two-color magneto-optical trap," *Optics Express*, vol. 20, pp. 11944–11952, May 2012.

[143] H. Ohadi, M. Himsworth, A. Xuereb, and T. Freegarde, "Magneto-optical trapping and background-free imaging for atoms near nanostructured surfaces," *Optics Express*, vol. 17, pp. 23003–23009, Dec. 2009.

[144] D. V. Sheludko, S. C. Bell, R. Anderson, C. S. Hofmann, E. J. D. Vredenbregt, and R. E. Scholten, "State-selective imaging of cold atoms," *Physical Review A*, vol. 77, p. 033401, Mar. 2008.

[145] J. P. McGilligan, K. R. Moore, R. Boudot, P. F. Griffin, A. S. Arnold, E. Riis, E. A. Donley, and J. Kitching, "Two-Photon Imaging of a Magneto-Optical Trap in a Micro-Fabricated Cell for Cold-Atom Sensors," in *2019 Joint Conference of the IEEE International Frequency Control Symposium and European Frequency and Time Forum*, pp. 1–2, Apr. 2019.

[146] N. M. Linke, D. T. C. Allcock, D. J. Szwer, C. J. Ballance, T. P. Harty, H. A. Janacek, D. N. Stacey, A. M. Steane, and D. M. Lucas, "Background-free detection of trapped ions," *Applied Physics B*, vol. 107, pp. 1175–1180, June 2012.

[147] H. J. Levine, *Quantum Information Processing and Quantum Simulation with Programmable Rydberg Atom Arrays*. PhD Thesis, Harvard University, July 2021.

[148] Y. Yang, F. Zhang, K. Tao, B. Sanchez, H. Wen, and Z. Teng, "An improved crest factor minimization algorithm to synthesize multisines with arbitrary spectrum," *Physiological Measurement*, vol. 36, p. 895, Apr. 2015.

[149] D. Hümmer, P. Schneeweiss, A. Rauschenbeutel, and O. Romero-Isart, "Heating in Nanophotonic Traps for Cold Atoms," *Physical Review X*, vol. 9, p. 041034, Nov. 2019.

[150] C.-L. Hung, A. González-Tudela, J. I. Cirac, and H. J. Kimble, "Quantum spin dynamics with pairwise-tunable, long-range interactions," *Proceedings of the National Academy of Sciences*, vol. 113, pp. E4946–E4955, Aug. 2016.

[151] S.-P. Yu, J. A. Muniz, C.-L. Hung, and H. J. Kimble, "Two-dimensional photonic crystals for engineering atom–light interactions," *Proceedings of the National Academy of Sciences*, vol. 116, pp. 12743–12751, June 2019.

[152] J.-B. Béguin, A. P. Burgers, X. Luan, Z. Qin, S. P. Yu, and H. J. Kimble, "Advanced apparatus for the integration of nanophotonics and cold atoms," *Optica*, vol. 7, p. 1, Jan. 2020.

[153] J.-B. Béguin, J. Laurat, X. Luan, A. P. Burgers, Z. Qin, and H. J. Kimble, "Reduced volume and reflection for bright optical tweezers with radial Laguerre–Gauss beams," *Proceedings of the National Academy of Sciences*, Oct. 2020.

[154] X. Zhou, H. Tamura, T.-H. Chang, and C.-L. Hung, "Coupling Single Atoms to a Nanophotonic Whispering-Gallery-Mode Resonator via Optical Guiding," *Physical Review Letters*, vol. 130, no. 10, 2023.

[155] A. González-Tudela, C.-L. Hung, D. E. Chang, J. I. Cirac, and H. J. Kimble, "Subwavelength vacuum lattices and atom–atom interactions in two-dimensional photonic crystals," *Nature Photonics*, vol. 9, pp. 320–325, May 2015.

[156] X. Zang, J. Yang, R. Faggiani, C. Gill, P. G. Petrov, J.-P. Hugonin, K. Vynck, S. Bernon, P. Bouyer, V. Boyer, and P. Lalanne, "Interaction between Atoms and Slow Light: A Study in Waveguide Design," *Physical Review Applied*, vol. 5, p. 024003, Feb. 2016.

[157] S. John and J. Wang, "Quantum electrodynamics near a photonic band gap: Photon bound states and dressed atoms," *Physical Review Letters*, vol. 64, pp. 2418–2421, May 1990.

[158] S. John and J. Wang, "Quantum optics of localized light in a photonic band gap," *Physical Review B*, vol. 43, pp. 12772–12789, June 1991.

[159] G. Kurizki, "Two-atom resonant radiative coupling in photonic band structures," *Physical Review A*, vol. 42, pp. 2915–2924, Sept. 1990.

[160] P. Lambropoulos, G. M. Nikolopoulos, T. R. Nielsen, and S. Bay, "Fundamental quantum optics in structured reservoirs," *Reports on Progress in Physics*, vol. 63, pp. 455–503, Mar. 2000.

[161] S. Bay, P. Lambropoulos, and K. Mølmer, "Atom-atom interaction in strongly modified reservoirs," *Physical Review A*, vol. 55, pp. 1485–1496, Feb. 1997.

[162] E. Munro, L. C. Kwek, and D. E. Chang, "Optical properties of an atomic ensemble coupled to a band edge of a photonic crystal waveguide," *New Journal of Physics*, vol. 19, p. 083018, Aug. 2017.

[163] T. Graß, C. Muschik, A. Celi, R. W. Chhajlany, and M. Lewenstein, "Synthetic magnetic fluxes and topological order in one-dimensional spin systems," *Physical Review A*, vol. 91, p. 063612, June 2015.

[164] F. Shimizu, "Specular Reflection of Very Slow Metastable Neon Atoms from a Solid Surface," *Physical Review Letters*, vol. 86, pp. 987–990, Feb. 2001.

[165] H. Friedrich, G. Jacoby, and C. G. Meister, "Quantum reflection by Casimir–van der Waals potential tails," *Physical Review A*, vol. 65, p. 032902, Feb. 2002.

[166] H. Bender, P. W. Courteille, C. Marzok, C. Zimmermann, and S. Slama, "Direct Measurement of Intermediate-Range Casimir-Polder Potentials," *Physical Review Letters*, vol. 104, p. 083201, Feb. 2010.

[167] N. P. Stern, D. J. Alton, and H. J. Kimble, "Simulations of atomic trajectories near a dielectric surface," *New Journal of Physics*, vol. 13, p. 085004, Aug. 2011.

[168] A. Asenjo-Garcia, J. D. Hood, D. E. Chang, and H. J. Kimble, "Atom-light interactions in quasi-one-dimensional nanostructures: A Green's-function perspective," *Physical Review A*, vol. 95, p. 033818, Mar. 2017.